Recent Advances in the Manufacturing of Polymeric Composites

Lead Guest Editor: Jinyang Xu
Guest Editors: J. Paulo Davim and Mohamed El Mansori

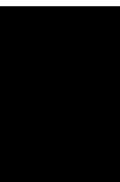# Recent Advances in the Manufacturing of Polymeric Composites

Recent Advances in the Manufacturing of Polymeric Composites

Lead Guest Editor: Jinyang Xu
Guest Editors: J. Paulo Davim and Mohamed El Mansori

Francisco Javier Fernández Fernández (iD), Spain

Isabel J. Ferrer (iD), Spain

Dora Foti (iD), Italy

Massimo Fresta, Italy

Dhanesh G. Mohan, China

Samia Gad, Egypt

Pasquale Gallo (iD), Finland

Sharanabasava Ganachari, India

Santiago Garcia-Granda (iD), Spain

Carlos Garcia-Mateo, Spain

Achraf Ghorbal (iD), Tunisia

Georgios I. Giannopoulos (iD), Greece

Ivan Giorgio (iD), Italy

Antonio Gloria (iD), Italy

Andrea Grilli (iD), San Marino

Vincenzo Guarino (iD), Italy

Daniel Guay, Canada

Gianluca Gubbiotti (iD), Italy

Jenö Gubicza (iD), Hungary

Xuchun Gui, China

Benoit Guiffard (iD), France

Zhixing Guo, China

Ivan Gutierrez-Urrutia (iD), Japan

Weiwei Han (iD), Republic of Korea

Simo-Pekka Hannula, Finland

A. M. Hassan (iD), Egypt

Akbar Heidarzadeh, Iran

Yi Huang (iD), United Kingdom

Michele Iafisco (iD), Italy

Saliha Ilican (iD), Turkey

Md Mainul Islam (iD), Australia

Ilia Ivanov (iD), USA

Hafsa Jamshaid, Pakistan

Hom Kandel (iD), USA

Kenji Kaneko, Japan

Rajesh Kannan A, Democratic People's Republic of Korea

Fuat Kara (iD), Turkey

Mehran Khan (iD), Hong Kong

Akihiko Kimura, Japan

Fantao Kong, China

Ling B. Kong (iD), Singapore

Lingxue Kong (iD), Australia

Pramod Koshy, Australia

Hongchao Kou, China

Alexander Kromka, Czech Republic

Abhinay Kumar, India

Avvaru Praveen Kumar, Ethiopia

Paweł Kłosowski (iD), Poland

Wing-Fu Lai (iD), Hong Kong

Andrea Lamberti (iD), Italy

Luciano Lamberti, Italy

Fulvio Lavecchia (iD), Italy

Marino Lavorgna (iD), Italy

Laurent Lebrun (iD), France

Joon-Hyung Lee (iD), Republic of Korea

Cristina Leonelli, Italy

Chenggao Li (iD), China

Rongrong Li, China

Ying Li (iD), USA

Yuanshi Li, Canada

Yuning Li, Canada

Guang-xing Liang (iD), China

Barbara Liguori (iD), Italy

Jun Liu (iD), China

Yunqi Liu, China

Zhiping Luo (iD), USA

Fernando Lusquiños (iD), Spain

Himadri Majumder, India

Georgios Maliaris (iD), Greece

Dimitrios E. Manolakos, Greece

Necmettin Maraşlı (iD), Turkey

Anish Mariadhas, India

Alessandro Martucci (iD), Italy

Roshan Mayadunne (iD), Australia

Nur Izzi Md Yusoff (iD), Malaysia

Mamoun Medraj (iD), Canada

Shazim A. Memon (iD), Kazakhstan

Pratima Meshram, India

Mohsen Mhadhbi (iD), Tunisia

Philippe Miele, France

Andrey E. Miroshnichenko, Australia

Ajay Kumar Mishra (iD), South Africa

Hossein Moayedi (iD), Vietnam

Sakar Mohan (iD), India

Tahir Muhmood, China

Faisal Mukhtar, Pakistan

Dr. Tauseef Munawar, Pakistan

Roger Narayan (iD), USA

Saleem Nasir, Pakistan
Rufino M. Navarro, Spain
Miguel Navarro-Cia, United Kingdom
Yasir Nawab, Pakistan
Behzad Nematollahi, Australia
Peter Niemz, Switzerland
Hiroshi Noguchi, Japan
Dariusz Oleszak, Poland
Laurent Orgéas, France
Togay Ozbakkaloglu, United Kingdom
Marián Palcut, Slovakia
Davide Palumbo, Italy
Gianfranco Palumbo, Italy
Zbyšek Pavlík, Czech Republic
Alessandro Pegoretti, Italy
Gianluca Percoco, Italy
Andrea Petrella, Italy
Claudio Pettinari, Italy
Giorgio Pia, Italy
Daniela Pilone, Italy
Teresa M. Piqué, Argentina
Candido Fabrizio Pirri, Italy
Marinos Pitsikalis, Greece
Alain Portavoce, France
Simon C. Potter, Canada
Ulrich Prahl, Germany
Ramadhansyah Putra Jaya, Malaysia
Veena Ragupathi, India
Kawaljit singh Randhawa, India
Baskaran Rangasamy, Zambia
Ghulam Rasool, China
Manijeh Razeghi, USA
Paulo Reis, Portugal
Hilda E. Reynel-Avila, Mexico
Yuri Ribakov, Israel
Aniello Riccio, Italy
Anna Richelli, Italy
Antonio Riveiro, Spain
Marco Rossi, Italy
Fernando Rubio-Marcos, Spain
Francesco Ruffino, Italy
Pietro Russo, Italy
Giuseppe Ruta, Italy
Sachin Salunkhe, India
F.H. Samuel, Canada

Carlo Santulli, Italy
Fabrizio Sarasini, Italy
Senthil Kumaran Selvaraj, India
Raffaele Sepe, Italy
Aabid H Shalla, India
Poorva Sharma, China
Mercedes Solla, Spain
Tushar Sonar, Russia
Donato Sorgente, Italy
Charles C. Sorrell, Australia
Andres Sotelo, Spain
Damien Soulat, France
Adolfo Speghini, Italy
Antonino Squillace, Italy
Koichi Sugimoto, Japan
Jirapornchai Suksaeree, Thailand
Baozhong Sun, China
Sam-Shajing Sun, USA
Xiaolong Sun, China
Shengwen Tang, China
Yongding Tian, China
Hao Tong, China
Miguel Angel Torres, Spain
Laszlo Toth, France
Achim Trampert, Germany
Tomasz Trzepieciński, Poland
Kavimani V, India
Matjaz Valant, Slovenia
Luca Valentini, Italy
Mostafa Vamegh, Iran
Lijing Wang, Australia
Zhongchang Wang, Portugal
Jörg M. K. Wiezorek, USA
Guosong Wu, China
Junhui Xiao, China
Guoqiang Xie, China
Jinyang Xu, China
Anil Singh Yadav, India
Yee-wen Yen, Taiwan
Hao Yi, China
Wenbin Yi, China
Tetsu Yonezawa, Japan
Hiroshi Yoshihara, Japan
Bin Yu, China
Dongdong Yuan, China

Contents

Editorial

Recent Advances in the Manufacturing of Polymeric Composites

Jinyang Xu [iD],[1] **J. Paulo Davim,**[2] **and Mohamed El Mansori**[3]

[1]*School of Mechanical Engineering, Shanghai Jiao Tong University, Shanghai 200240, China*
[2]*Department of Mechanical Engineering, University of Aveiro, Campus Santiago, Aveiro 3810-193, Portugal*
[3]*MSMP-EA 7350, Arts et Métiers ParisTech, Châlons-en-Champagne 51006, France*

Correspondence should be addressed to Jinyang Xu; xujinyang@sjtu.edu.cn

The current special issue focuses on reporting the latest advances achieved in the field of polymeric composite manufacturing. The addressed polymeric composites represent an advanced functional material being extensively utilized in various industries. This type of material shows higher specific mechanical properties and better structural functionalities compared with conventional alloys and steels. Polymeric composites are often fabricated by reinforcing fibres and polymer matrices, showing anisotropic behaviour and heterogeneous structure. Mechanical manufacturing, such as trimming, turning, and drilling, are essential operations to shape the composite specimens into desired quality and target dimensions. However, polymeric composites show very poor machinability owing to their inherent anisotropic behaviour. The manufacture of polymeric composites involves issues such as the design of the processing operations, the optimization of the machining parameters, the minimization of the manufacturing damage, the quantification of accuracy and quality, the monitoring of manufacturing outputs, and the control of tool wear.

This special issue aims to discuss the recent research challenges and achievements in manufacturing polymeric composites, covering both experimental and numerical investigations. Rigorous peer-review processes were undertaken to ensure the academic quality of the published papers. It is hoped that the contributions collected in this special issue can provide useful information as a basis for a better understanding of the manufacturing science and technology of polymeric composites and may further aid the development of advanced manufacturing techniques for other engineering composites.

Conflicts of Interest

The guest editors declare that there are no conflicts of interest involved in this special issue.

Acknowledgments

Research Article

Investigation of Drilling Process Parameters of Palmyra Based Composite

A. Mohan Kumar ⬚,[1] R. Rajasekar ⬚,[1] P. Manoj Kumar ⬚,[2] R. Parameshwaran ⬚,[1] Alagar Karthick ⬚,[3] V. Mohanavel ⬚,[4] T. Sakthi,[5] and M. Muhibbullah ⬚[6]

[1]*School of Building and Mechanical Sciences, Kongu Engineering College, Perundurai 638060, Tamilnadu, India*
[2]*Department of Mechanical Engineering, KPR Institute of Engineering and Technology, Coimbatore 641407, Tamilnadu, India*
[3]*Department of Electrical and Electronics Engineering, KPR Institute of Engineering and Technology, 641407 Coimbatore, Tamilnadu, India*
[4]*Centre for Materials Engineering and Regenerative Medicine, Bharath Institute of Higher Education and Research, 600073 Chennai, Tamilnadu, India*
[5]*Department of Mechanical Engineering, National Engineering College, K.R. Nagar, Kovilpatti 628 503, Tamilnadu, India*
[6]*Department of Electrical and Electronic Engineering, Bangladesh University, Dhaka 1207, Bangladesh*

Correspondence should be addressed to A. Mohan Kumar; amohanmech2006@gmail.com and M. Muhibbullah; m.muhibbullah@bu.edu.bd

The drilling process is the most essential in the final assembly of the mechanical parts. Natural fiber based composites replace traditional materials due to their advantages, such as strength to weight ratio, availability, and environmental hazards. In this work, an attempt has been made to find the minimum thrust force produced by the drill tool at specified drilling process parameters. The drilling process parameters used for the investigation are rotational speed, tool feed, and resins. The spindle speed and feed rate are selected with three levels. Three resin materials were used, namely, epoxy, polyester, and vinyl ester. Taguchi's L_{27} orthogonal array was implemented. The result shows that the candlestick drill bit generated lesser thrust force at the specified drilling process parameters, followed by the twist and step cone drill bits.

1. Introduction

Environmental protection is the main focus towards the use of cellulose fiber as reinforcement in the polymer matrix. Natural fibers having many advantages compared to synthetic fibers are lightweight, available in plenty, biodegradable, and no hazards to the environment. Hence, they are used as load transfer material in composite material. However, they have few drawbacks compared to synthetic materials, such as poor resistance to water, lesser modulus, and lower strength. Few authors reported the different studies in the natural fiber based composites, namely, hemp, abaca, sisal, banana, oil palm, and wood pulp [1–3]. The strength and stiffness characteristics of the natural fiber based composite can be improved by increasing interfacial bonding of the fibers and matrixes [4].

The machining of the fiber based composite is complicated due to the property difference and the fiber orientation nature of the natural fibers reinforcement [5]. Hence, it is required special attention to analyze fiber based composite compared to homogeneous machining. During drilling of the fiber strengthened composite, the effect of the mechanical and thermal properties is more. Hence, the selection of the process factors of the drilling process and the experimental conditions is more essential to produce quality machining. During fiber based composite machining process, the manufacturing defects produced are cracks, voids, fiber pullouts, delamination, and thermal defects. The following factors are considered to determine the machinability of the fiber-reinforced composite: tool materials, tool geometry, cutting condition, and type of

machining process [6–8]. The other factors, namely, surface roughness, roundness, and residual stress, are considered less critical.

Drilling is an essential machining process in the final assembly process of the manufacturing industry [9–13]. Different methods are used to make a hole on the fiber based composite. However, the most common traditional method has been employed. According to the forces generated during drilling, drilling is more complicated than another machining process. Few other factors affect the hole quality, namely, delamination fiber pullouts and surface roughness. To overcome the defects generated during the drilling process, it is required to develop proper experimental procedures, machining conditions, and cutting conditions [5, 14, 15].

The composites are inclined towards delamination and fiber pullouts due to their unidirectional properties. The hole quality is checked by visual inspection that is a standard assessment method. The delamination defects may be present, namely, peel-up and push-down delamination in the drilled hole. The measurement of the delamination in the natural fiber based composite is either direct or indirect. Indirect measurement measures delamination factors such as chip produced, damage width, surface unevenness, and delamination factor. The indirect measurement includes assessment of axial force, torque, and power generation during the drilling process.

In most of the direct assessment methods of delamination, the essential parameter considered is the delamination factor. The delamination is majorly classified into two types, namely, push-down and peel-up delamination. The following parameters are considered appropriate to avoid defects during the drilling process: drill rate, cutting speed, tool shape, and experimental conditions [16]. Feito et al. [17] found the lesser axial force and delamination factor during drilling at a low drill rate using stepped drill geometry. In addition, the backplate can be used to diminish delamination factor and axial force and obtain quality holes. They stated that the best contract is obtained between the experimental results and the mathematical model. The investigation was carried out with flax-based composite and found that the defacing factor reduces with drill rate.

Additionally, different factor accounts in the numerical model have been validated with experimental results [18]. Vinayagamoorthy et al. analyzed the hole-making characteristics of the vetiver-based composite. The drill's drilling rate and point angle mainly influence the push-out defacing, but the effect of the spindle speed is very minimal. They also found that the spindle speed, drill rate, and point angle majorly influence the peel-up defacing [19]. Rezghi Maleki et al. found that the feed rate has influenced the axial force generation during drilling jute-based fibers for all drill tools. They concluded that the high-speed steel drill and CoroDrill 856 contribute more to the generation of axial force and surface unevenness during drilling compared to CoroDrill 854, feed rate 0.15 mm/rev, and rotational speed 1250 rpm that are very much suitable for drilling of jute-based composite with minimum drilling defects [20]. Rezghi Maleki et al. repeated the same investigation to the flax-

based fibers and found that the high-speed drill influences the thrust force generated more than the CoroDrill 856 and CoroDrill 854 drill bits. They also reported that the hole quality and delamination factor influence the different geometrical drill bits more than the spindle speed and drill rate [21]. Patel et al. investigated the drilling characteristics of the hybrid composite, namely, basalt/glass, the tool geometry, and the lamination sequences effects of peel-up and push-down delamination. The parabolic geometry of the drill bit with high feed shows lesser delamination at exit. They concluded that the low spindle speed, low feed, and parabolic geometry drill bit are very much suitable for drilling hybrid composites to produce high quality holes [22]. Pradeep and Rajasekaran [23] analyzed the drilling behavior in chopped jute-based fiber, and three different drill tool materials are used, namely, high-speed steel, cobalt steel, and tungsten carbide. The axial force required to make the hole is lesser for the tungsten drill bit than other drill bits. Bajpai and Singh [24] found the drilling characteristics of the sisal fiber based composite, and two different geometrical drill bits have been used, namely, twist and trepanning tools. The thrust force generated by the trepanning tool is much lower compared to the twist tool. They concluded that the hollow drill bit might be suitable to drill natural fiber-reinforced composites. The drilling process parameters, namely, spindle speed, drill rate, and the drill geometries, are influenced much more by the defacing factor and drilling forces (axial force and torque) during drilling of sisal/optiva natural fiber based composites. Among the process parameters, the drill bit geometry contributes more to the defacing factor [25]. Roy Choudhury et al. [26] examined drilling-induced delamination, forces, and induced temperature produced during the drilling process experimentally. The five different geometric drill bits have been used for the investigation. Turki et al. [27] inspected the influence of fiber alignment on the delamination damage and thrust force. The friction-induced between the tool and the composite surfaces is examined by the temperature developed during the carbon fiber-reinforced epoxy composite specimen. The assessment between the thrust force and the defacing factor of two dissimilar geometrical drill bits on the flax-based composites has been carried out. They also found that the feed rate affects more the induced damage during drilling in the composite specimen [28].

The delamination defect, namely, peel-up occurred at the tool entrance of the composite specimen. When the tool starts to pierce the surface of the specimen, it generates peel-up force in the axial direction, and it separates the laminates. The delamination degree will depend on the rotational speed and point angle. The push-down delamination happens at the exit of the drilled hole. This is because the resistive force offered by the exit laminae is lesser than the axial force of the tool. Hence, it generates exit delamination [29]. Belaadi et al. [30] investigated the drilling process parameters with four different geometrical drill bits, and response surface methodology and artificial neural networks are used to authenticate the experimental values. The two techniques obtained from the artificial neural network are closer to the experimental value than the response surface methodology.

Rajaraman et al. [31] examined the process parameters of drilling on the kenaf and banana-based composite. The high-speed steel of three different diameters and the L9 factorial method has been used for the experimental study. They concluded that the spindle speed of 3000 rpm and 150 mm/min has been suitable for defect-free holes. Panneerselvam et al. [32] investigated the drilling on the sisal/glass hybrid composite and found that the drilling rate influences the exit defacing more. They used a profile projector, and image processing software was used to examine the defects in the holes. Abilash and Sivapragash [33] evaluated the effect of the induced force during drilling of bamboo-based composites and developed the regression modelling to reduce exit delamination. Ramesh et al. [34] investigated the drilling defects in hybrid composites, which consist of the sisal/glass, also found that the axial force is enhanced with drill rate, and obtained the maximum value for high-speed steel tool.

The availability of Palmyra fiber is plenty in south zone of India especially in Tamilnadu. It made interesting investigation on optimization of drilling parameters during drilling of Palmyra based composite. Only few papers are available on characteristic study of Palmyra based composite. However, there are no research papers available for drilling parameters optimization of Palmyra based composites. Hence, in this investigation, an attempt has been made to find the most appropriate drilling process parameters to reduce drilling defects. One appropriate drill bit has been suggested with optimum drilling process parameters among the two different geometrical drill bits used for this investigation. As per Taguchi's design of the experiment L_{27} model has been used for investigation. Table 1 shows the methodology of investigation on drilling process parameters of Palmyra based composite.

2. Materials and Methods

The three matrices have been used for the investigation, namely, epoxy, polyester, and vinyl ester. The density and viscosity of epoxy at 25°C are 1.16 gm/cm^3 and 900 cps, respectively. The hardener used is 3 diacid anhydride. The density and viscosity of vinyl ester at 25°C are 1.052 gm/cm^3 and 325 cps, respectively. For polyester, the density and viscosity at 25°C are 1.12 gm/cm^3 and 500 cps, respectively. These are purchased from the Aypols private limited Coimbatore. Methyl ethyl ketone peroxide and cobalt activator are used as curing system for vinyl ester and polyester resin, respectively. The Palmyra sprout fiber extracted from the Palmyra sprout fruit (*Borassus flabellifer*) is shown in Figure 1. Sipcon vertical profile projector has been used to view outer periphery of the drilled hole. The resolution of the profile projector is up to 0.5 micrometer.

2.1. Experimental Setup. The investigation has been carried out in Computer Numerical Control (CNC) vertical machining center. The maximum spindle speed, power, and machine axis are 40,000 rpm, 5 kW, and 3. The drill tool dynamometer is of 50 Hz frequency, with the axial measuring range 0–50000 N fixed in the CNC platform as shown

in Figure 2. The drilling tool is 6 mm carbide, and different geometries were used, namely, standard twist, candlestick, and step cone drill bits, as shown in Figure 3. Three levels of rotational speed and drill rate have feed considered for investigation. Three levels of rotational speed are 1000, 1500, and 2000 rpm. Three levels of feed are 0.1, 0.15, and 0.2 mm/rev.

2.2. Composite Fabrication. The Palmyra sprout fiber is cleaned and chopped with 5 to 10 cm length. The range of diameter is 0.05 to 2 cm. The fibers are dried under vacuum for 3 hours at the temperature of 60°C [35]. The palmyra sprout fiber-reinforced polyester, vinyl ester, and epoxy are made up of hand layup process and compression moulding techniques. The fibers are randomly oriented, and steel rollers have been used to form an even surface of the specimen. The uniform thickness of the specimen has been obtained by the hydraulic press for 4 hours. The curing reagent of 1 Vol.% has been used for fast curing. The composite specimen has been allowed to cool for 24 hours at atmospheric temperature. The required dimension of 30 cm ∗ 3 cm ∗ 0.3 cm was obtained as shown in Figure 4.

2.3. Taguchi Method. The Taguchi method of optimization has been selected for this study due to the three process parameters, three levels, and one response parameters, and L_{27} full factorial method has been implemented. The output influencing parameters are listed in the orthogonal array Table 1. The L_{27} orthogonal array test can be conducted to minimize a large number of experiments. The maximum signal to noise ratio value is considered the best value to minimize the thrust force value. A loss function has been characterized to determine the difference between the experimental value and the standard value. The process behavior is characteristic of three types: the smaller the better, the nominal the better, and the higher the better .

$$\text{Lower} - \text{the} - \text{better} = -10 \log\left(\frac{1}{n}\sum_{i=1}^{n} y_t^2\right), \quad (1)$$

where n = number of replications and y_t = tensile strength for the ith trial.

3. Results and Discussion

Many researches prove that the defects produced during drilling of the fiber based composites depend on the thrust force produced during drilling [8, 15, 34]. The axial force was determined using different geometrical drill bits to drill the palmyra fiber-reinforced epoxy, polyester, and vinyl ester composites. The three drill bits used for the analysis are the candlestick, twist, and step one. The axial force generated during drilling of Palmyra fiber based composite is listed in the Table 1. The L_{27} orthogonal array is used with three drilling process factors: resin, rotational speed, and drill rate. Three levels of spindle speed are 1000, 1500, and 2000 rpm. Three levels of feed are 0.1, 0.15, and 0.2 mm/rev. The axial force generated by the three drill tools shown in Table 2

TABLE 1: Methodology of investigation on drilling process parameters of Palmyra based composite.

Materials	Fibers	Palmyra sprout fruit
	Resins	Epoxy
		Polyester
		Vinyl ester
Drilling process parameters	Speed (rpm)	1000, 1500, 2000
	Feed (mm/rev)	0.10, 0.15, 0.20
	Drill bit geometry	Candlestick, standard twist, and Stepcone drill
	Response parameter	Thrust force (N)
Experimental setup	Fabrication method	Hand layup process
	Machine	CNC vertical machining center
Optimization of process parameters	Taguchi's method	L_{27} orthogonal array

(a)   (b)

FIGURE 1: (a) Palmyra sprout fruit. (b) Palmyra sprout fiber.

varies from 7.39 N to 12.83 N. The axial force generated by the candlestick drill bit is lesser than that of other drill bits. At 1000 rpm and 0.2 mm/rev, the axial force generated by the candlestick is minimum. The smaller it is, the better option has been considered for the S/N ratio to find the deviation from the desired value as shown in Figure 5. Since lesser thrust force is required, the smaller, the better S/N ratio selected for the study.

At 1000 rpm rotational speed, and 0.2 mm/rev axial feed, the drilled hole of the Palmyra reinforced epoxy specimen by candlestick drill bit has been viewed using profile projector as shown in Figure 6. The specimen has been cut laterally and viewed using profile projector; it is clear that the defects on the specimen at specified speed, feed, and drill bit are lower compared with the drilled hole at different speeds and feeds.

Figure 5 shows the Signal to Noise (S/N) ratio during drilling of Palmyra based composite. Figure 5(a) shows the S/N ratio of thrust force generated by the candlestick

drill bit. The lower S/N ratio value is shown at 1000 rpm and 0.2 mm/rev. Similarly, at 1000 rpm and 0.2 mm/rev, the S/N ratio of thrust force produced by the twist drill has a minimum, as shown in Figure 5(b). At 2000 rpm and 0.2 mm/rev, the S/N ratio of thrust force produced by the step cone drill bit has a minimum, as shown in Figure 5(c).

The signal to noise ratio of spindle speed is increased to 18.5% and 92.59% for 1500 rpm and 2000 rpm, respectively, compared to 1000 rpm for the candlestick drill bit during the drilling process Figure 5(a). It implies that the spindle speed increases with the increase in the thrust force value. For candlestick drills, the thrust force value is significantly influenced by the spindle speed. Similarly, the signal to noise ratio during drilling of the composite by standard twist drill is increased to 59.09% and 50% for the spindle speed of 1500 rpm and 2000 rpm, respectively, compared to 1000 rpm as shown in the Figure 5(b). In contrast, the signal to noise ratio decreases to 32.2% and 12.9% for the step cone drill bit
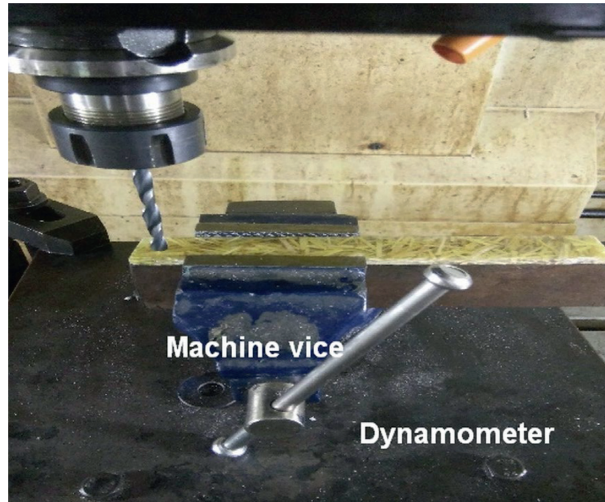
FIGURE 2: Drilling experimental setup.

(a)

(b)

(c)
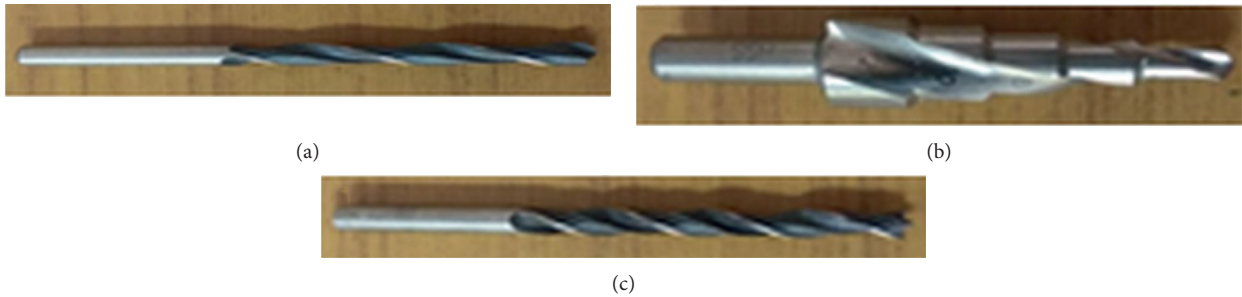
FIGURE 3: (a) Standard twist drill, (b) step cone drill, and (c) candlestick drill tools.

(a)

(b)

(c)
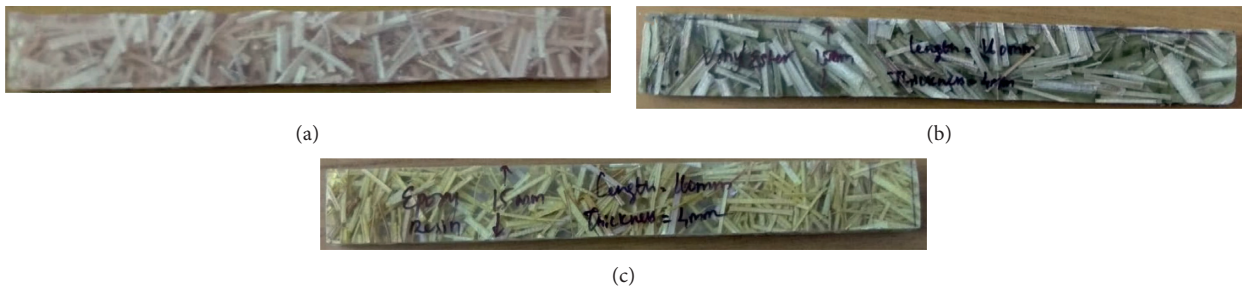
FIGURE 4: Palmyra sprout fiber-reinforced (a) polyester, (b) vinyl ester, and (c) epoxy composites specimen.

for spindle speed 2000 rpm and 1500 rpm, respectively, compared to the 1000 rpm as shown in Figure 5(c). The signal to noise ratio increases with the increase in the spindle speed for the candlestick and twist drill bit. In contrast, the signal to noise ratio decreases with spindle speed for the step cone drill bit. The statistical significance of the spindle on the thrust force generated by the candlestick drill bit is very high compared to the other drill bits. The thrust force values greatly reduced at 1000 rpm spindle speed due to the forces generated, as drill bit A has been transferred to the outer periphery compared to the other drill bits.

For the candlestick drill bit, the tool feed's signal to noise ratio increases to 0.15 mm/rev and then decreases, as shown in Figure 5(a). The percentage of the signal to noise ratio of tool feed increases to 32.35% and then decreases to 67.85%, corresponding to 0.15 mm/rev and 0.20 mm/rev, respectively. The same trend has been followed for the other drill bit also; for a standard twist drill, the signal to noise ratio of tool feed increases to 10.34% and then decreases to 18.5%, corresponding to the 0.15 mm/rev and 0.2 mm/rev, respectively. Likewise, the signal to noise ratio of tool feed increases to 1.38% and then decreases to 12.12%, corresponding to the 0.15 mm/rev and 0.2 mm/rev, respectively. The statistical importance of the tool feed on the thrust force generated by the candlestick drill bit is very high compared to other drill bits. The thrust force values greatly reduced at

TABLE 2: Thrust force generated by the candlestick, standard twist, and step cone drill bits during the drilling process.

S. no	Resin	Speed (rpm)	Feed (mm/rev)	Thrust force by candlestick (N)	Thrust force by a twist drill	Thrust force by step cone drill
1	Epoxy	1000	0.10	08.153	10.371	11.232
2	Epoxy	1000	0.15	09.292	10.674	11.331
3	Epoxy	1000	0.20	07.392	10.998	10.459
4	Epoxy	1500	0.10	10.169	10.370	12.981
5	Epoxy	1500	0.15	09.125	10.458	10.600
6	Epoxy	1500	0.20	10.023	10.566	10.968
7	Epoxy	2000	0.10	09.674	10.234	12.259
8	Epoxy	2000	0.15	10.359	10.356	12.657
9	Epoxy	2000	0.20	09.129	10.554	11.227
10	Polyester	1000	0.1	09.627	10.369	11.599
11	Polyester	1000	0.15	10.522	10.273	11.451
12	Polyester	1000	0.20	08.439	10.123	11.348
13	Polyester	1500	0.10	10.438	10.262	11.117
14	Polyester	1500	0.15	10.566	10.178	10.573
15	Polyester	1500	0.20	10.635	10.019	11.896
16	Polyester	2000	0.10	09.534	10.198	10.693
17	Polyester	2000	0.15	08.356	09.956	13.893
18	Polyester	2000	0.20	09.259	09.897	11.354
19	Vinyl ester	1000	0.10	08.933	10.595	11.400
20	Vinyl ester	1000	0.15	09.875	10.097	11.366
21	Vinyl ester	1000	0.20	08.996	09.899	10.289
22	Vinyl ester	1500	0.10	10.544	10.480	11.090
23	Vinyl ester	1500	0.15	09.153	10.569	11.199
24	Vinyl ester	1500	0.20	09.756	10.668	13.288
25	Vinyl ester	2000	0.10	09.432	10.393	12.639
26	Vinyl ester	2000	0.15	09.356	10.456	12.156
27	Vinyl ester	2000	0.20	08.289	09.754	10.887
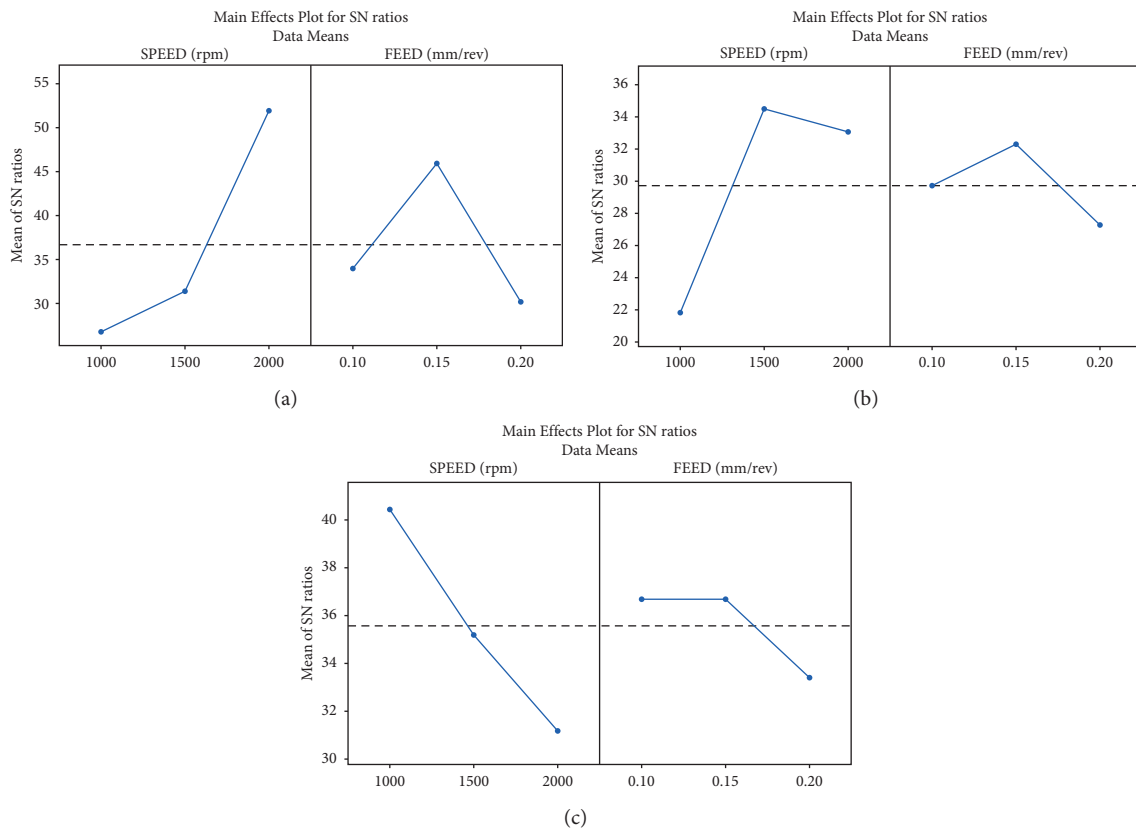
FIGURE 5: Signal-noise ratio of (a) candlestick, (b) twist, and (c) step cone drill bits during the drilling process.

FIGURE 6: Periphery of the drilled hole is viewed using profile projector.

0.2 mm/rev feed rate, because the forces generated during drill bit A have been transferred to the outer periphery compared to the other drill bits. The suitable spindle speed and feed rate are 1000 rpm and 0.2 mm/rev, respectively, to drill Palmyra reinforced epoxy composites.

The defects generated during drilling of Palmyra reinforced epoxy resin depend on the thrust force generated during drilling [8, 15, 34]. In previous studies, it is evident that the peel-up and push-down defects at the entry and exit, respectively, are formed during drilling. Hence, this work aims to reduce thrust force and achieve defect-free hole. Among the three different geometrical drill bits, the candlestick drill bit distributes the axial force into the outer circumferential of the hole. This may be the reason for the lower thrust force. The twist and step cone drill bit transmit thrust force in the axial direction; hence, the thrust force generated at the end of the composite specimen is higher due to the tool's axial force exceeding the adhesive force of uncut thickness the composite specimen [36, 37].

4. Conclusion

The drilling analysis has been carried out on the Palmyra based composites. Three process parameters have been selected for the investigation: resin, rotational speed, and drill rate. The three levels of rotational speed and drill rate have been chosen for the study. The result shows that the axial force generated by the candlestick drill bit during the drilling process has a minimum. It is followed by the twist and step cone drill bits. At lower rotational speed and higher drill rate, the thrust force generated by the candlestick and the twist drill has a minimum. Likewise, at the maximum rotational speed and higher drill rate, the axial force produced by the step cone drill bit is minimum. The minimum axial force produced by the candlestick drill tool is distributed to the tool's outer periphery. The thrust force of the drill tool exceeds the adhesive force of uncut thickness of the composite specimen, and it may be the cause for the higher axial force of twist and step cone drill bits.

Data Availability

The data used to support the findings of this study are included in the article.

Conflicts of Interest

The authors declare that there are no conflicts of interest regarding the publication of this article.

Acknowledgments

References

[1] A. M. Kumar, R. Parameshwaran, P. S. Kumar et al., "Effects of abaca fiber reinforcement on the dynamic mechanical behavior of vinyl ester composites," *Materials Testing*, vol. 59, no. 6, pp. 555–562, 2017.

[2] A. Mohan Kumar, M. Gowthaman, M. Harikrishnan, and A. Kesava nanthanan, "Investigation of mechanical behavior of palmyra palm petiole fiber reinforced epoxy composites," *Materials Today: Proceedings*, vol. 45, pp. 1417–1422, 2021.

[3] M. S. Sreekala and S. Thomas, "Utilization of short oil palm empty fruit bunch fiber (OPEFB) as a reinforcement in phenol-formaldehyde resins: studies on mechanical properties," *Journal of Polymer Engineering*, vol. 16, no. 4, pp. 265–294, 1996.

[4] K. Yoganandam, V. Shanmugam, A. Vasudevan et al., "Investigation of dynamic, mechanical, and thermal properties of Calotropis procera particle-reinforced PLA biocomposites," *Advances in Materials Science and Engineering*, vol. 2021, Article ID 2491489, 2021.

[5] V. Kavimani, B. Stalin, P. M. Gopal, M. Ravichandran, and M. Bharani, "Application of r-GO-MMT hybrid nanofillers for improving strength and flame retardancy of epoxy/glass fibre composites," *Advances in Polymer Technology*, vol. 2021, Article ID 6627743, 2021.

[6] P. P. Gohil, V. Chaudhary, and K. Patel, "Challenges in machining of natural fibre composites," in *Manufacturing of Natural Fibre Reinforced Polymer Composites*, pp. 139–153, Springer, Berlin, Germany, 2015.

[7] J. P. Davim, F. Mata, V. N. Gaitonde, and S. R. Karnik, "Machinability evaluation in unreinforced and reinforced PEEK composites using response surface models," *Journal of*

Thermoplastic Composite Materials, vol. 23, no. 1, pp. 5–18, 2010.

[8] R. Parameshwaran, A. Mohan kumar, R. Rajasekar, V. C. Harissh Ragavendra, and N. Praveenraj, "Effect of thrust force, torque, and induced temperature on Kevlar reinforced composites during drilling process," *Materials Today: Proceedings*, vol. 45, pp. 522–528, 2021.

[9] V. Manikandan, J. T. Winowlin Jappes, S. M. Suresh Kumar, and P. Amuthakkannan, "Investigation of the effect of surface modifications on the mechanical properties of basalt fibre reinforced polymer composites," *Composites Part B: Engineering*, vol. 43, no. 2, pp. 812–818, 2012.

[10] C. Duraipandi, A. Khan M, J. J. T. Winowlin, N. M. Ghazaly, and P. M. Mashinini, "Solid particle erosion studies of thermally deposited alumina-titania coatings on an aluminum alloy," *International Journal of Minerals, Metallurgy and Materials*, vol. 28, no. 7, pp. 1186–1193, 2021.

[11] K. Ganesan, C. Kailasanathan, N. Rajini et al., "Assessment on hybrid jute/coir fibers reinforced polyester composite with hybrid fillers under different environmental conditions," *Construction and Building Materials*, vol. 301, Article ID 124117, 2021.

[12] K. Sudalaiyandi, K. Alagar, M. P. Vj, and P. Madhu, "Performance and emission characteristics of diesel engine fueled with ternary blends of linseed and rubber seed oil biodiesel," *Fuel*, vol. 285, Article ID 119255, 2021.

[13] M. Vetrivel Sezhian, K. Giridharan, D. Peter Pushpanathan, G. Chakravarthi, B. Stalin, and M. Bharani, "Microstructural and mechanical behaviors of friction stir welded dissimilar AA6082-AA7075 joints," *Advances in Materials Science and Engineering*, vol. 2021, Article ID 4113895, 2021.

[14] S. D. Kumar, M. Ravichandran, A. Jeevika, B. Stalin, C. Kailasanathan, and A. Karthick, "Effect of ZrB2 on microstructural, mechanical and corrosion behaviour of aluminium (AA7178) alloy matrix composite prepared by the stir casting route," *Ceramics International*, vol. 47, no. 9, pp. 12951–12962, 2021.

[15] S. Senthilkumar, A. Karthick, R. Madavan et al., "Optimization of transformer oil blended with natural ester oils using Taguchi-based grey relational analysis," *Fuel*, vol. 288, Article ID 119629, 2021.

[16] L. M. P. Durão, D. J. S. Gonçalves, J. M. R. S. Tavares et al., "Drilling delamination outcomes on glass and sisal reinforced plastics," in *Materials Science Forum*Trans Tech Publ, Switzerland, 2013.

[17] N. Feito, J. Díaz-Álvarez, J. López-Puente, and M. H. Miguelez, "Experimental and numerical analysis of step drill bit performance when drilling woven CFRPs," *Composite Structures*, vol. 184, pp. 1147–1155, 2018.

[18] A. Díaz-Álvarez, J. Díaz-Álvarez, N. Feito, and C. Santiuste, "Drilling of biocomposite materials: modelling and experimental validation," *Simulation Modelling Practice and Theory*, vol. 106, Article ID 102203, 2021.

[19] R. Vinayagamoorthy, I. V. Manoj, G. Narendra Kumar, I. Sai Chand, G. V. Sai Charan Kumar, and K. Suneel Kumar, "A central composite design based fuzzy logic for optimization of drilling parameters on natural fiber reinforced composite," *Journal of Mechanical Science and Technology*, vol. 32, no. 5, pp. 2011–2020, 2018.

[20] H. Rezghi Maleki, M. Hamedi, M. Kubouchi, and Y. Arao, "Experimental study on drilling of jute fiber reinforced polymer composites," *Journal of Composite Materials*, vol. 53, no. 3, pp. 283–295, 2019.

[21] H. Rezghi Maleki, M. Hamedi, M. Kubouchi, and Y. Arao, "Experimental investigation on drilling of natural flax fiber-reinforced composites," *Materials and Manufacturing Processes*, vol. 34, no. 3, pp. 283–292, 2019.

[22] N. Patel, K. Patel, V. Chaudhary, and P. Gohil, "Investigations on drilling of hybrid basalt/glass polyester composites," *Australian Journal of Mechanical Engineering*, vol. 2020, Article ID 1784560, 10 pages, 2020.

[23] S. Pradeep and T. Rajasekaran, "Cutting force analysis on drilling of natural fiber reinforced polymer composites material," in *Techno-Societal 2018*, pp. 561–571, Springer, Berlin, Germany, 2020.

[24] P. K. Bajpai and I. Singh, "Drilling behavior of sisal fiber-reinforced polypropylene composite laminates," *Journal of Reinforced Plastics and Composites*, vol. 32, no. 20, pp. 1569–1576, 2013.

[25] P. K. Bajpai, K. Debnath, and I. Singh, "Hole making in natural fiber-reinforced polylactic acid laminates," *Journal of Thermoplastic Composite Materials*, vol. 30, no. 1, pp. 30–46, 2017.

[26] M. Roy Choudhury, M. S. Srinivas, and K. Debnath, "Experimental investigations on drilling of lignocellulosic fiber reinforced composite laminates," *Journal of Manufacturing Processes*, vol. 34, pp. 51–61, 2018.

[27] Y. Turki, M. Habak, R. Velasco, and P. Vantomme, "Highlighting cutting mechanisms encountered in carbon/epoxy composite drilling using orthogonal cutting," *International Journal of Advanced Manufacturing Technology*, vol. 92, 2017.

[28] A. Díaz-Álvarez, Á. Rubio-López, C. Santiuste, and M. H. Miguélez, "Experimental analysis of drilling induced damage in biocomposites," *Textile Research Journal*, vol. 88, no. 22, pp. 2544–2558, 2018.

[29] D. Chandramohan and K. Marimuthu, "Drilling of natural fiber particle reinforced polymer composite material," *International Journal of Advanced Engineering Research and Studies*, vol. 1, no. 1, pp. 134–145, 2011.

[30] A. Belaadi, M. Boumaaza, S. Amroune, and M. Bourchak, "Mechanical characterization and optimization of delamination factor in drilling bidirectional jute fibre-reinforced polymer biocomposites," *International Journal of Advanced Manufacturing Technology*, vol. 111, no. 7, pp. 2073–2094, 2020.

[31] G. Rajaraman, S. K. Agasti, and M. P. Jenarthanan, "Investigation on effect of process parameters on delamination during drilling of kenaf-banana fiber reinforced in epoxy hybrid composite using Taguchi method," *Polymer Composites*, vol. 41, no. 3, pp. 994–1002, 2020.

[32] T. Panneerselvam, S. Raghuraman, T. K. Kandavel, and K. Mahalingam, "Evaluation and analysis of delamination during drilling on sisal-glass fibres reinforced polymer," *Measurement*, vol. 154, Article ID 107462, 2020.

[33] N. Abilash and M. Sivapragash, "Optimizing the delamination failure in bamboo fiber reinforced polyester composite," *Journal of King Saud University - Engineering Sciences*, vol. 28, no. 1, pp. 92–102, 2016.

[34] M. Ramesh, K. Palanikumar, and K. H. Reddy, "Influence of tool materials on thrust force and delamination in drilling sisal-glass fiber reinforced polymer (S-GFRP) composites," *Procedia Materials Science*, vol. 5, pp. 1915–1921, 2014.

[35] M. S. Huda, L. T. Drzal, A. K. Mohanty, and M. Misra, "Effect of fiber surface-treatments on the properties of laminated biocomposites from poly(lactic acid) (PLA) and kenaf fibers," *Composites Science and Technology*, vol. 68, no. 2, pp. 424–432, 2008.

[36] P. M. Kumar and K. Mylsamy, "A comprehensive study on thermal storage characteristics of nano-CeO2 embedded phase change material and its influence on the performance of evacuated tube solar water heater," *Renewable Energy*, vol. 162, pp. 662–676, 2020.

[37] H. Hocheng and C. Tsao, "Effects of special drill bits on drilling-induced delamination of composite materials," *International Journal of Machine Tools and Manufacture*, vol. 46, no. 12-13, pp. 1403–1416, 2006.

Research Article

Influence of Fiber Volume and Fiber Length on Thermal and Flexural Properties of a Hybrid Natural Polymer Composite Prepared with Banana Stem, Pineapple Leaf, and S-Glass

K. B. Prakash,[1] Yahya Ali Fageehi,[2] Rajasekaran Saminathan,[2] P. Manoj Kumar [ID],[3] S. Saravanakumar,[4] Ram Subbiah,[5] B. Arulmurugan,[3] and S Rajkumar [ID][6]

[1]*Department of Mechanical Engineering, Bannari Amman Institute of Technology, Sathyamangalam 638401, Tamil Nadu, India*
[2]*Department of Mechanical Engineering, College of Engineering, Jazan University, Jazan, Saudi Arabia*
[3]*Department of Mechanical Engineering, KPR Institute of Engineering and Technology, Coimbatore 641407, Tamil Nadu, India*
[4]*Department of Mechanical Engineering, M. Kumarasamy College of Engineering, Karur 639113, Tamil Nadu, India*
[5]*Department of Mechanical Engineering, Gokaraju Rangaraju Institute of Engineering and Technology, Hyderabad 500090, Telangana, India*
[6]*Department of Mechanical Engineering, Faculty of Manufacturing, Institute of Technolog, Hawassa University, Hawassa, Ethiopia*

Correspondence should be addressed to S Rajkumar; rajkumar@hu.edu.et

There is more demand for natural fiber-reinforced composites in the energy sector, and their impact on the environment is almost zero. Natural fiber has plenty of advantages, such as easy recycling and degrading property, low density, and low price. Natural fiber's thermal properties and flexural properties are less than conventional fiber. This work deals with the changes in the thermal properties and mechanical properties of S-glass reinforced with a sodium hydroxide-treated pineapple leaf (PALF) and banana stem fibers. Banana stem and pineapple leaf fibers (PALF) were used at various volume fractions, i.e., 30%, 40%, and 50%, and various fiber lengths of 20 cm, 30 cm, and 40 cm with S-glass, and their effects on the thermal and mechanical properties were studied, and their optimum values were found. It was evidenced that increasing the fiber volume and fiber length enhanced the flexural and thermal properties up to 40% of the fiber volume, and started to decrease at 50% of the fiber volume. The fiber length provides an affirmative effect on the flexural properties and a pessimistic effect on the thermal properties. The PALF S-glass combination of 40% fiber load and 40 cm fiber length provides maximum flexural strength, flexural modulus, storage modulus, and lowest loss modulus based on hybrid Taguchi grey relational optimization techniques. PALF S-glass hybrid composite has been found to have 7.80%, 3.44%, 1.17% higher flexural strength, flexural modulus, and loss modulus, respectively, and 15.74% lower storage modulus compared to banana S-glass hybrid composite.

1. Introduction

Due to the demand for lower dense material and green environment, fiber-reinforced composites (FRCs) have drawn more awareness towards the alternatives to metal-reinforced composites. Natural fibers are effectively utilized in polymer matrices as reinforcement [1]. Fillers such as particles or filaments are created with polymers to get items with the most needed mechanical, thermal, and electrical properties. The characteristics of natural composites are primarily subject to their particular fiber characteristics [2]. There are different variables, which influence the properties of the microstructural boundaries, such as fiber radius, length of fiber, fiber spread, fiber direction, loading weight of the fiber, and production method [3]. Natural fibers have more limitations, such as hydrophilic behavior, which leads to decreased adhesive properties [4]. In addition, natural fibers have more attraction to water particles from moisture,

and they are affected easily by ultraviolet rays, so more variations in their thermal and mechanical properties occur [5]. Hence, to limit these issues, researchers are focusing on natural-fiber-strengthened composites with polymer matrices.

The addition of natural fibers to polymers is referred to as hybrid composites. It overcomes the limitations and enhances the hindering properties of the natural and the polymer composites [6, 7]. Gowda et al. [8] worked on various types of natural fibers, i.e., silk, bamboo, kapok, coconut fiber, which were reinforced with polymer matrices and reported that the addition of natural fiber enhances the mechanical and thermal characteristics of the polymer matrices by 6–10%. Similarly, Abdul Karim et al. worked on various natural fibers, such as hemp, coir, and jute, and studied the properties of the mechanical and thermal characteristics of hybrid natural polymer composites and enhanced its properties to 4–8% [9]. Sheng and Gimbun found that an increment in the fiber volume fraction increases the flexural strength linearly from 4% to 6% up to 0.4 fiber fraction [10]. Jain et al. varied the fiber fraction from 0.1 to 0.3 and found that there is increment in tensile strength and flexural strength by 3–8% [11]. Chollakup et al. used the different fibers and found that PALF and banana fiber provides better mechanical and thermal properties [12]. Shih et al. conducted a study and discovered that the tensile and flexural strengths of PALF and banana fibers are approximately 80% and 50% higher, respectively, than the other fibers [13]. Asim et al. deliberated different fiber loadings with PALF and banana fibers resulting in flexural strength increase with an upsurge in fiber loading [14].

Nur et al. [15] investigated the influence of the fiber length and found that an increment in the PALF length intensifies the tensile strength and flexural strength of the composite by 8–12%. Aji et al. varied the fiber length and found that an increase in the fiber length increases the tensile strength and flexural strength by 8–12% [16]. Luo and Netravali varied the fiber length of the natural composites and found that there were significant effects on the thermal and mechanical properties [17]. Chollakup et al. discovered that the increment in the fiber length provides positive effects on the flexural and thermal properties up to a certain fiber length of 30 cm, after which it shows a counter-effect [18]. Lopattananon et al. varied the fiber length and found that the fiber length increases the loss of mass during the analysis of thermal characteristics [19].

The fiber loading and fiber length discover the drastic changes in the characteristics of the composites, and it creates both positive and negative effects [13, 20, 21]. The improvement was noticed in tensile strength, hardness, and strain modulus with an upsurge in the fiber volume, fiber length, and fiber type, respectively. The fiber fraction, fiber length, fiber type, and fiber treatment process are the significant elements influencing the properties of the composites [22–24]. Hence, it is a significant role being a researcher to study the effects of various compositions of natural fibers, their treatment methods, fiber length, and fiber volume on the mechanical and thermal properties [25, 26].

Natural fiber composites retain better thermomechanical and electrical properties if the interfacial bonds between the matrix and fiber are strong enough [27–29]. As of now, there is less data available on natural fiber reinforcement with S-glass polymer matrices; especially, there is no optimized data about the combination, which provides a better result of thermomechanical properties. The novelty of this work is that it pays special attention to determining the optimum mechanical and thermal characteristics of the polymer hybrid composites with various fiber loadings and different fiber lengths of banana stem, PALF, and S-glass.

2. Materials and Methods

2.1. Materials. Banana stems and pineapple leaves were taken as fiber materials, and their fiber lengths were chosen as 20 mm, 30 mm, and 40 mm. The S-glass fabric was selected as synthetic fiber with 600 gsm, and its size was fixed as 30 cm square. Epoxy resins were used as resins. The properties of materials are given in Table 1. The pineapple leaf was chemically treated with 6% sodium hydroxide, and it was immersed in it for 3 hours [30]. The banana leaf was also treated with the same method, and its immersion time was 2 hours. Then, it was dried in the furnace for 24 hours at 60°C, and it was weighted for the required volume as per equation (1) [19]. Naturally, untreated fibers tend to absorb moisture, which can cause delamination between the fibers and the polymer matrix and seriously affect the strength of the resulting composite material [31]. This is because natural fibers are hydrophilic, so their reinforcing effect can be minimized. Second, the hydrophobicity of the polyurethane matrix in conjunction with the hydrophilic fibers will lead to poor adhesion, phase separation, and limited stress load transfer in the composite foam [32]. Additionally, the presence of certain organic compounds (such as wax and pectin) found on the surface of these fibers can sometimes act as a barrier to destroy the effective interfacial adhesion between the filler and the polymeric matrix [33],

$$V_f = \frac{W_f/\rho_f}{\left(W_f/\rho_f\right) + \left(W_m/\rho_m\right)}, \qquad (1)$$

where V_f is the volume fraction of fiber (%), W_m and W_f are the mass of the matrix and fiber, respectively, and ρ_m and ρ_f refer to the density of the matrix and fiber, respectively.

The S-glass was kept in the middle layer to avoid stress concentration on a single point [34]. Hence, stresses were transferred to the natural fiber of both the bottom and top-sided fibers. As per the ASTM: D790 standard, flexural assessments were carried out.

2.2. Methods. The different sets of hybrid composites were made by the hot compression method as shown in Figure 1. The specimens prepared with different fiber volume fraction and fiber length are labelled as shown in Table 2.

A morphological investigation was accomplished to analyze the presence of interfacial attachment between the fiber and epoxy resin. Sample tests were covered with a skinny layer of gold, proceeded to scan to build the thermal

TABLE 1: Properties of tested materials.

Properties	Unit	S-glass fiber	Banana fiber	PALF fiber
Density (ρ)	kg/m^3	2500	1350	1520
Tensile strength	MPa	4570	212	413
Young's modulus	GPa	86	8	34
Elongation at the failure	—	2.8	2	1.6

FIGURE 1: Preparation of samples with a hot compression method.

TABLE 2: Prepared samples of the hybrid composite.

Combination	Symbolic representation	S-glass fiber	Banana fiber	PALF fiber	Fiber length
S-glass banana PALF	SGBP30	1	0.15	0.15	20
S-glass banana PALF	SGBP40	1	0.20	0.20	30
S-glass banana PALF	SGBP50	1	0.25	0.25	40
30% S-glass banana	SGB3020	1	0.3	—	20
30% S-glass banana	SGB3030	1	0.3	—	30
30% S-glass banana	SGB3040	1	0.3	—	40
40% S-glass banana	SGB4020	1	0.4	—	20
40% S-glass banana	SGB4030	1	0.4	—	30
40% S-glass banana	SGB4040	1	0.4	—	40
50% S-glass banana	SGB5020	1	0.5	—	20
50% S-glass banana	SGB5030	1	0.5	—	30
50% S-glass banana	SGB5040	1	0.5	—	40
30% S-glass PALF	SGP3020	1	—	0.3	20
30% S-glass PALF	SGP3030	1	—	0.3	30
30% S-glass PALF	SGP3040	1	—	0.3	40
40% S-glass PALF	SGP4020	1	—	0.4	20
40% S-glass PALF	SGP4030	1	—	0.4	30
40% S-glass PALF	SGP4040	1	—	0.4	40
50% S-glass PALF	SGP5020	1	—	0.5	20
50% S-glass PALF	SGP5030	1	—	0.5	30
50% S-glass PALF	SGP5040	1	—	0.5	40

and electrical conductivity, and to forestall electrostatic charging during test assessment. The pictures were examined to research the proper circulation of the natural fibers in the synthetic polymer matrix and their character of connection with one another. The flexural tests were accompanied to find the flexural strength and flexural modulus.

The flexural tests were piloted based on the ASTM standard D790 [35]. The specimen was supported by a support span, and the load was applied to the center by the loading nose, resulting in three-point bending at a set rate. The support span, loading speed, and maximum deflection for the test were the parameters for this test. As per the recommended

procedure, the ASTM D790 test was accomplished till the point of failure of the specimen. The thermogravimetric analyzer was used to record the variation in the thermal characteristics of the manmade hybrid composites based on their weight loss at different temperatures [36]. It measures the rate of change of material weight for different temperature profiles based on the effects of dehydration, decomposition, and oxidation. The dynamic mechanical investigation was carried out while examining the viscoelastic characteristics at various temperature profiles [37]. This investigation included the application of an oscillatory sprain at various temperatures.

3. Results and Discussion

3.1. Flexural Test. The condition of the samples before and after the flexural test is depicted in Figure 2. Three random samples from each fiber composition are presented in Figure 2(b) for better understanding. Flexural test results are presented in Figure 3. The flexural strength of the hybrid composite is nonlinear. It showed an increasing trend from 30% to 40%, and after 50% volume fraction, it started to decrease. The flexural strength of the S-glass/PALF hybrid composite was 18% higher than the S-glass/banana composite [23]. The maximum flexural strength of the SGP40 composite recorded at 20 cm, 30 cm, and 40 cm fiber lengths was 97.5 MPa, 103.6 MPa, and 112.3 MPa, respectively. As the fiber length of the hybrid composite upsurges, the flexural strength also increases linearly. The percentage strain of the composites decreases with the increase in the volume fraction of the glass fibers. Since the glass fiber is extremely brittle, the flexural strength of the composite increases with an increase in the fiber volume. The maximum flexural strength of the SGB40 composite recorded at 20 cm, 30 cm, and 40 cm fiber lengths were 94.5 MPa, 99.8 MPa, and 104.5 MPa, respectively. The increase in the fiber length of the SGB40 hybrid composite increases the mechanical flexural strength linearly. The greatest flexural strength of the SGBP composite recorded at 20 cm, 30 cm, and 40 cm fiber lengths were 62.5 MPa, 64.6 MPa, and 66.3 MPa, respectively. As the fiber length of the SGBP40 hybrid composite increases, the flexural strength also increases linearly. The same kinds of results were obtained and reported by Shen and Gimbun [28]. The reason for this phenomenon was characterized to the insufficient resin. Natural fibers are normally hydrophobic in nature, and they absorb more resin. Hence, insufficient resin led to a decrement in the flexural strength of the polymer hybrid composites, when the fiber volume was increased after 50%. The after-effects of the insufficient resin increased the brittleness, and hence, it started to fail permanently.

The flexural modulus results followed same as that of the flexural strength results, which are shown in Figure 4. It shows an increasing trend from 30% to 40%, and at 50% volume fraction, it started to decline. The stiffness of the hybrid composite would be better if the value of the flexural modulus is high. The flexural modulus of the SGP 40 has found to be superior (8.56 MPa) at 40 cm fiber length. The flexural modulus of the SGBP 40 has been obtained as

2.76 MPa at 40 cm fiber length, which is the lowest value ever. Hence, the determined results accredited that the SGP 40 would absorb more forces than the other hybrid composites [27]. The flexural modulus exhibited a decrement with the reduction in the fiber length due to high strain in the material.

3.2. Thermal Test. The thermogravimetric analysis was carried out between 30°C and 600°C at 10°C/min rate, and its results are presented in Figures 5(a)–5(c). The major degradation for SGB4030 occurred at the temperature between 288°C and 451°C. The peak degradation occurred at 381°C temperature. The degradation of the SGP4030 occurred at the temperature between 258°C and 426°C, and the peak happened at 342°C. The reason for the same is attributed to a different phase of degradation. The first phase of the weight loss occurred from 30°C to 100°C, and it may be due to the moisture evaporation. The subsequent phase occurred between 150°C and 430°C, and it was attributed to the process of decomposition. The next decomposition was hemicellulose decomposition, which started at 250°C and ended at 326°C. In addition, the cellulose decomposition was started. The thermal stability of the cellulose was accredited to their strong chemical structure. Furthermore, lignin decomposition started at 30°C and extended till 600°C. It can be understood that lignin has shown more thermal stability, and hence, it provided the toughness to the natural fibers [38].

The banana and S-glass hybrid composites possess higher thermal degradation temperature, and their mass loss was higher than the PALF and S-glass hybrid composites due to their higher fiber weight [38, 39]. Hence, SGB 3020, SBP3020, and SGBP 20 have shown lower thermal degradation temperatures. Figure 5 depicts that a decrease in the fiber length would cause a decrease in the mass loss of the hybrid composite. It can be understood that a low rate of decomposition of fiber would be the decline in the mass loss of the hybrid fiber composite.

3.3. Storage Modulus Test. The dynamic mechanical analyzer (V4.5A TA Model) was used to measure the thermal storage modulus. It is preferred because of its comparative effectiveness in measuring the storage modulus [40, 41]. The hybrid composites were heated from 30°C to 200°C, and their results were plotted as shown in Figures 6(a)–6(c). The results evidenced that owing to the less stiffness of the fiber, a slight variation in the storage modulus for the hybrid polymer composites happened. Furthermore, the storage modulus diminished with temperature for both the natural composites. Hence, the higher fiber volume caused to increase the stiffness of the hybrid composites. However, it demonstrated the waning of stiffness with the increase in temperature [42]. At the PALF fiber proportion of 40%, the least flexural modulus was recorded. It was observed that, if the fiber volume decreases, the storage modulus also decreases due to the mobility of molecules in natural fiber composites. The storage modulus decreased with the decrease in temperature of the glass fiber, and it was compensated with the reinforcement of banana fiber and PALF
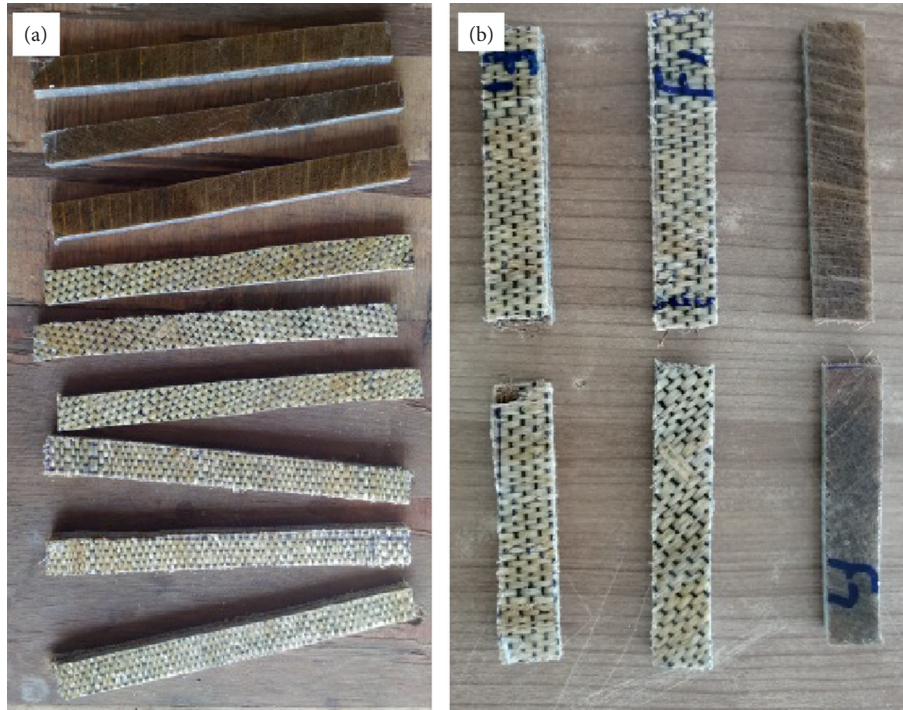
FIGURE 2: Flexural test specimens (a) before and (b) after the test.
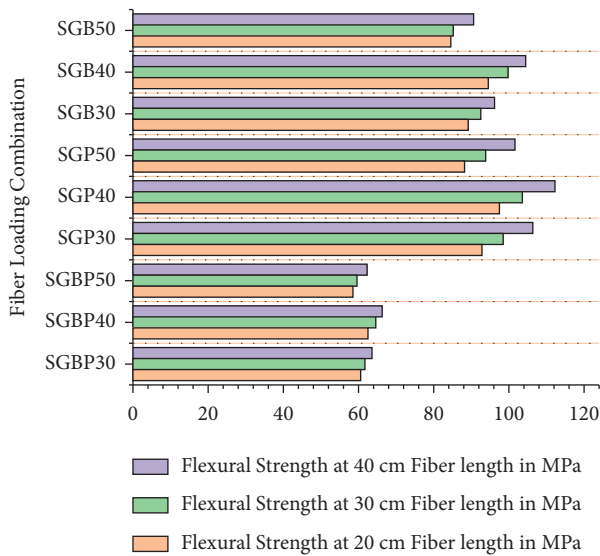
FIGURE 3: Graphical representation of flexural strength for various samples at different fiber volumes and fiber lengths.
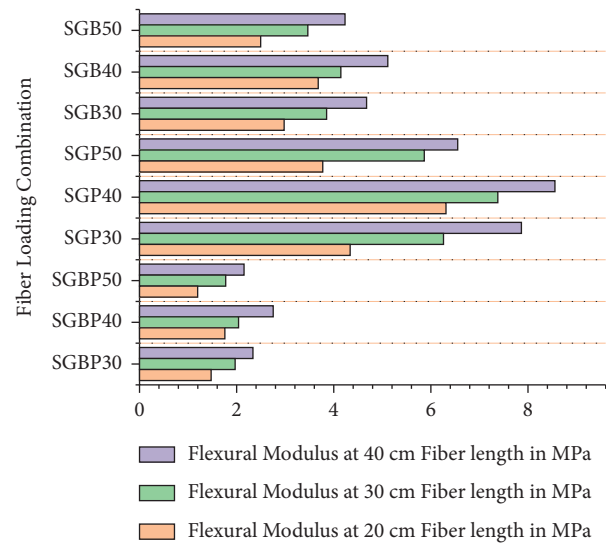
FIGURE 4: Graphical representation of flexural modulus for various samples at different fiber volumes and fiber lengths.

fiber. Because the thermal expansion coefficients of epoxy resin, banana fiber, and PALF fiber are all positive, it became the reason for the changes in mechanical and thermal properties. However, in the absence of residual stress, it has become responsible for a drop in the shear modulus for the increment in the fiber volume and fiber length.

3.4. Comparison. The present work is compared with the previous research work, which was piloted by Mohd Hanafee

Zin and Nurazzi Norizan [43] for the 40% fiber volume and 30 cm fiber length of banana, PALF-reinforced polymer matrix as presented in Table 3. They used E-glass fiber with banana stem and PALF. It is obvious that SGB4030 exhibited a 14.89 percent more flexural strength, 6.85 percent higher flexural strength, 3.95 percent higher loss modulus, 1.77 percent higher storage modulus than [43]. S-glass is a high-performance glass fiber that differs from E-glass fiber principally in terms of silica content. Silica, aluminium, and magnesium oxides are abundantly found in S-glass fiber, and

(a)

(b)

(c)
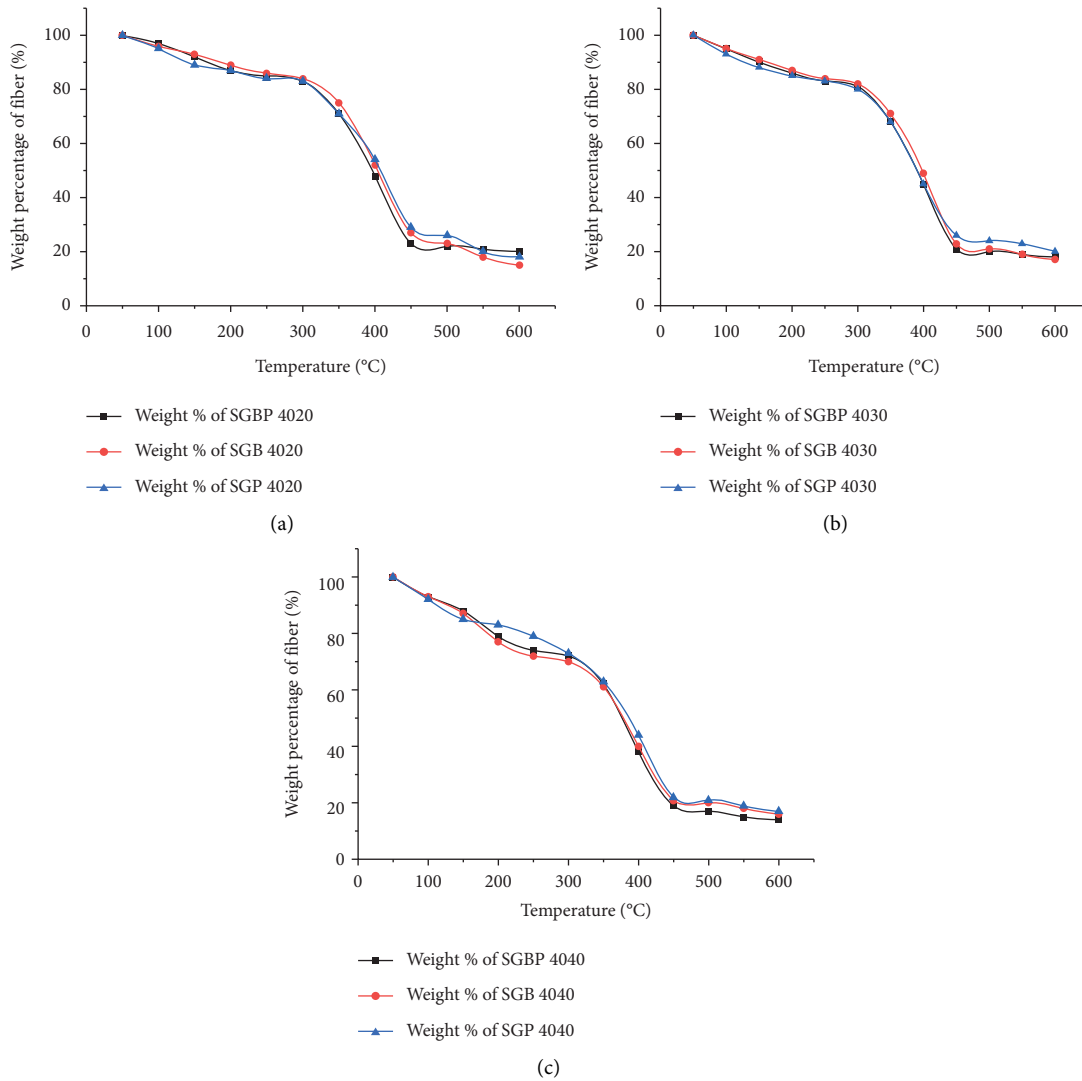
Figure 5: Graphical representation of weight percentage of 40% fiber volume sample at (a) 20 cm fiber length, (b) 30 cm fiber length, and (c) 40 cm fiber length.

hence, S-glass fibers are superior in terms of mechanical and thermal properties compared to E-glass fibers.

3.5. Optimization. Hybrid Taguchi Grey relational analysis (HTGRA) was used to find the optimum output parameters from the different input parameters as shown in Table 4. Initially, L27 design of experiments were selected with different combination of fiber type, fiber load, and fiber length. The test specimens were prepared as per the L27 Design of Experiments (Doe), and mechanical and thermal characteristics tests were performed as described in the earlier sections. The output responses (data from Table 5), i.e., flexural strength, flexural modulus, and storage modulus were first converted into a signal to noise ratio based on the

following first equation, and the percentage of mass loss was determined by the next equation [44, 45]:

$$\text{Larger the better}\left(\frac{S}{N}\right) = 10\,\text{Log}\left(\frac{1}{n}\sum_{i=1}^{n}\frac{1}{yi^2}\right), \tag{2}$$

$$\text{Smaller the better}\left(\frac{S}{N}\right) = 10\,\text{Log}\left(\frac{1}{n}\sum_{i=1}^{n}yi^2\right), \tag{3}$$

where "S/N" refers to signal to noise ratio, and "yi" refers to the output response of specific sequence. Then, the data from the S/N ratios were preprocessed using the following equations:

(a)

(b)

(c)
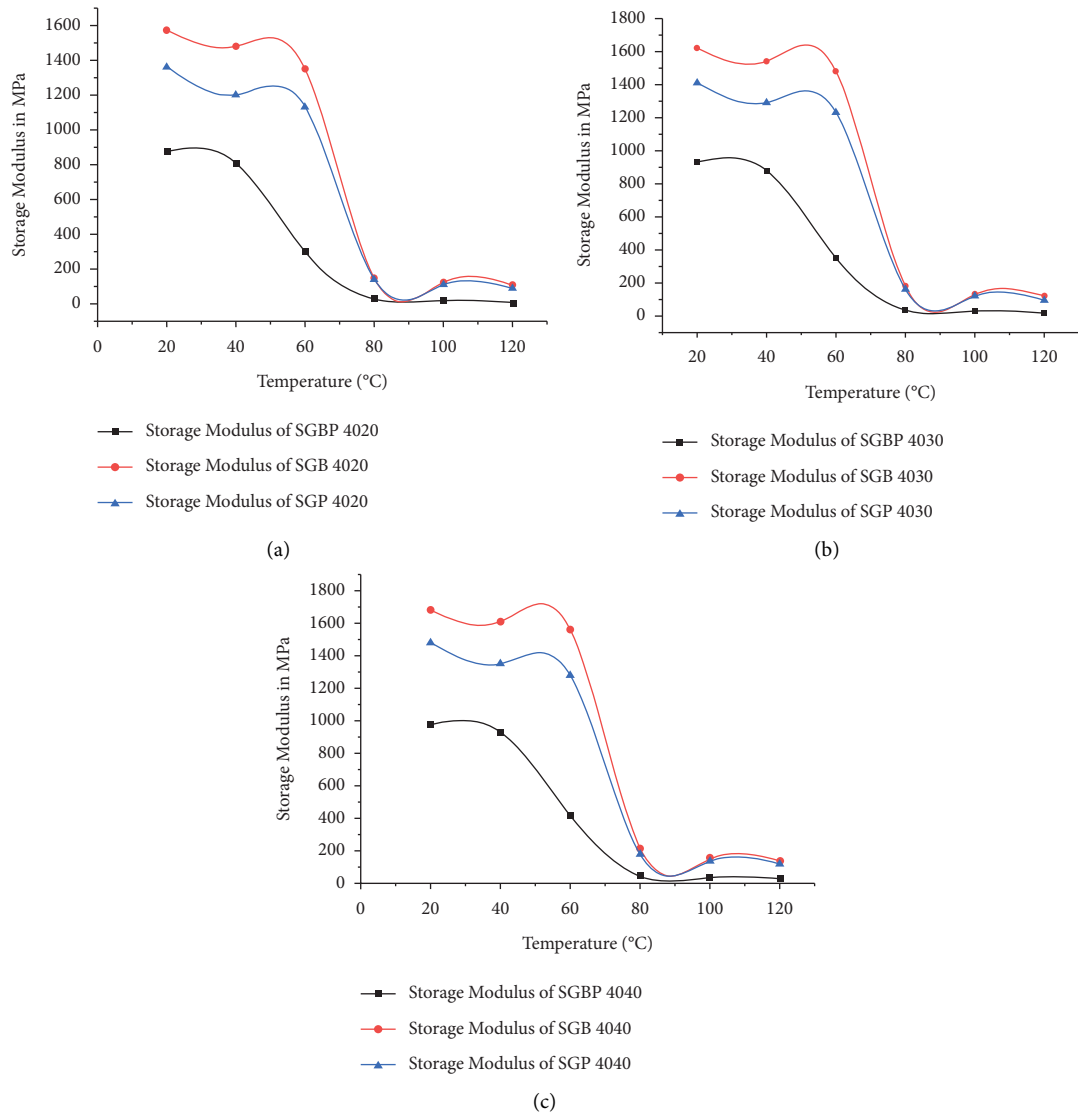
FIGURE 6: Graphical representation of storage modulus of sample at 40% fiber volume sample at (a) 20 cm fiber length, (b) 30 cm fiber length, and (c) 40 cm fiber length.

TABLE 3: Comparison of previous and current research work at 40% fiber volume and 30 cm fiber length.

Sl No	Parameters considered for study	Previous research work [43]		Current research work	
		Banana E-glass	PALF E-glass	Banana S-glass	PALF S-glass
1	Flexural strength (MPa)	90.95	105.10	104.5	112.3
2	Flexural modulus (MPa)	4.24	7.61	5.12	8.56
3	Loss modulus	91.73	70.81	87.23	78.4
4	Storage modulus (MPa)	77.94	61.16	79.32	63.58

TABLE 4: Input parameters.

Sl. No	Parameters	Level 1	Level 2	Level 3
1	Fiber combination	SGBP	SGP	SGB
2	Fiber volume	30%	40%	50%
3	Fiber length	20 cm	30 cm	40 cm

TABLE 5: Output responses (samples).

Sl No	Fiber combination (FC)	Fiber volume (FV) (%)	Fiber length (FL) (cm)	Flexural strength in MPa	Flexural modulus in MPa	Total % of mass loss	Storage modulus in MPa
1	SGP	30	20	92.8	4.35	78.72	99.31
2	SGP	30	30	98.5	6.26	83.56	97.43
3	SGP	30	40	106.3	7.87	85.27	96.85
4	SGP	40	20	97.5	6.32	81.46	68.53
5	SGP	40	30	103.6	7.38	85.87	65.72
6	SGP	40	40	112.3	8.56	88.4	63.58
7	SGP	50	20	88.2	3.78	80.56	74.35
8	SGP	50	30	93.9	5.87	84.25	71.53
9	SGP	50	40	101.6	6.56	86.94	68.25

$$\text{Larger the better } (xi)^* (k) = \frac{xi^{(o)} (k) - \min xi^{(o)} (k)}{\max xi^{(o)} (k) - \min xi^{(o)} (k)}, \tag{4}$$

$$\text{Smaller the better } (xi)^* (k) = \frac{\max xi^{(o)} (k) - xi^{(o)} (k)}{\max xi^{(o)} (k) - \min xi^{(o)} (k)}, \tag{5}$$

where $xi^{(o)} (k)$ is an output response value at original sequence, and $\max xi^{(o)} (k)$ is the largest value of sequence, and $\min xi^{(o)} (k)$ is the lowest value of that responses. Equation (4) was used for flexural strength, flexural modulus, and storage modulus as these values should be as large as possible. In addition, equation (5) was used for finding the percentage of mass loss responses as these values should be as small as possible [46, 47]. Then, the deviation sequence (ϵi (k)) was found using the following equations (ddistinguished coefficient (ϵ) was chosen as 0.5):

$$\Delta oi = \|xo^* (k) - xi^* (k)\|, \tag{6}$$

$$\epsilon i (k) = \frac{\Delta \min - \epsilon \Delta \max}{\Delta i (k) - \epsilon \Delta \max}. \tag{7}$$

Finally, grey relation grade (GRG) was calculated using equation (7) [48, 49]. GRG was given as input to the software Minitab 19, and then, the optimized parameter plot, regression equation, and R^2 values were found,

$$\text{GRG} = \frac{1}{n} \sum_{k=1}^{n} \epsilon i (k). \tag{8}$$

R^2 value was found to be 95.34%, and the predicted R^2 value was 89.10%. Hence, the model was found to be valid. Before calculating the R^2 values, the empirical correlations were created. At a 95% confidence level, all the coefficients were evaluated for significance. Using the Student's t-test,

Main Effects Plot for GRG

Data Means
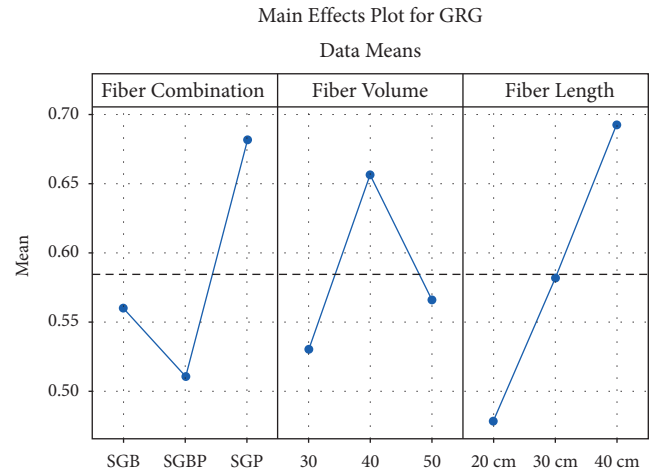
FIGURE 7: Graphical representation of the main effect plot on output response of input responses.

insignificant coefficients were removed without impacting the correctness of the empirical connections. In order to establish the final empirical relationships, the significant coefficients were taken into account. For all replies, the final developed empirical connections with processing components in the coded form are given in the following regression equation :

$$\begin{aligned} \text{Grey Relational Grade} = \{ & 0.5843 - 0.2141X1 - 0.0734X2 \\ & + 0.0975X3 - 0.0541Y1 \\ & + 0.0724Y2 - 0.0184Y3 \\ & - 0.1062Z1 - 0.0022Z2 \\ & + 0.1084Z3 \}, \end{aligned} \tag{9}$$

where X_1, X_2, and X_3 refer to the different levels of fiber combinations, Y_1, Y_2, and Y_3 are different fiber volume

Interaction Plot for GRG Data Means
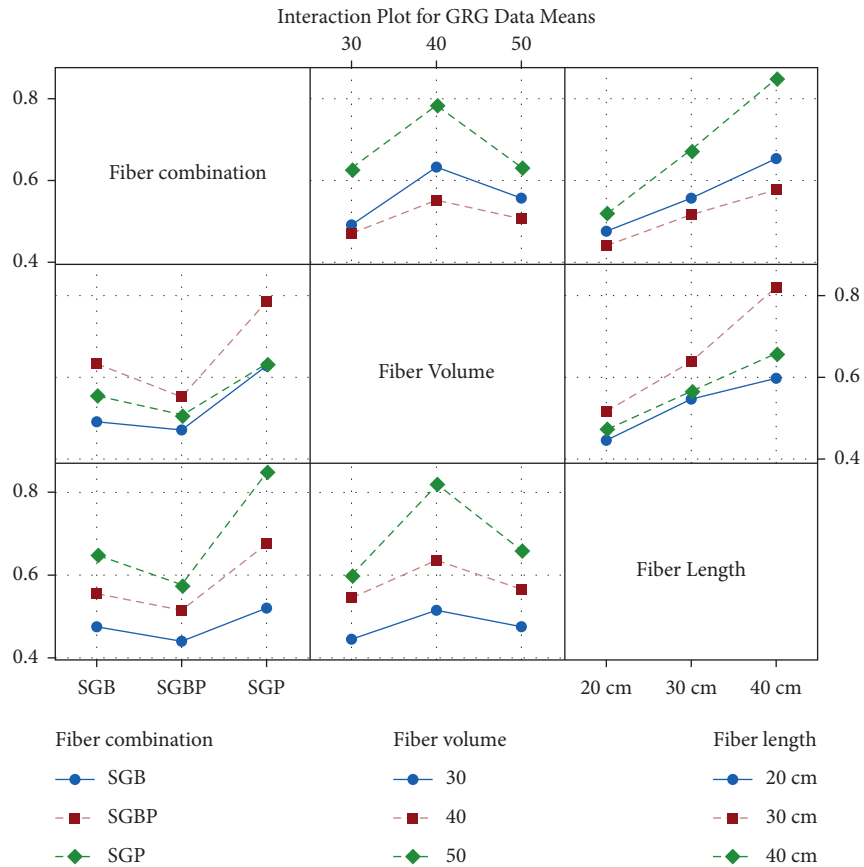
FIGURE 8: Graphical representation of the interaction effect plot on output response of different input responses.

levels, and Z_1, Z_2, and Z_3 are different levels of fiber length. Based on the GRG values, the main effects and the interaction effects of the input parameters were determined, and the best parameter settings were identified from the main effects plot of grey relational grade response as follows (Figure 7): S-glass PALF fiber combination, 40% fiber load, and 40 cm fiber length. According to the interaction effect plot as shown in Figure 8, there is no interaction effect between the input parameters even though S-glass PALF fiber combination, 40% fiber load, and 40 cm fiber length combination provides optimum mechanical and thermal properties. The HTGRA technique proposed a set of optimal input parameters, and the tests were carried out once again to validate the results. It yielded the GRG value of 0.796, and when compared it to the average values of the experimental results, GRG was raised by 0.015 percent during the confirmation test.

4. Conclusions

This work deals with the influence of fiber volume and length on mechanical and thermal properties of the polymer hybrid composite. The following inferences are drawn from the critical investigation:

(1) The increment in the fiber volume and fiber length induces the enhancement in the flexural and thermal characteristics of the hybrid composites. After

reaching 40% of the fiber volume, the mentioned characteristics started to decline. Furthermore, an increment in the fiber length always has positive effects on the mechanical and thermal properties.

(2) Based on the assessment of the mechanical properties, SGP4030 exhibited better flexural properties, i.e., flexural modulus and flexural strength of 8.6 MPa and 112.3 MPa, respectively. On the other hand, SGBP3020 registered a 6 MPa and 4.35 MPa of flexural strength and flexural modulus, respectively, which are the lowest values compared to other combinations. However, the flexural strength of SGB4030 was observed as 14.89% higher than the SEB4030. Similarly, the flexural strength of SGP4030 was 6.85% higher than the SEB4030.

(3) The assessment of the thermal properties revealed that SGB4020 and SGP4020 exhibited a low mass loss, and SGB4030 presented the higher storage modulus. The storage modulus of SGB4030 was perceived as 3.95% higher than the SEB4030. Likewise, the storage modulus of SGP4030 was 1.77% higher than the SEB4030.

(4) Hybrid Taguchi GRA techniques suggested that PALF-reinforced S-glass fiber with a 40% fiber volume and 40 cm fiber length provides the optimum mechanical and thermal properties compared to other combinations.

Data Availability

The data used to support the findings of this study are included within the article.

Conflicts of Interest

The authors declare that there are no conflicts of interest regarding the publication of this paper.

References

[1] S. Alsubari, M. Y. M. Zuhri, S. M. Sapuan, M. R. Ishak, R. A. Ilyas, and M. R. M. Asyraf, "Potential of natural fiber reinforced polymer composites in sandwich structures: a review on its mechanical properties," *Polymers*, vol. 13, no. 3, p. 423, 2021.

[2] S.-K. Yeh, C.-R. Hu, M. B. Rizkiana, and C.-H. Kuo, "Effect of fiber size, cyclic moisture absorption and fungal decay on the durability of natural fiber composites," *Construction and Building Materials*, vol. 286, 2021.

[3] S. Sekar, S. Suresh Kumar, S. Vigneshwaran, and G. Velmurugan, "Evaluation of mechanical and water absorption behavior of natural fiber-reinforced hybrid biocomposites," *Journal of Natural Fibers*, 2020.

[4] A. C. Manalo, E. Wani, N. A. Zukarnain, W. Karunasena, and K. T. Lau, "Effects of alkali treatment and elevated temperature on the mechanical properties of bamboo fibre-polyester composites," *Composites Part B: Engineering*, vol. 2015, no. 80, pp. 73–83.

[5] K. Makhijani, R. Kumar, and S. K. Sharma, "Biodegradability of blended polymers: a comparison of various properties," *Critical Reviews in Environmental Science and Technology*, vol. 45, no. 16, pp. 1801–1825.

[6] H. A. McKenna, J. W. S. Hearle, and N. O'Hear, *Handbook of Fibre Rope Technology*, Woodhead Publishing in Textiles, Cambridge, England, 2004.

[7] G. Basu, A. N. Roy, and A. N. Roy, "Blending of jute with different natural fibres blending of jute with different natural fibres," *Journal of Natural Fibers*, vol. 4, no. 4, 2008.

[8] Y. Gowda, T. Girirajappa, S. M Rangappa, J. Parasmeswaranpillai, and S. SiengChen, "Natural fiber as a sustainable and renewable energy development of eco friendly composites: a Comprehensive Review," *Front matter*, vol. 6, pp. 1–14, 2019.

[9] M. R. Abdul Karim, D. Thair, E. U Haq, A. Hussain, and M. S. Malik, "Natural fiber as a promising environmental friendly reinforcements for polymer composites," *Polymer Composites*, vol. 29, pp. 1–24, 2020.

[10] F. T. Sheng and J. Gimbun, "Strengthening performance of PALF-epoxy composite plate on reinforced concrete beams," *IOP Conference Series: Materials Science and Engineering*, pp. 1–9, 2017.

[11] J. Jain, S. Jain, and S. Sinha, "Characterization and thermal kinetic analysis of pineapple leaf fibers and their reinforcement in epoxy," *Journal of Elastomers and Plastics*, vol. 51, no. 3, pp. 1–12, 2018.

[12] R. Chollakup, H. Askanian, and F. Delor-Jestin, "Initial properties and ageing behaviour of pineapple leaf and palm fibre as reinforcement for poly propylene," *J thermoplastic Compos Mater*, vol. 30, no. 2, pp. 174–195, 2017.

[13] Y. F. Shih, W. C. Chang, W. C. Liu, C. C. Lee, C. S. Kuan, and Y. H. Yu, "Pineapple leaf/recycled disposable chopstick hybrid fiber-reinforced biodegradable composites," *Journal of Taiwan, Institute of Chemical Engineering*, vol. 45, pp. 2039–2046, 2014.

[14] M. Asim, M. Jawaid, K. Abdan, M. I. Ridzwan, M. R. Ishak, and O. Y. Alothman, "Effect of hybridization on the mechanical properties of pineapple leaf fibre/kenaf phenolic hybrid composites," *Journal of Renew Mater*, vol. 6, 2017.

[15] S. Nur, R. Ramli, and U. Teknikal, "The effect of alkaline treatment and fiber length on pineapple leaf fiber reinforced poly lactic acid biocomposite," *Journal of Teknol*, vol. 79, pp. 111–125, 2017.

[16] I. S. Aji, E. S. Zainudin, A. Khalina, S. M. Sapuan, and M. D. Khairul, "Studying the effect of fiber size and fiber loading on the mechanical properties of hybridized kenaf/PALF-reinforced HDPE composite," *Journal of Reinforced Plastics and Composites*, vol. 30, pp. 546–553, 2011.

[17] S. Luo and A. N. Netravali, "Mechanical and thermal properties of environment-friendly "green" composites made from pineapple leaf fibers and poly (hydroxy butyrate-co-valerate) resin," *Polymer Composites*, vol. 20, no. 3, pp. 367–378, 1999.

[18] R. Chollakup, R. Tantatherdtam, S. Ujjin, and K. Sriroth, "Pineapple leaf fibre reinforced thermoplastic composites: effects of fibre length and fibre content on their characteristics," *Jornal of Applied Polymer Science*, vol. 119, no. 4, 1952.

[19] N. Lopattananon, K. Panawarangkul, K. Sahakaro, and B. Ellis, "Performance of pine apple leaf fiber-natural rubber composites: the effect of fiber surface treatments," *Journal of Applied Polymer Science*, vol. 102, no. 2, pp. 1974–1984.

[20] N. Graupner, G. Ziegmann, F. Wilde, F. Beckmann, and J. Müssig, "Procedural influences on compression and injection moulded cellulose fibre-reinforced polylactide (PLA) composites: influence of fibre loading, fibre length, fibre orientation and voids," *Compos Applied Science Manuf*, vol. 81, pp. 158–171, 2016.

[21] M. F. M. Alkbir, S. M. Sapuan, A. A. Nuraini, and M. R. Ishak, *Fibre Properties and Crash Worthiness Parameters of Natural Fibre-Reinforced Composite Structure:*, Elsevier, Amsterdam, Netherlands, 2016.

[22] M. F. Zainuddin, S. Rosnah, M. M. Noriznan, and I. Dahlan, "Effect of moisture content on physical properties of animal feed pellets from pineapple plant waste," *Agriculture and Agriculture Science Procedia*, vol. 2, pp. 224–230, 2014.

[23] K. L. Pickering, M. G. A. Efendy, and T. M. Le, "A review of recent developments in natural fibre composites and their mechanical performance," *Composite Applied Science Manufacturing*, vol. 83, pp. 98–112, 2016.

[24] Y. F. Shih, J. X. Cai, C. S. Kuan, and C. F. Hsieh, "Plant fibers and wasted fiber/epoxy green composites," *Composites Part B: Engineering*, vol. 43, no. 7, pp. 2817–2821, 2012.

[25] N. Kengkhetkit and T. Amornsakchai, "Utilisation of pineapple leaf waste for plastic reinforcement: 1. A novel extraction method for short pineapple leaf fiber," *Industrial Crops and Products*, vol. 40, no. 1, pp. 55–61, 2012.

[26] A. Kalapakdee and T. Amornsakchai, "Mechanical properties of preferentially aligned short pineapple leaf fiber reinforced thermoplastic elastomeric: effects of fiber content and matrix orientation," *Polymer Testing*, vol. 37, pp. 36–44, 2014.

[27] A. N. Kasim, M. Z. Selamat, N. Aznan et al., "Effect of pineapple leaf fiber loading on the mechanical properties of pine apple leaf fiber – polypropylene composite," *Journal of Teknol*, vol. 77, no. 21, pp. 117–123, 2015.

[28] F. T. Sheng and J. Gimbun, "Strengthening performance of PALF-epoxy composite plate on reinforced concrete beams," *IOP conference series: materials science and engineering*, vol. 318, 2017.

[29] K. Z. M. A. Motaleb, M. d. Shariful Islam, and M. B. Hoque, "Improvement of physic-mechanical properties of pineapple leaf fiber reinforced composite," *International Journal of Biomater*, vol. 2018, Article ID 7384360, 7 pages, 2018.

[30] W. Liu, M. Misra, P. Askeland, L. T. Drzal, and A. K. Mohanty, ""Green" composites from soy based plastic and pineapple leaf fiber: fabrication and properties evaluation," *Polymer*, vol. 46, no. 8, pp. 2710–2721, 2005.

[31] S. Kaewpirom and C. Worrarat, "Preparation and properties of pineapple leaf fiber reinforced poly (lactic acid) green composites," *Fibers and Polymers*, vol. 15, no. 7, pp. 1469–1477, 2014.

[32] A. Kalambettu, A. Damodaran, S. Dharmalingam, A. Kalambettu, and D. S. DamodaranA, "Evaluation of biodegradation of pineapple leaf fiber reinforced PVA composites," *Journal of Natural Fibers*, vol. 12, no. 1, pp. 39–51, 2015.

[33] W. Smitthipong, R. Tantatherdtam, and R. Chollakup, "Effect of pineapple leaf fiber-reinforced thermoplastic starch/poly(lactic acid) green composite: mechanical, viscosity, and water resistance properties," *Journal of Thermoplastic Composite Materials*, 2015.

[34] D. Mathivanan, H. Norfazilah, J. P. Siregar, M. R. M. Rejab, D. Bachtiar, and T. Cionita, "The study of mechanical properties of pineapple leaf fibre reinforced tapioca based bio plastic resin composite," *MATEC Web Conferences*, vol. 74, pp. 5–8, 2016.

[35] N. M. Barkoula, B. Alcock, N. O. Cabrera, and T. Peijs, "Poly(lactic acid) composites reinforced with leaf fibers from ornamental variety of hybrid pineapple (Potyra)," *Polymers and Polymer Composites*, vol. 16, no. 2, pp. 101–113, 2017.

[36] M. K. Gupta and R. K. Srivastava, "Mechanical properties of hybrid fibers-reinforced polymer composite: a review," *Taylor & Francis*, vol. 55, 2016.

[37] S. Rathika, K. Palanikumar, P. S. S. Raghavan, S. Rathika, K. Palanikumar, and P. S. R. ., "Physical performance of sisal-PALF-banana/glass fiber reinforced polyester hybrid composites," *Asian Journal of Chemistry*, vol. 2, no. 4, pp. 21–36, 2012.

[38] C. Ngaowthong, K. Mongkut, T. Nor, and R. View, "Effect of Dielectric Barrier Discharge Plasma Surface Treatment on the Properties of Pineapple Leaf Fiber Reinforced Poly(La," *Materials Science Forum*, vol. 862, 2016.

[39] S. H. Sheikh MdFadzullah, Z. Mustafa, S. N. R. Ramli, Q. Yaacob, and Y.A. F. Mohamed, "Preliminary study on the mechanical properties of continuous long pineapple leaf fibre reinforced PLA bio composites," *Key Engineering Materials*, vol. 694, pp. pp18–22, 2016.

[40] T. T. Nagarajan, A. S. Babu, K. Palanivelu, and S. K. Nayak, "Mechanical and thermal properties of PALF reinforced epoxy composites," *Macromolecular Symposia*, vol. 361, no. 1, pp. 57–63, 2016.

[41] P. Suwanruji, T. Tuechart, W. Smitthipong, and R. Chollakup, "Modification of pine apple leaf fiber surfaces with silane and isocyanate for reinforcing thermoplastic," *Journal of Thermoplastic Composite Materials*, vol. 30, no. 10, pp. 1344–1360, 2017.

[42] D. Puglia, J. Biagiotti, and J. M. Kenny, "A review on natural fibre-based composites — Part II: application of natural reinforcements in composite materials for automotive industry," *Journal of Natural Fibers*, vol. 1, 2008.

[43] K. A. Mohd Hanafee Zin and M. Nurazzi Norizan, "The effect of different fiber loading on flexural and thermal properties of banana/pine apple leaf (PALF)/glass hybrid composite," *Structural Health Monitoring of Biocomposites, Fibre-Reinforced Composites and Hybrid Composites*, pp. 1–17, 2019.

[44] R. Viswanathan, S. Ramesh, S. Maniraj, and V. Subburam, "Measurement and multi-response optimization of turning parameters for magnesium alloy using hybrid combination of Taguchi-GRA-PCA technique," *Measurement*, vol. 159, Article ID 107800, 2020.

[45] T. K. Mulenga, A. U. Ude, and C. Vivekanandhan, "Techniques for modelling and optimizing the mechanical properties of natural fiber composites: a review," *Fibers*, vol. 9, p. 6, 2021.

[46] O. Smith Onyekwere, M. H. Oladeinde, and R. O. Edokpiab, "Multi-Response optimization of bamboo fiber reinforced unsaturated polyester composites using hybrid Taguchi – grey relational analysis method," *Journal of Industrial and Production Engineering*, pp. 98–107, 2020.

[47] N. M. Mehat, S. Kamaruddin, and Abdul Rahim Othman, "Hybrid integration of Taguchi parametric design, grey relational analysis, and principal component analysis optimization for plastic gear production," *Chinese Journal of Engineering*, vol. 2014, Article ID 351206, 11 pages, 2014.

[48] B. Singaravel, S. Deva Prasad, K. Chandra Shekar, K. Mangapathi Rao, and G. Gowtham Reddy, "Optimization of process parameters using hybrid Taguchi and VIKOR method in electrical discharge machining process," in *Advanced Engineering Optimization through Intelligent Techniques Computing, vol 949*, R. Venkata Rao and J. Taler, Eds., Advances in Intelligent Systems and Springer, New York, NY, USA, 2020.

[49] T.-P. Dao, "Multiresponse optimization of a compliant guiding mechanism using hybrid taguchi-grey based fuzzy logic approach," *Mathematical Problems in Engineering*, vol. 2016, Article ID 386893, 17 pages, 2016.

Research Article

Finite Element Analysis of Temperature Distribution and Stress Behavior of Squeeze Pressure Composites

P. Gurusamy,[1] T. Sathish ⓘ,[2] V. Mohanavel ⓘ,[3] Alagar Karthick ⓘ,[4] M. Ravichandran ⓘ,[5] Omaima Nasif,[6] Saleh Alfarraj,[7] Velu Manikandan,[8] and S. Prasath ⓘ[9]

[1]*Department of Mechanical Engineering, Chennai Institute of Technology, Chennai 600069, India*
[2]*Department of Mechanical Engineering, Saveetha School of Engineering, SIMATS, Chennai 602105, Tamilnadu, India*
[3]*Centre for Materials Engineering and Regenerative Medicine, Bharath Institute of Higher Education and Research, Chennai 600073, Tamilnadu, India*
[4]*Department of Electrical and Electronics Engineering, KPR Institute of Engineering and Technology, Coimbatore 641407, Tamilnadu, India*
[5]*Department of Mechanical Engineering, K. Ramakrishnan College of Engineering, Tiruchirappalli 621112, Tamilnadu, India*
[6]*Department of Physiology, College of Medicine and King Khalid University Hospital, King Saud University Medical City, P.O. Box 2925, Riyadh 11461, Saudi Arabia*
[7]*Zoology Department, College of Science, King Saud University, Riyadh 11451, Saudi Arabia*
[8]*College of Environmental & Bioresource Sciences, Jeonbuk National University, Iksan 570752, Republic of Korea*
[9]*Department of Mechanical Engineering, College of Engineering and Technology, Mizan Tepi University, Tepi Campus, Tepi 121, Ethiopia*

Correspondence should be addressed to S. Prasath; prasath@mtu.edu.et

Aluminium-reinforced composites play a vital role in the engineering industry because of their better strength and stiffness. The properties are directly related to the solidification phenomenon of the cast alloy. The design engineer should understand the importance of the solidification behavior of base alloy and its reinforcement. Composites' solidification study is rare, and the reviews are limited. The solidification process is analyzed using the finite element method (FEM), and this would fetch a lot of information about the cooling rate of the composites and also helps to reduce the time in experimentation. This paper reports and plots the cooling curves of Al/SiC$_p$ composites using simulation software. Cylindrical-shaped composites were developed using the squeeze casting method, and the experimental cooling curves were plotted using a K-type thermocouple. Composites samples were prepared at the following squeeze pressures: 0, 30, 50, 70, 100, and 130 MPa; melt and die temperature was kept constant at 800 and 400°C, respectively. The experimental and FEA cooling curves were compared, and it was agreed that the increase in the squeeze pressure increases the cooling rate of the developed composite. Furthermore, the effect of temperature distribution from the inner region of the melt and die material which causes the radial and tangential stress of components has also been examined.

1. Introduction

Aluminium alloys, reinforced with SiC, have become an essential material that is used in a wide range of applications in the aviation, marine, electronic packaging, defence, and automobile industries [1]. The nature of the matrix metal is generally soft which contains good mechanical and thermal properties. The most common metals are aluminium, copper, titanium, magnesium, etc. The standard properties offered by the metals are malleability, ductility, fatigue strength, machinability, and thermal and electrical conductivity. The reinforcing material has to offer strong bonding to the metal in order to make the composite tensile, and the stiffness to weight ratio and strength to weight ratio is higher than the metal matrices. The hard and robust nature is obtained when the correct amount of the

reinforcements is added to the matrix. The particle-reinforced metal matrix composites exhibit better physical and mechanical properties; it can be modified to reach metallurgist requirements. Also, this material can show excellent thermophysical properties due to which it has been used in all the structural applications. It can pose a tremendous amount of strength at high-temperature applications; the capability to reveal low thermal shock and excellent wear resistance at less weight is the unique characteristics. There are many manufacturing methods to produce MMCs on which solid- and liquid-state processing is the promising route for developing the composites [2]. In solid-state processing, the interfacial reaction between base alloy and ceramic particles is not right in agreement. Hence, liquid-state processing can resolve this issue through stir casting. Further improving the better properties of the composites, the process adopts the squeeze casting method. It is a method to remove shrinkage and porosity during the liquid-state processing of composites. Hence, near net shape components are fabricated by this method [3].

Ghomashchi and Vikhrov [4] reported that the essential parameters for fabricating any alloys using squeeze casting routes are melt temperature, die temperature, and application of pressure, the main premise for this research. The base alloy's temperature, heat transfer coefficient, thermal conductivity, die temperature, and pressure during solidification would change the phase relationship of any alloy system. Thus, the application of pressure helps to decrease the interatomic movement during the process of solidification, which allows changes in the temperature of the melt. Many other factors would influence increase of the pressure, which are impurities, trace elements, and intersolubility of constituents' elements. Yue and Chadwick [5] have observed that the application of pressure would reduce the gap between the mould and melt, which leads to a more significant cooling rate. It influences the cooling rate. In permanent mould casting, due to the surface contact between the mould and casting, the cooling rate and solidification time must be considered for better results [6]. The mechanical properties of the casting are derived from the solidification time of the casting. Sukumaran et al. [7] investigated the squeeze cast A2124 alloy with 10% ceramic particles with increasing pressure during solidification of alloy and the developed composite. He reported that the application of pressure directly relates to the enhancement of composites. The applied pressure of about 100 MPa has created uniform particle distribution and other factors such as porosity and shrinkages and obtained fine refinement of microstructure. Furthermore, he reported that the squeeze pressure coupled with die temperature is increased; the heat transfer rate in composites is higher compared with that of the base alloy. The heat transfer rate is directly related to the amount of particles present in the alloys, which decides the cooling rate of the composite. Hanumanth and Irons [8] have reported that particle distribution can increase the cooling rate up to a certain percentage of reinforcing particles; after that, the cooling rate is decreased. Increasing the particles reduces the heat transfer rate in the melt, which causes the thermal diffusivity of the composite to reduce. Studies by Rajan et al. [9] have shown varying volume fractions of graphite and SiC particles with AA6082 alloy in the sand, steel, and graphite moulds, and heat transfer at casting and mould interface is also investigated. The heat transfer rate is enhanced due to the addition of one percent of magnesium particles in the aluminium alloy; this increases the wettability between the particle and the base alloy. The magnesium particles can be useful for hunting the oxide layer as well as increasing the interfacial reaction between the melt and the mould. Many researchers found, during the study of interfacial reaction, that the effect of intermetallic compounds plays a vital role. Zhou [10] reveals that the intermetallic compounds (Al_4C_3) would decrease when the solidification process is disturbed, which means it affects the fluidity of the materials. The compunds are varied with respect to the base alloy. Studies on Al and Graphene-bonding strength and wettability literature are not enough so far, these two intermetallic compounds, such as Al_4C_3 and Al_2O_3, are helping the base alloy in terms of transferring loads [10–12]. Li et al. [13] claimed that no evidence had noticed the formation of Al_4C_3 between Al and graphene nanoplatelets (GNPs). Nonetheless, stacking faults were observed near the Al matrix, which could be the reason for the strengthening of composites. Incorporating metal reinforcement (Cu-GNPs and Ni-GNPs) along with GNPs would enhance the strength of the composite; perhaps, the metal particles could have stopped the formation of Al_4C_3 [14]. Liu et al. [15] reported that the application of pressure would enhance the interface strength of Al/Mg-based composites. The intermetallic compounds are directly related to the cooling rate of the composites, and the application of squeeze pressure enhances the cooling rate of the composite [16]. The effect of intermetallic compound (Al_4C_3) is modeled with the help of Ansys software, and the impact of that is compared with the rule of mixture predictions. No significant results have been found in the Al-Si/CNT composites [17].

There are many studies based on fracture behaviour, interpenetrating with some structure models, simulation of moulds [18, 19], addition of particles with base alloy [20–22], and mechanical properties of particles [23–25] and using the finite element method. The study based on the solidification and cooling rate of the composites is highly complicated. Because, during the solidification process, the complex shapes' grain refinement and the features of microstructures are changed. Also, there are many studies which are focused only on the base alloy cooling rate and solidification process. This study gives importance of two different materials' solidification process because of its different behaviours. Hence, the squeeze casting process would give better results and integrate the cooling rate and microstructural features. There is a lack of information regarding the application pressure on the solidification study of cast composites, which is an essential feature in the high-pressure die casting industry. Therefore, the present work focuses on both experimental and theoretical research on the solidification of AA6082 composites with temperature behaviour and stress behaviour using the finite element method.

2. Boundary Conditions for the Cylindrical Model

The cooling curves have been plotted by the simulation software-ANSYS (version 19.2). Structural analysis, followed by thermal analysis, is carried out by the coupled field analysis. Hence, the structural and thermal capability of the element (PLANE 13) is used. Thus, each node has up to four-degree degrees of freedom. In this study, first, nonlinear thermal analysis was carried out, and then, static stress analysis was carried out. The half portion of a cylinder with the melt model was plotted for this symmetrical problem. Figure 1 shows the two-dimensional model of casting with the melt with its dimensions. The thermophysical properties of ceramic materials and AA6082 are shown in Table 1. The processing conditions for the preparation of cast samples are listed in Table 2. Tables 3 and 4 show die and ceramic material properties [9, 26]. Table 5 shows the boundary conditions of the FEA model. Convection properties were initially given to the model, and the initial room temperature is also applied to the die wall. Figure 2(a) shows the model for melt and die without boundary conditions, and Figure 2(b) shows the convection boundary condition for the die material. The rule of mixture was used to calculate the thermal conductivity of the composite. In contrast, the value of enthalpy is considered as the same value of base alloy because there is no phase change or ceramic material [22]. A step-by-step process of the solidification process concerning time is established by solution control. Finally, the cooling curve is plotted with the help of a time-history processor.

3. Experimental Work

The base plate width was 120 mm, the die inner diameter was 50 mm, thickness was 35 mm, and height was 150 mm. Figure 3(a) shows the melt stirring with reinforcement setup, and Figure 3(b) shows the punch and die have been preheated. Figure 4(a) shows the baseplate and die, and Figure 4(b) shows the appropriate locations of thermocouples. Figure 4(c) shows the fabrication of the squeeze cast setup. The squeeze casting technique was adopted for fabricating the composites, as discussed in [3]. The temperature values were being recorded by K-type thermocouple, which was recorded every one second. Figure 4(d) shows the thermocouples in its exact locations. The data acquisition system was incorporated in the experimental setup to record all temperature values, precisely. The recorded values were transferred to the computer to draw solidification curves. Aluminium composites were fabricated with increasing pressures when the die and melt temperatures were 400 and 800°C, respectively.

4. Results and Discussion

4.1. Cooling Rate and Time. The temperature readings measured from the baseplate readings (T_0 to T_2) are used to plot cooling curves and solidification time. In contrast, the die materials' temperature readings (T_3 to T_5) are used to measure the temperature distribution of the die. The
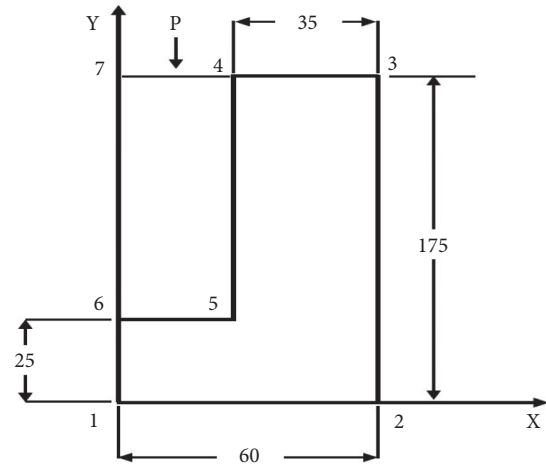
Figure 1: The cylindrical model with BCs for the die temperature of 400°C (melt temperature 800°C and pressure 130 MPa).

Table 1: Chemical composition of AA6082 aluminium alloy.

Element	Si	Fe	Cu	Mn	Mg	Cr	Zn	Ti	Al
Weight (%)	1.0	0.60	0.10	0.5	0.7	0.25	0.10	0.20	Bal

Table 2: Process conditions for composites.

Die temperature (°C)	Matrix temperature (°C)	Pressure (MPa)
400	800	0, 30, 50, 70, 100, 130

temperature readings are used to determine the solidification time for any type of cast alloy [26].

Increasing the pressure decreases the solidification time from 60 seconds to 42 seconds [2]. Figure 5 shows the various squeeze pressures cooling curves for both experiment and FEA study of Al/SiCp composite. The cooling rate is observed from the experimental cooling curves, and the values are 2.28°C/s 2.52°C/s, 2.68°C/s, 2.87°C/s, 3.5°C/s, and 3.75°C/s for 0, 30, 50, 70, 100, and 130 MPa, respectively. The flattening region is the freezing zone, and it is clearly shown in Figure 5.

The melting range of AA6082 alloy in the solid state is 577°C and the liquid state is 615°C, and the experimental freezing range is closely agreed with that of Hanumanth and Irons [8]. Also, in squeeze casting, the application of pressure brings the melt to solidify first, and then, the cooling rate is decided by the location of the particle [27]. Maleki et al. [28] reported that the application of pressure enhances the die and melt contact surface, which promotes high heat transfer and cooling rate. Hence, increasing the pressure increases the cooling rate of the composite. The predicted cooling rates are 1.23°C/s, 1.31°C/s, 1.47°C/s, 1.81°C/s, 1.98°C/s, and 2.24°C/s for the squeeze pressure of 0, 30, 50, 70, 100, and 130 MPa, respectively. Particle and base alloy reaction, formation of air inside the mould and melt, aspirations, and flow velocity were not considered in this analysis. The mentioned factors have to be considered for the FEA study [22], even though the cooling rate is almost close to the experimental cooling rate.

TABLE 3: Properties of SiC [9].

Material	Thermal conductivity (W/m°C)	Density (kg/m³)	Specific heat (J/kg·k)
Silicon carbide	100	3200	1300

TABLE 4: Properties of H13 [26].

Material	Thermal conductivity (W/m°C)	Density (kg/m³)	Specific heat (J/kg·k)
AISI H13	28.6	7761	461

TABLE 5: Boundary conditions for the applied pressure of 130 MPa.

Key points	Variables (mm)	Parameters (°C)
1	$x = 0$; $y = 0$	$T_d = 400$
2	$x = 60$; $y = 0$	$T_d = 400$
3	$x = 60$; $y = 175$	$T_d = 400$
4	$x = 25$; $y = 175$	$T_m = 800$
5	$x = 25$; $y = 25$	$T_m = 800$
6	$x = 0$; $y = 25$	$T_m = 800$
7	$x = 0$; $y = 175$	$T_m = 800$

(a)   (b)
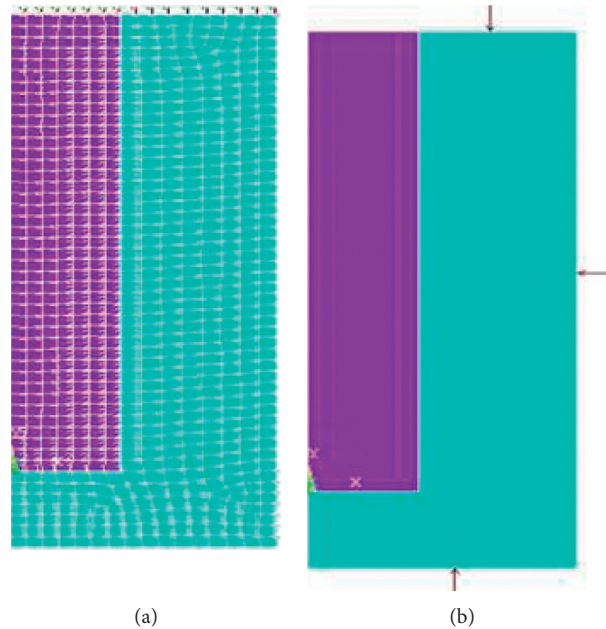
FIGURE 2: (a) FEA model of melt and die without BCs. (b) Convection boundary conditions of the FEA model.

4.2. Temperature Distribution and Thermal Stresses. To avoid multiple trial-and-error casting production or to avoid recreating the system repeatedly, the FEA-based analysis is recommended to fulfill the technical problems [13, 14]. Temperature distribution within the melt and distribution in the die are essential factors to identify the rate of the solidification process, mainly when the melt is in the application of pressure. Figure 6 shows the temperature dispersion in the composites at various squeeze pressures up to 800 seconds. From the FEA analysis, the observed values are 314°C, 318°C, 319°C, 321°C, 322°C, and 323°C for different

squeeze pressures 0, 30, 50, 70, 100, and 130 MPa, respectively. The amount of heat transfer is observed in the melt and reinforcement based on the applied pressure [29]. Hence, the temperature is varied based on the applied pressure.

It is important to focus complex shape engineering application-oriented castings, using design and solidification process using the finite element method. FEA is significant for casting industry because components' rejection leads to increase in cost of production. The finite element method is better in analyzing heat transfer of components within the
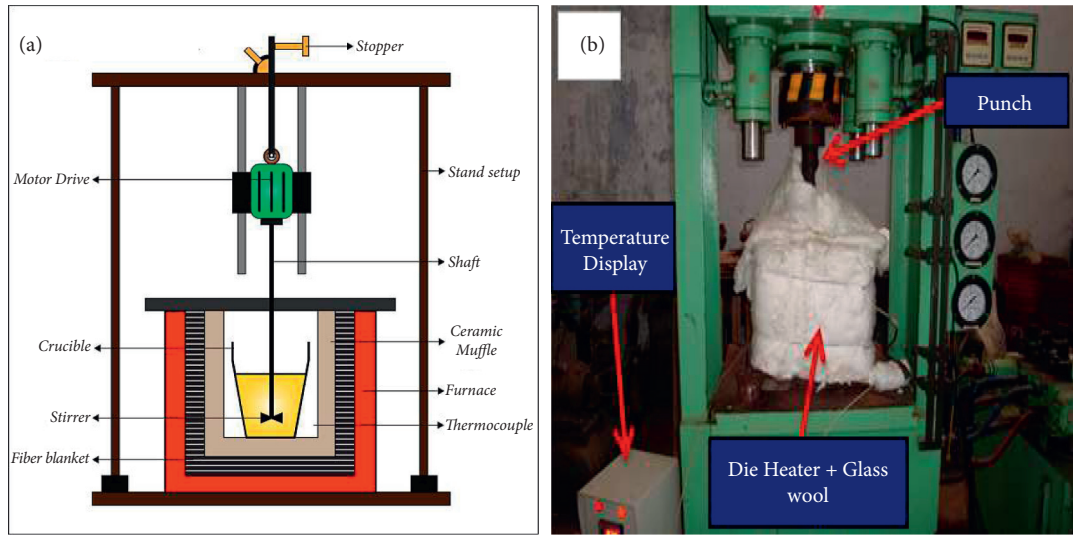
FIGURE 3: (a) Melt stirring setup. (b) Die and punch preheating for the preparation of composite.
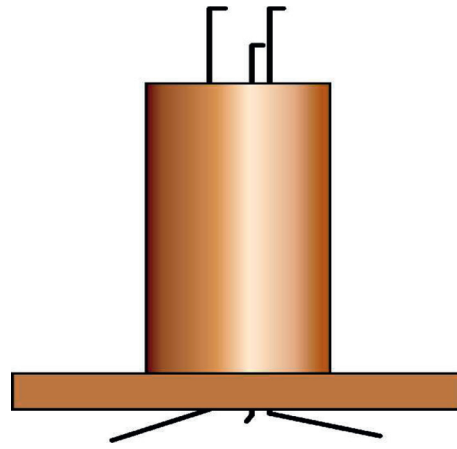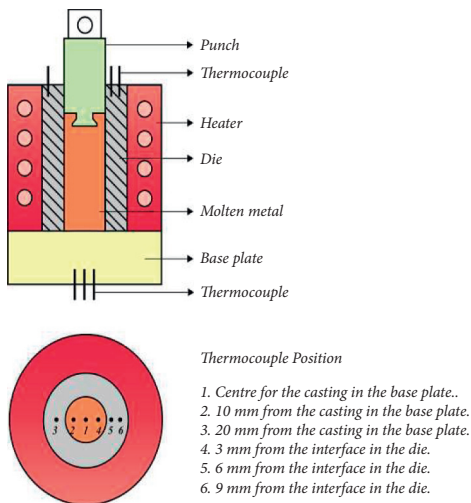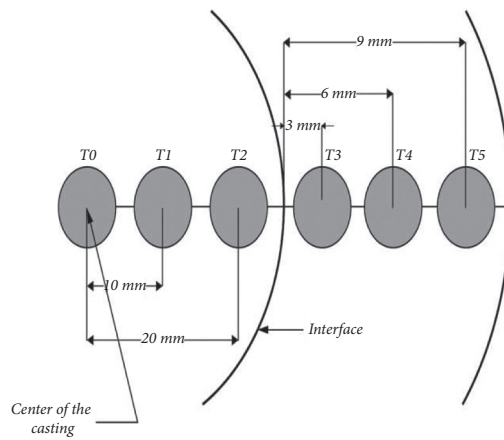
FIGURE 4: (a) Die and baseplate. (b) Appropriate locations of thermocouples for the complete setup. (c) Experimental squeeze cast setup. (d) Exact locations of thermocouples in the baseplate and die material.
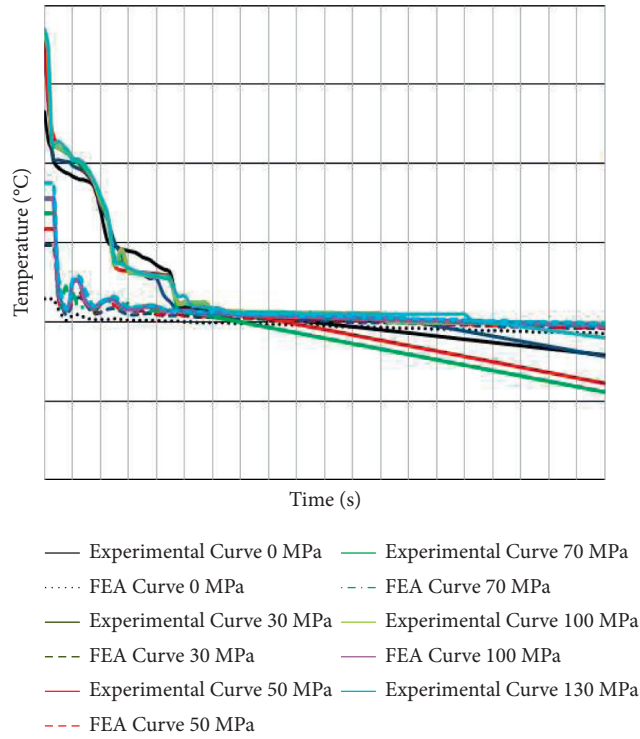
FIGURE 5: Comparison of experimental and FEA curves for Al AA6082/SiC$_p$ composites.
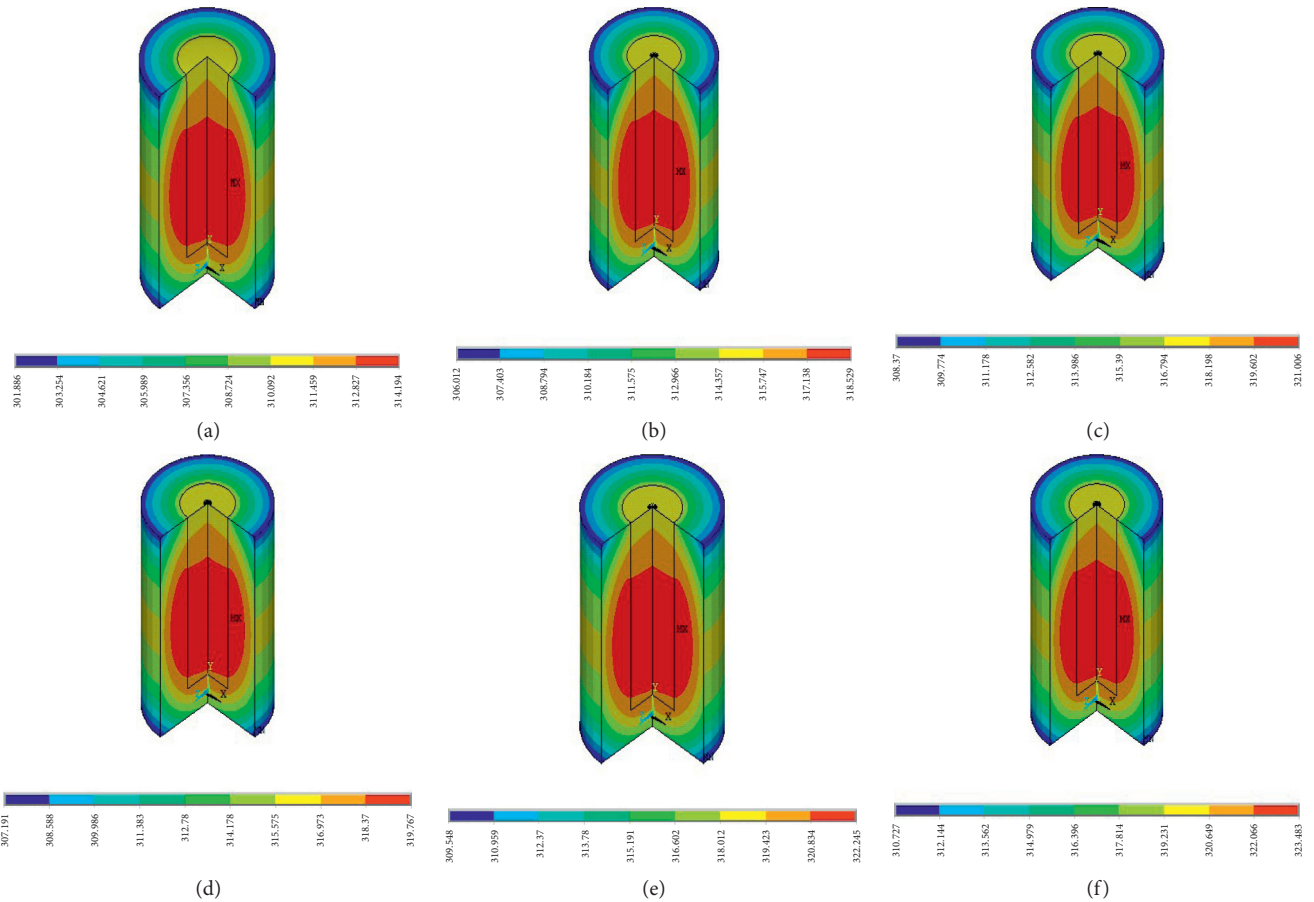
FIGURE 6: Temperature dispersion in the composites at various squeeze pressures up to 800 seconds: (a) 0 MPa; (b) 30 MPa; (c) 50 MPa; (d) 70 MPa; (e) 100 MPa; (f) 130 MPa.
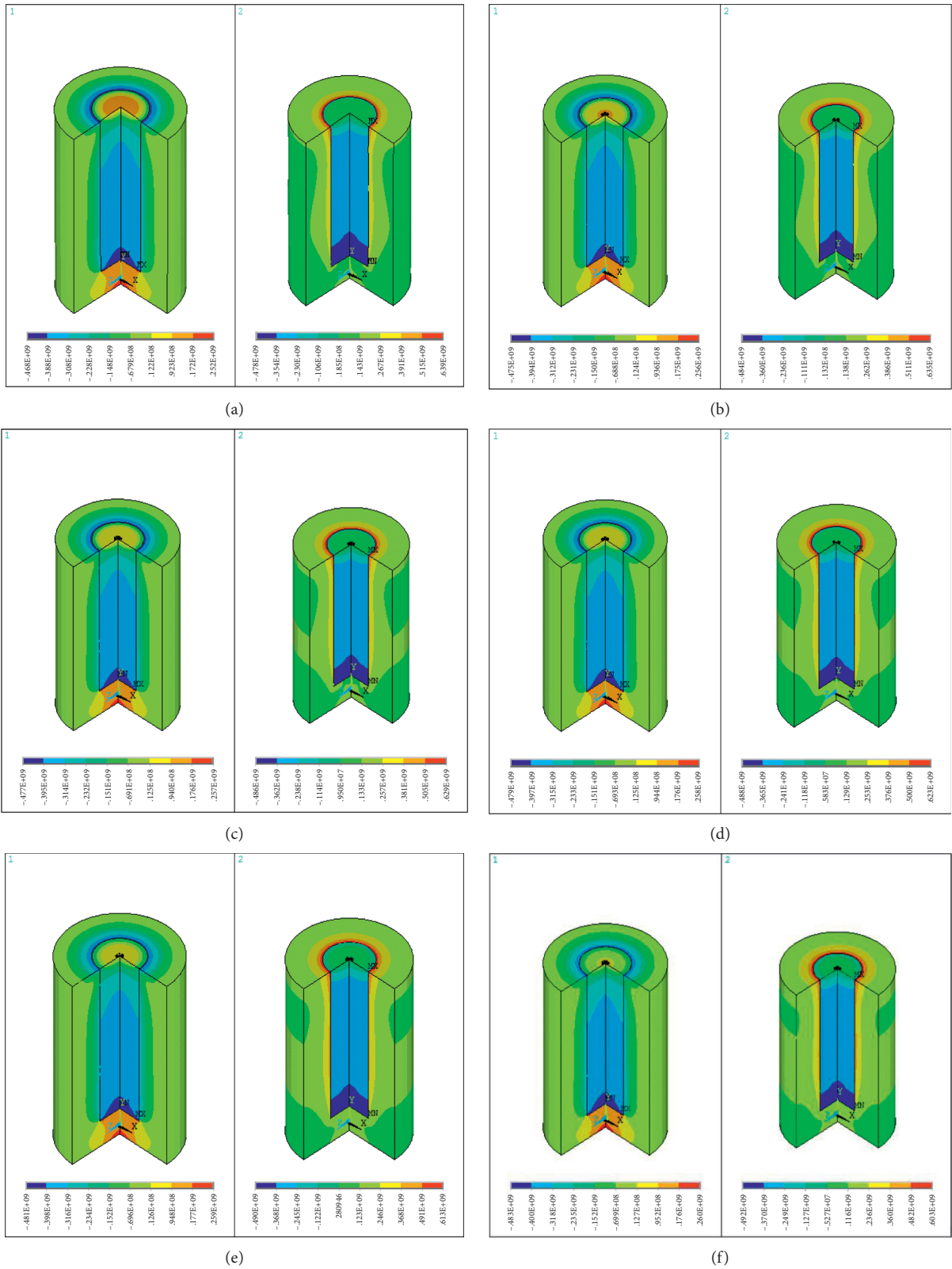
Figure 7: The radial and tangential stresses obtained with increasing squeeze pressures: (a) 0 MPa; (b) 30 MPa; (c) 50 MPa; (d) 70 MPa; (e) 100 MPa; (f) 130 MPa.

TABLE 6: Stress dispersion of the squeeze cast composite for 800 seconds.

Squeeze pressure (MPa)	Radial stress (MPa)		Tangential stress (MPa)	
	Max	Min	Max	Min
0	252	−468	639	−478
30	256	−475	635	−483
50	257	−477	629	−486
70	258	−479	623	−488
100	259	−481	613	−490
130	260	−483	603	−492

system and outside the system. In this analysis, the initial thermal stresses are kept at 0°C, and it was considered that the composites' mechanical property values are taken as per the experimental work because the mechanical property values may change at higher temperature. With these constraints, the temperature (linear) distribution and tangential and radial stresses are plotted for the squeeze-cast specimen. The melt and reinforcements have different thermal expansions; hence, the study of radial and tangential stresses is essential in this analysis. Figure 7 shows the radial and tangential stresses obtained with increasing squeeze pressures. The application of pressure is in the axial direction; hence, the radial stresses are high at the bottom of the die. At the melt and die interface location, the tangential stress is maximum. Table 6 shows the stress dispersion of the squeeze cast composite for 800 seconds. Tangential stresses are comparatively higher than the radial stresses, and in the interfacial region, the tangential stresses are decreased [30]. It is due to the application pressure, which leads to a thermal mismatch within the composite [31]. Hence, the stresses are closely related to the orthotropic behavior of composite material.

5. Conclusion

The following observations are identified from the experimental and FEA analysis of an aluminium-based metal matrix composite.

(1) Experimental cooling rates are increased by increasing the squeeze pressure. The effect of pressure enhances the heat transfer rate of the melt and the die material.

(2) Predicted cooling rates are increased by increasing the pressure, but the values are almost close to experimental cooling rates.

(3) The amount of heat transfer is observed in the melt and reinforcement based on the applied pressure. Hence, the temperature is varied based on the applied pressure.

(4) Tangential stresses are comparatively higher than the radial stresses, and in the interfacial region, the tangential stresses are decreased. It is due to the application pressure, which leads to a thermal mismatch within the composite. Hence, the stresses are closely related to the orthotropic behaviour of composite material.

(5) Particle and base alloy reaction, the formation of air inside the mould, and flow velocity have to be considered for the FEA study.

Data Availability

The data used to support the findings of this study are included within the article.

Disclosure

Conflicts of Interest

The authors declare that there are no conflicts of interest regarding the publication of this article.

Acknowledgments

References

[1] P. Gurusamy, S. B. Prabu, and R. Paskaramoorthy, "Influence of processing temperatures on mechanical properties and microstructure of squeeze cast aluminum alloy composites," *Materials and Manufacturing Processes*, vol. 30, no. 3, pp. 367–373, 2015.

[2] P. Gurusamy, S. B. Prabu, and R. Paskaramoorthy, "Interfacial thermal resistance and the solidification behavior of the Al/SiCpComposites," *Materials and Manufacturing Processes*, vol. 30, no. 3, pp. 381–386, 2015.

[3] P. Gurusamy, S. Balasivanandha Prabu, and R. Paskaramoorthy, "Prediction of Cooling Curves for Squeeze Cast Al/SiCp Composites Using Finite Element Analysis," *Metallurgical and Materials Transactions A*, vol. 46, no. 4, pp. 1697–1703, 2015.

[4] M. R Ghomashchi and A. Vikhrov, "Squeeze casting: an overview," *Journal of Materials Processing Technology*, vol. 101, no. 1-3, pp. 1–9, 2000.

[5] T. M. Yue and G. A. Chadwick, "Squeeze casting of light alloys and their composites," *Journal of Materials Processing Technology*, vol. 58, no. 2-3, pp. 302–307, 1996.

[6] A. Fardi Ilkhchy, M. Jabbari, and P. Davami, "Effect of pressure on heat transfer coefficient at the metal/mold interface of A356 aluminum alloy," *International Communications in Heat and Mass Transfer*, vol. 39, no. 5, pp. 705–712, 2012.

[7] K. Sukumaran, K. K. Ravikumar, S. G. K. Pillai et al., "Studies on squeeze casting of Al 2124 alloy and 2124-10% SiCp metal matrix composite," *Materials Science and Engineering: A*, vol. 490, no. 1-2, pp. 235–241, 2008.

[8] G. S. Hanumanth and G. A. Irons, "Solidification of particle-reinforced metal-matrix composites," *Metallurgical and Materials Transactions B*, vol. 27, no. 4, pp. 663–671, 1996.

[9] T. P. D. Rajan, K. Narayan Prabhu, R. M. Pillai, and B. C. Pai, "Solidification and casting/mould interfacial heat transfer characteristics of aluminum matrix composites," *Composites Science and Technology*, vol. 67, no. 1, pp. 70–78, 2007.

[10] W. Zhou, "Effectively enhanced load transfer by interfacial reactions in multi-walled carbon nanotube rein- forced Al matrix composites," *Acta Materialia*, vol. 125, pp. 369–376, 2016.

[11] W. Zhou, P. Mikulova, Y. Fan, K. Kikuchi, N. Nomura, and A. Kawasaki, "Interfacial reaction induced efficient load transfer in few-layer graphene reinforced Al matrix composites for high-performance conductor," *Composites Part B: Engineering*, vol. 167, pp. 93–99, 2019.

[12] G. Fan, Y. Jiang, Z. Tan et al., "Enhanced interfacial bonding and mechanical properties in CNT/Al composites fabricated by flake powder metallurgy," *Carbon*, vol. 130, pp. 333–339, 2018.

[13] M. Li, Z. Zhang, H. Gao et al., "Formation of multilayer interfaces and the load transfer in graphene nanoplatelets reinforced Al matrix composites," *Materials Characterization*, vol. 159, Article ID 110018, 2019.

[14] T. Han, E. Liu, J. Li, N. Zhao, and C. He, "A bottom-up strategy toward metal nano-particles modified graphene nanoplates for fabricating aluminum matrix composites and interface study," *Journal of Materials Science & Technology*, vol. 46, pp. 21–32, 2020.

[15] Y. Liu, Y. Ma, W. Liu et al., "The mechanical properties and formation mechanism of Al/Mg composite interface prepared by spark plasma sintering under different sintering pressures," *Vacuum*, vol. 176, Article ID 109300, 2020.

[16] M. R. Ghomashchi and K. N. Strafford, "Factors influencing the production of high integrity alu- minium/silicon alloy components by die and squeeze casting processes," *Journal of Materials Processing Technology*, vol. 38, no. 1-2, pp. 303–326, 1993.

[17] I. Alfonso, O. Navarro, J. Vargas et al., "FEA evaluation of the Al4C3 formation effect on the Young's modulus of carbon nanotube reinforced aluminum matrix composites," *Composite Structures*, vol. 127, pp. 420–425, 2015.

[18] G. Li, X. Zhang, Q. Fan et al., "Simulation of damage and failure processes of interpenetrating SiC/Al composites subjected to dynamic compressive loading," *Acta Materialia*, vol. 78, pp. 190–202, 2014.

[19] T. R. Vijayaram, S. Sulaiman, A. M. S. Hamouda, and M. H. M. Ahmad, "Numerical simulation of casting solidi-fication in permanent metallic molds," *Journal of Materials Processing Technology*, vol. 178, no. 1-3, pp. 29–33, 2006.

[20] V. Mohanavel, K. Rajan, and M. Ravichandran, "Synthesis, characterization and properties of stir cast AA6351-aluminium nitride (AlN) composites," *Journal of Materials Research*, vol. 31, no. 24, pp. 3824–3831, 2016.

[21] S. K. Jagadeesh, C. S. Ramesh, J. M. Mallikarjuna, and R. Keshavamurthy, "Prediction of cooling curves during solidification of Al 6061-SiCp based metal matrix composites using finite element analysis," *Journal of Materials Processing Technology*, vol. 210, no. 4, pp. 618–623, 2010.

[22] V. Mohanavel, K. S. Ashraff Ali, S. Prasath, T. Sathish, and M. Ravichandran, "Microstructural and tribological charac-teristics of AA6351/Si3N4 composites manufactured by stir casting," *Journal of Materials Research and Technology*, vol. 9, no. 6, Article ID 14662, 2020.

[23] J. Zhang, Q. Ouyang, Q. Guo et al., "3D Microstructure-based finite element modeling of deformation and fracture of SiCp/ Al composites," *Composites Science and Technology*, vol. 123, pp. 1–9, 2016.

[24] J. Nafar Dastgerdi, B. Anbarlooie, A. Miettinen, H. Hosseini Toudeshky, and H. Remes, "Effects of particle clustering on the plastic deformation and damage initiation of particulate reinforced composite utilizing X-ray CT data and finite element modeling," *Composites Part B: Engineering*, vol. 153, pp. 57–69, 2018.

[25] X. Tan, B. Zhang, K. Liu et al., "Microstructure and me-chanical property of the 2024Al matrix hybrid composite reinforced with recycled SiCp/2024Al composite particles," *Journal of Alloys and Compounds*, vol. 815, Article ID 152330, 2020.

[26] L. J. Yang, "The effect of solidification time in squeeze casting of aluminium and zinc alloys," *Journal of Materials Processing Technology*, vol. 192-193, pp. 114–120, 2007.

[27] Y. Seo and C. Kang, "The effect of applied pressure on particle-dispersion characteristics and mechanical properties in melt-stirring squeeze-cast SiCp/Al composites," *Journal of Mate-rials Processing Technology*, vol. 55, no. 3-4, pp. 370–379, 1995.

[28] A. Maleki, B. Niroumand, and A. Shafyei, "Effects of squeeze casting parameters on density, macrostructure and hardness of LM13 alloy," *Materials Science and Engineering: A*, vol. 428, no. 1-2, pp. 135–140, 2006.

[29] M. S. Yong and A. J. Clegg, "Process optimisation for a squeeze cast magnesium alloy," *Journal of Materials Pro-cessing Technology*, vol. 145, no. 1, pp. 134–141, 2004.

[30] G. Altan and M. Topçu, "Thermo-elastic stress of a metal-matrix composite disc under linearly-increasing temperature loading by analytical and FEM analysis," *Advances in Engi-neering Software*, vol. 41, no. 4, pp. 604–610, 2010.

[31] L. Cen, W. Y. Qin, and Q. M. Yu, "Analysis of interface delamination in thermal barrier coating system with axi-symmetric structure based on corresponding normal and tangential stresses," *Surface and Coatings Technology*, vol. 358, pp. 785–795, 2019.

Research Article

Novel Lanthanum Doped Magnetic Teff Straw Biochar Nanocomposite and Optimization Its Efficacy of Defluoridation of Groundwater Using RSM: A Case Study of Hawassa City, Ethiopia

Temesgen Abeto Amibo [iD],[1] **Surafel Mustafa Beyan** [iD],[1] **and Tsegaye Markos Damite**[2]

[1]*School of Chemical Engineering, Jimma Institute of Technology, Jimma University, P.O. Box 378, Jimma, Ethiopia*
[2]*Department of Material Science & Engineering, Jimma Institute of Technology, Jimma University, P.O. Box 378, Jimma, Ethiopia*

Correspondence should be addressed to Temesgen Abeto Amibo; temesgen.abeto@ju.edu.et

The problem extent of the large concentration of fluoride ions in drinking water is still a central health issue. In the present study, lanthanum doped magnetic Teff straw biochar (LDMTSB) was developed as a novel adsorbent for removing fluoride ions in the groundwater in Rift-Valley regions, especially Hawassa city, Ethiopia. The synthesized LDMTBC was characterized via FTIR, XRD, SEM, and BET. And, this analysis proposed that multiadsorption techniques such as ligand exchange, precipitations, and electrostatic interaction could be evinced throughout the fluoride ions adsorption process by LDMTSB. The constraints that influence the adsorption efficacy, namely, a dosage of LDMTSB, contact time, pH of the solution, and rotational speed, were analyzed and optimized using the response surface methodology approach. Under the optimum situations, LDMTSB dosage: 3.97 g, contact time: 56.36 min, rotational speed: 591.19 rpm, and pH: 3.968 demonstrate high efficacy of LDMTSB with 98.89% fluoride removal capacity. Further, the quadratic model ($R^2 = 0.9841$) was designated for governing the mathematical process. The LDMTSB was successful in the removal of fluoride ions in the groundwater. This study provides a valuable economical solution for the application of Teff straw.

1. Introduction

Drinkable water is not generally available owing to contamination caused by both natural and human sources [1]. The major cause of water contamination was the fast expansion of industry, mining processes, natural gas extraction, and the natural presence of high amounts of minerals.

The ions calcium (Ca), sodium (Na), potassium (K), sulfate (SO_4^{2-}), magnesium (Mg), chloride (Cl), fluoride ion (F), carbonate (CO_3), and bicarbonate (HCO_3) account for more than 90% of the dissolved solids in groundwater [2]. More than 70% of groundwater from deep wells contains F levels higher than the WHO's drinkable limit. F levels in all hot spring water tests were above the WHO drinkable limit, with the highest value of 57.4 mg/L [3]. These all ions are present in drinkable water in a high amount as it affects the

health of human beings, animals, and aquatic organisms [4, 5]. Fluoride concentrations of more than 1.5 g/L are designated contaminants by the WHO because they impair the life of living things. Excessive fluoride consumption causes serious health problems, such as dental fluorosis, which has a concentration range of 1.5 to 4.0 mg/L, skeletal fluorosis, which has a concentration range of 4.0–10.0 mg/L, and gradually debilitating scourge-skeletal fluorosis, which has a concentration greater than 10 mg/L. Fluoride has a safe level when its concentration is less than 1.5 mg/L, which is necessary to avoid tooth decay and anxiety [6, 7]. More than 200 million people are now suffering from high levels of fluoride concentration in their drinking water, which is caused by fluoride being naturally poisoned in the water [8]. The groundwater containing fluoride ions is abundant in the East African Rift Valley basin, particularly in Hawassa,

Zeway, Shashamane, and Adama. The research of acceptable fluoride treatment procedures is required to lower the content of fluoride in drinking water [9].

Within physical methods, several drinking water treatment techniques were developed and implemented to remove such contaminants by high fluoride concentration. Ion exchange, electrokinetic coagulation, membrane separation processes, and adsorption techniques are the widely utilized methods. Each of which has its cons and pros [10]. Electrokinetic coagulation yields poor outcomes from fluoride removal, meaning that it is not that much applicable method. Membranes are unable to resist severe conditions such as high temperature, reactive environments, and contaminated feed. As a result, industrialists do not prefer them as a separation mechanism [10, 11]. In contrast, adsorption is considered as the preferred method of wastewater treatment as it is a method that is easy and suitable to operate and effective in purifying waste water as it has high efficiency of deodorizing, detoxifying, and easy removal of harmful components from wastewater [11]. Adsorption-based methods use microporous materials that are a very promising cost-efficient technology, which is commonly accepted as the most attractive, efficient, and affordable due to its simple control, low operating and capital investment costs, and higher energy efficiency [12, 13]. The adsorption technique was utilized to decrease the fluorine content in the drinking water for this investigation.

Biochar is prepared through thermal degradation of biomass at moderate temperature by pyrolysis process in the absence of oxygen [14]. Biochar is known for being cheap, safe, and it has a plentiful supplier of raw resources that are used for the production of it such as municipal sludge, livestock manure, and agricultural residues [15]. It also has unique physicochemical characteristics, such as a vast number of pore structures, large specific surface area, stability, and effectiveness. As a result, biochar is ideally suited for use as an adsorbent [16]. Biochar can be prepared from different lignocellulosic materials, and Teff straw can be used for the preparation of magnetic biochar.

Teff straw is a plentiful and indigenous lignocellulose material in Ethiopia, and it is a residual waste obtained after the seeds of Teff were removed. According to Mottaleb and Rahut [17], Ethiopia is a significant producer of Teff in the globe, presently producing a considerable amount of Teff annually in various locations, and Teff accounted for roughly 24% of all grain-cultivated land in Ethiopia in 2017. Teff straw was freely available in all regions of Ethiopia once Teff seeds were removed, and Teff straw was considered a waste [18].

According to Huang et al. [19], to increase the adsorption efficiency, Teff straw biochar can be doped with hydrated metal oxides, such as Zr (IV), La (III), Fe (II), Fe (III), and Ce (IV), that were widely investigated for treatment purposes because it could supply a large number of coordination sites and had a particular affinity for fluoride ions. From those, lanthanum has gotten a lot of interest since it is nontoxic, low-cost, chemically stable, and has an exceptionally high affinity for fluoride even at low concentrations [20].

Up to date, no research has been done on the removal of fluorides ion from groundwater using Teff straw biochar magnetic composite doped with lanthanum. Further, process parameters, namely, adsorption dosage, pH, rotational speed, and adsorption time, that affect the efficiency of the composite on the removal of fluorides was optimized using central composite response surface methodology (RSM-CCD) as a statical tool. RSM-based CCD has been proved as a reliable statical tool to estimate and optimize various variables on removal efficiency [21, 22]. Supplementary characterization of the obtained Teff straw biochar magnetic composite doped with lanthanum by X-ray diffraction (XRD), scanning electron microscope (SEM), Fourier transforms infrared (FTIR), and proximate analysis were executed.

2. Materials and Methods

2.1. Materials and Chemicals Used.

The raw material Eragrostis tef (Teff straw) was collected from Yebu, 10 kilometers from Jimma town, Ethiopia, and high fluoride water content was transported from Hawassa city to Jimma Institute of Technology's Department of Material Science and Engineering to treat and characterize the application, as well as to determine the optimal defloration capacity of the adsorbent. For the current study, ferrous chloride ($FeCl_2.4H_2O$), ferric chloride hexahydrate ($FeCl_3 \cdot 6H_2O$), lanthanum chloride ($LaCl_3$), potassium nitrate (KNO_3), hydrochloric acid (HCl), sodium hydroxide (NaOH), sodium chloride (NaCl), ethylenediaminetetraacetic acid (EDTA), and sodium fluoride (NaF) were analytical grade chemicals purchased from Hi-Media Rankem PLC, Addis Ababa, Ethiopia. Distilled water was used throughout this study. The following tools were used to synthesize and characterize the adsorbents: Muffle furnace, sonicator, FTIR (Furrier transmission infrared spectroscope), XRD (X-ray diffraction), TGA (thermogravimetric analysis), BET (Brunauer-Emmett-Teller), and SEM (Scanning Electron Microscope) were employed, as well as UV-spectrophotometer and AAS (atomic absorption spectrophotometer) to test the adsorption of fluoride ions.

2.2. Methods

2.2.1. Biochar Synthesis from Teff Straw (Eragrostis Tef).

Hand-sorting was used to eliminate contaminants such as non-Teff straw, grasses, sand, leaves, and dirt. The Teff straw was then steeped in tap water overnight. The next day, the stocked Teff straw was cleaned three times with distilled water that was produced through the reverse osmosis process. The size of the sun-dried Teff straws was reduced using a knife and other size reduction tools, and the size was analyzed by mesh analysis, and the size between 1 mm and 2 mm was taken, followed by impregnation with diluted (1% v/v) sodium hydroxide to remove the mineral and other impurities from the sample. Then, in the absence of oxygen, it was placed in a muffle furnace at 500°C for 2 hours. After the carbonization process was completed, it was chilled overnight in an L31M muffle furnace. Finally, the Teff straw

biochar was crushed and sieved to achieve a particle size of fewer than 63 μm, which was put on pun and kept in a glass container for later use.

2.2.2. Lanthanum Doped Magnetic Biochar Nanocomposite Adsorbent Preparation.

Teff straw biochar was doped with lanthanum salts to create nanocomposites for adsorption purposes. The chemical coprecipitation technique was utilized to create lanthanum doped magnetic Teff straw biochar [23]. Nanocomposites doped with lanthanum metal salts such as iron salts and lanthanum salts were used to create biochar. Teff straw biochar (8 g) was added to an aqueous solution containing 80 ml of $FeCl_2.4H_2O$ (2.54 g), $FeCl_3 \cdot 6H_2O$ (6.5 g), and $LaCl_3$ (1.96 g), then it was stirred until a homogeneous solution was formed, followed by sonication for further 20 minutes. Following sonication, 1 M sodium hydroxide solution was added to the solution until the pH reached 11 at room temperature. To complete the reaction, the entire mixture was swirled at a rotational speed of 400 rpm at a temperature of 90°C for 1 day, and then it was cooled at room temperature. After cooling, the separation procedure was carried out using Whatman filter paper with a pore size of 42 μm, and the adsorbents were rinsed repeatedly in distilled water until the pH reached seven [24]. Then, the black precipitate was separated through a 42 μm Whatman filter with the help of an external magnet and washed repeatedly with deionized water until the pH decreased to seven. Then, the final precipitate was dried in an oven overnight, followed by calcination in a muffle furnace at 300°C for about two hrs. Finally, the milled lanthanum doped magnetic biochar composite adsorbent was passed through the 1 mm sieve to obtain the constant particle size. To test the adsorption effectiveness of single Teff straw biochar and Teff straw biochar doped with lanthanum, two samples were produced, one without the presence of lanthanum salt and the other with 0.15, 0.2, 0.25, and 0.3 w/w ratios of $LaCl_3$ to biochar. Based on the results of the five trials experiments, magnetic biochar containing lanthanum has better fluoride removal efficiency and was thus chosen for future adsorbent preparation by taking into account previous work on minor changes.

2.3. Characterization of Teff Straw (Eragrostis Tef).

The ASTM (American Society for Testing and Materials) standards were utilized to establish the proximate analysis for moisture content, ash content; volatility contents were examined to estimate the fixed carbon content in Teff straw biomass. The raw Teff straw maintained below 2 mm in thickness weighed 5 grams. The prepared Teff straw was dried in an oven at 1050 degrees Celsius until it formed a uniform mass. The experiment was repeated three times. The ash composition of raw Teff straw ash was determined using a muffle furnace with model number L31M. The 3 g of Teff straw sample was placed in a crucible and burnt at 1000 degrees Celsius until the Teff straw ash was completely transformed to ash. The ash content may be calculated using equation (2). The volatile matter was measured by ASTM (E-872). Then, 2 g of Teff straw samples were burnt in a muffle

furnace with a model number of L31M by using a crucible at 650°C for 6 minutes; hence, it allowed cooling in a desiccator. The volatile matter content was determined by using equation (3). Fixed carbon was determined by subtracting the entire sample content from the sum of the percent moisture, ash, and volatile matter. As a result, the fixed carbon was determined by equation (4)

$$TS_{MC} = \frac{W_B - W_A}{W_B} \times 100\%, \qquad (1)$$

where TS_{MC} is the moisture content of raw Teff straw, W_B represents the weight of the Teff straw in its natural state, and W_A represents the weight of the oven-dried sample.

$$TS_{AC} = \frac{W_{C+BA} - W_C}{W_{C+AA} - W_C} \times 100\%, \qquad (2)$$

where TS_{AC} is the ash content of Teff straw sample, W_C is the weight of the crucible, W_{C+BA} is the weight of the crucible + sample weight before the ash process, and W_{C+AA} is the weight of the crucible + sample after the ash process.

$$TS_{VC} = \frac{TS_{IW} - TS_{FW}}{TS_{IW}} \times 100\%, \qquad (3)$$

where TS_{VC} stands for the volatility content of the Teff straw sample, TS_{IW} stands for the initial weight of the Teff straw sample, and TS_{FW} stands for the final weight of the Teff straw sample.

$$FCC = 100\% - [TS_{MC} + TS_{AC} + TS_{VC}] \times 100\%, \qquad (4)$$

where FCC stands for fixed carbon content, TS_{MC} stands for the moisture content of raw Teff straw, TS_{AC} is the ash content of Teff straw samples, TS_{VC} stands for volatility content of Teff straw sample.

2.4. Characterization of Biochar Produced.

The fixed carbon content is ground to produce biochar from Teff straw raw material [25]. Biochar produced characterized by using different types of equipment such as FTIR, XRD, TGA, SEM, yields of biochar obtained from Teff straw, point zero charges were determined.

2.4.1. FTIR Analysis.

FTIR was used to determine the functional groups found in the raw Teff straw, sample, Teff straw biochar, and lanthanum modified Teff straw biochar comparatively. The bond stretching and vibrations of functional groups were studied using an FTIR analyzer at room temperature with a spectrum 400-IR (Perkin Elmer) in the range 4500–400 cm^{-1} and KBr pellets as a reference. The chemical functional groups were then identified by looking at the wavenumbers associated with signals in the FTIR spectra and comparing them to the standard absorbance of functional groups [26].

2.4.2. X-Ray Diffraction (XRD) Analysis.

According to Yao et al. [27], XRD was used to determine the crystallinity index analyses purpose by using crystallinity peak area and

amorphous peak area for Teff straw biochar as well as modified biochar with lanthanum. The device used to conduct X-ray diffraction was the XRD-7000 apparatus for studies on the produced material powder. The studies were carried out with the angle of diffraction (2θ) kept between 10 and 80 degrees. Using the crystallinity index equation, determine if the material is crystalline, semicrystalline, or amorphous.

$$CI = \frac{A_C}{A_T} \times 100\%, \tag{5}$$

where CI stands the crystallinity index, A_C crystallinity peak area, and A_T the total area obtained from both crystallinity peak area + amorphous peak area.

2.4.3. SEM Analysis.
SEM analysis was performed to examine the changes in the surface morphology of the biochar before and after modification with iron and lanthanum oxide nanoparticles [28].

2.4.4. Thermal Stability Analysis.
The weight loss of the sample was measured using the TGA-4000 Perkin Elmer instrument [29]. This was done with nitrogen gas for all samples. Under the influence of nitrogen gas, the samples were heated from 25°C to 500°C. The nitrogen gas flow rate was 20 ml/min, with a heating rate of 10°C/min. The data from Derivative Thermogravimetric (DTGA) was also taken. This aids in determining the thermal stability of Teff straw biochar as well as the modified biochar.

2.4.5. BET Analysis.
The BET instrument was used to determine the specific surface area of Teff straw biochar, magnetic biochar, and lanthanum doped magnetic biochar. The Brunauer-Emmett-Teller (BET) technique was used to calculate the volume of adsorbed nitrogen gas based on the adsorption and desorption of various gas concentrations at atmospheric pressure and ambient temperature. The three samples were first treated for 1 hour at 230°C to eliminate air and water molecules from the pore. Finally, the samples were tested.

2.4.6. Point Zero Charge Analysis.
Point of zero charges for a concept that a certain substance has a specific pH at which it is neutral. The point of zero charges is the pH value at which the surface is neutral. The solid addition technique was used to study the point of zero charges for biochar and lanthanum doped Teff straw biochar. In eight separate flasks, 500 ml of KNO_3 (0.1 M) with a pH range of 3 to 10 was produced. 45 ml of KNO_3 (0.1 M) was drawn from 500 ml, the pH of the solution was adjusted with drops of 0.1 N NaOH and 0.1 N HCl solutions, and 0.5 g of powdered Teff straw biochar and Modified biochar with lanthanum samples were added to each flask and shaken at room temperature. The final pH of all samples was measured after 2 days and plotted against the pH change; the intersection point of the curve with the line passing through the origin was used as a reference for determining the point of zero charge value.

2.5. Experimental Design.
The response surface approach was analyzed using the design of expert (v.11) software to evaluate the experimental effects. The optimum strategy for optimizing the process variable, namely adsorption dosage, pH, rotational speed, and adsorption time, is the response surface methodology. It was utilized to determine which component had the most impact on adsorption. To answer such problems, the response surface approach central composite design was selected to evaluate linear interaction and quadratic connections between independent and dependent variables during the optimization of fluoride ions removal from the groundwater. The CCD generates 30 data points based on equation (6), comprising 16 factor points, 8 axial points, and 6 center points (Table 1).

To examine the experimental effects, the response surface approach was evaluated using the design of expert (v.11) software. The optimum adsorption efficiency of modified lanthanum doped magnetic Teff straw biochar was calculated using the response surface approach. This study was conducted to discover which components had the most influence on fluoride ion adsorption, allowing researchers to understand which components have the biggest impact on yield.

$$Y = 2^b + 2b + b_c, \tag{6}$$

where Y represents the number of trials done, b represents the number of independent variables, and b_c represents the number of replicates utilized to determine if the above-mentioned experiment was accurate or not.

$$M = a_o + \sum_{i=1}^{n} a_i x_i + \sum_{i=1}^{n} a_{ii} x_i^2 + \sum_{i=1}^{n-1} \sum_{j=i+1}^{n} a_{ij} x_{ij}, \tag{7}$$

where M stands for the predicted response of surface methodology. The number n denotes the number of independent factors utilized to optimize the adsorption capacity. Constant coefficients, first-order (linear) coefficients, second-order (quadratic) interaction coefficients, and second-order (quadratic) noninteraction coefficients are all represented by the coefficients a_o, a_i, a_{ii}, a_{ij}.

3. Results and Discussion

3.1. Proximate Analysis of Raw Teff Straw (Eragrostis Tef).
In this section, the proximate analysis was analyzed to determine the fixed carbon contents of Teff straw by using equation (4). Hence, to investigate the ash content, moisture content, and volatile matter content was mandatory to determine the fixed carbon content in Teff straw. According to the study conducted by Bageru and Srivastava [18], the proximate analysis for Teff straw was reported as moisture content of 6.0 to 8.0%, ash content of 3 to 6%, volatile matter of 70 to 80%; also this study had similar results reported by the previous study. For the current study, the proximate analysis performed was presented in Table 2, the same as that reported in a literature review from another study, the ash content, moisture content, and volatility matter had 4.88%, 6.98%, and 73.61%, respectively. Based on this, the result

TABLE 1: Central composite design matrix for defluoridation efficiency.

Run	Independent variable (factors)				Dependent variable (factor)
	Dosage LDMTSB (g/L)	Contact time (min.)	Rotational speed (rpm)	pH	Defluoridation efficiency (%)
1	4	30	600	3	85.94
2	3	45	500	4.5	95.94
3	4	60	400	6	83.46
4	2	60	400	3	81.77
5	3	45	500	4.5	95.91
6	4	60	400	3	93.03
7	2	30	600	6	73.97
8	4	60	600	6	92.95
9	3	45	500	4.5	90.89
10	3	45	700	4.5	91.98
11	2	30	600	3	73.47
12	3	45	500	7.5	78.15
13	4	60	600	3	97.95
14	3	45	500	4.5	95.90
15	3	75	500	4.5	88.58
16	2	60	600	6	82.50
17	2	30	400	6	71.12
18	4	30	400	6	83.23
19	4	30	600	6	87.34
20	4	30	400	3	90.55
21	1	45	500	4.5	69.75
22	3	15	500	4.5	76.46
23	2	60	400	6	71.67
24	3	45	300	4.5	84.83
25	2	30	400	3	78.88
26	3	45	500	1.5	85.76
27	3	45	500	4.5	95.93
28	3	45	500	4.5	95.95
29	2	60	600	3	83.45
30	5	45	500	4.5	90.46

TABLE 2: Proximate analysis experimental results for Teff straw.

Std.	Analysis conducted	Experimental results	Obtained from literature
(1)	Ash content	4.88%	3 to 6%
(2)	Moisture content	6.98%	6.0 to 8.0%
(3)	Volatile matter content	73.61%	70 to 80%
(4)	Fixed carbon content	14.53%.	12–17%
		Experimental result	Bageru and Srivastava [18]

obtained for fixed carbon content was 14.53%. From the total bases, including ash content, moisture content, and volatile matter, the yield of biochar produced from Teff straw was 12.11 percent, while from fixed carbon, the yield was 83.23 percent. This result was obtained at a temperature of 500°C for 120 minutes.

3.2. Teff Straw Biochar and Magnetic Biochar Modified Lanthanum Physiochemical Properties. When compared to modified biochar containing lanthanum and biochar made from Teff, straw has distinct properties. The bulk densities of Teff straw biochar and lanthanum doped magnetic Teff straw biochar were 0.42 and 0.592 gcm^{-3}, respectively, as indicated in Table 3 for the experimental findings. This indicates that the bulk density of lanthanum doped magnetic Teff straw

biochar was higher than that of Teff straw biochar, owing to the presence of rare Earth metals within it, which increased its density. Similarly, the pH value of Teff straw biochar is higher than that of lanthanum doped biochar. Teff straw biochar was discovered to have a higher hydroxyl group than lanthanum doped Teff straw biochar, which was attributed to the hydroxyl group contained to make it high pH. Point of zero charge value for Teff straw biochar and lanthanum doped Teff straw biochar were 4.3 and 8.1, respectively. Teff straw biochar had a smaller pH surface area for becoming zero than lanthanum doped Teff straw, which was because Teff straw biochar consumes more acid during point zero charge generation. Teff straw biochar had a surface area of 120.61 m^{2}g^{-1}, while lanthanum doped Teff straw biochar had a surface area of 321.52 m^{2}g^{-1}, indicating that lanthanum doped Teff straw biochar has a larger surface area than Teff

TABLE 3: Different biochar physiochemical properties.

Std.	Analysis conducted	Teff straw biochar	Lanthanum doped Teff straw biochar
(1)	Bulk density (gcm^{-3})	0.42	0.592
(2)	pH	10.8	6.3
(3)	pH_{PZC}	4.3	8.1
(4)	Surface area (m^2g^{-1})	120.61	321.52

straw biochar. As a result, modified biochar had greater adsorption effectiveness than nonmodified biochar. Because the modified biochar is a nanocomposite, it has high surface area availability. Teff straw activated carbon ($552.23 \, m^2g^{-1}$) has a higher surface area than coffee husk activated carbon, according to another study ($400 \, m^2g^{-1}$). Tef straw biochar surface area ($120.61 \, m^2g^{-1}$) was higher than coffee husk biochar, as was the case with activated carbon ($90.2 \, m^2g^{-1}$). Research conducted by Kong et al. [30] on the removal of phosphate and fluoride using rice lanthanum doped nanocomposite reported that the surface area of the nanocomposite is $123.28 \, m^2g^{-1}$. The point zero charge for both TSBC and LDMTSB is shown in Figure 1.

3.3. Characterization Teff Straw BC and Lanthanum Doped Magnetic Teff Straw BC

3.3.1. Crystallinity Index for TSBC and LDMTSB. Figures 2(a) and (b) show how X-ray diffraction (XRD) may be used to determine the crystalline, amorphous, and semicrystalline phases. As illustrated in Figure 2 (a), the lanthanum doped magnetic Teff straw biochar exhibited an amorphous phase due to the random distribution of atoms inside the modified Teff straw biochar. In addition to this, lanthanum doped magnetic Teff straw biochar has crystalline peaks, and its crystallinity index was around 43.45 percent. The lanthanum doped magnetic Teff straw biochar after fluoride adsorption had crystal peaks, as illustrated in Figure 2 (b), due to the presence of metals such as lanthanum and irons in biochar. The total crystallinity index after adsorption is 43.81 percent. This indicates the modified biochar after adsorption was found in the amorphous phase. The metal ions and fluoride ions found in water are absorbed by an active site found in a nanocomposite. Due to this reason, the ions are randomly distributed, which makes the modified biochar after adsorption in the amorphous phase. The metals exhibit crystalline peaks as a result of the crystallinity nature of the metals, and the crystalline peak in modified biochar is owing to this [31]. The peak represented by 24.10°, 37.05°, 45.49°, and 50.61° represents lanthanum peaks. Peaks for iron (II) and (II) were also found in X-RD patterns 45.00°, 64.62°, and 69.47°. The peak found around 22.11, 53.73, and 69.47 represents the peaks for fluoride absorbed.

3.3.2. Functional Group Analysis. From Figure 3(a), the Fourier transmission infrared spectrophotometer (FTIR) spectra of TSBC contained a variety of peaks that begin ion adsorption. The number of peaks detected in TSBC shows the presence of several functional groups within it; these peaks' functional groups were determined using wavenumber (cm^{-1}) and transmittance (percent). The graph of the TSBC spectra shows a large peak bond stretch between 3500 and $3000 \, cm^{-1}$, indicating the existence of free and bond hydroxyl (O-H) functional groups bond stretch [32]. The peaks found at 1800 to $1200 \, cm^{-1}$ may be ascribed to a strong carboxyl stretch (C=O) stretched at $1294 \, cm^{-1}$ [33]. C-H and carboxylic acid may be attributed to the peak at 1465 to $1000 \, cm^{-1}$ [34]. Other prominent peaks identified between 1000 and $695 \, cm^{-1}$ reflect significant C-O and C=C [34]. The overall surface of biochar is characterized by the presence of several negatively charged functional groups [35]. Similarly, similar results with other biomass-derived biochars have been published regularly. As seen in Figure 3(b), the LDMTSB clearly shows a decrease in hydroxyl, carboxyl, and carbonate functional groups, with the following alteration when compared to Teff straw biochar. However, minor peaks at 3200, 1846, 1675, 1620, 1500, 1440, 692, 621, 556, and $461 \, cm^{-1}$ were detected, which can be ascribed to the presence of residual O-H, C-O, and C≡N functional groups. Furthermore, novel bond lengths were discovered at 650 to $500 \, cm^{-1}$, which can be ascribed to the existence of the La-O ($621 \, cm^{-1}$) and Fe-O ($556 \, cm^{-1}$) bonds stretch, respectively. In different studies' findings, the metal oxide bond stretches were found within these ranges [36]. The peak is shown in Figure 3(c), LDMTSB, pecks are removed through the adsorption process. The free O-H, C≡ N, C=O, and other free bonds found in modified biochars then adsorb the fluoride ions prevalent in water, causing some bond stretch to be lost [37]. The bond stretch for hydroxyl was found at about $3200 \, cm^{-1}$; OH bond stretch did not exist after the adsorption process. Bond stretch for C=O, C≡N, and C-O accessible about $1635 \, cm^{-1}$, $1410 \, cm^{-1}$, $2951 \, cm^{-1}$, and $2345 \, cm^{-1}$ has not been detected after adsorption, as shown in Figure 3(c), analogous to that of OH. This is owing to the lone pair found in each bond stretch being filled with fluoride ions.

3.3.3. Thermogravimetric Analysis. The breakdown of cellulose, hemicellulose, and lignin, low molecular weight molecules such as carboxylic aldehydes, alkenes, and other components, are all linked to the thermal stability of materials during pyrolysis [1, 38]. High mass losses were detected in three degradation zones on the TGA curve of the biochar sample, as illustrated in Figures 4 (a) and (b). The release of water molecules caused the mass loss at 100°C [39]. Between 68°C and 273°C, there was a significant loss of mass, which might lead to the breakdown of low molecular weight molecules. Decomposition of larger molecular weight compounds resulted in a significant mass loss at 400°C. High mass losses were found at 450°C in the Teff straw biochar
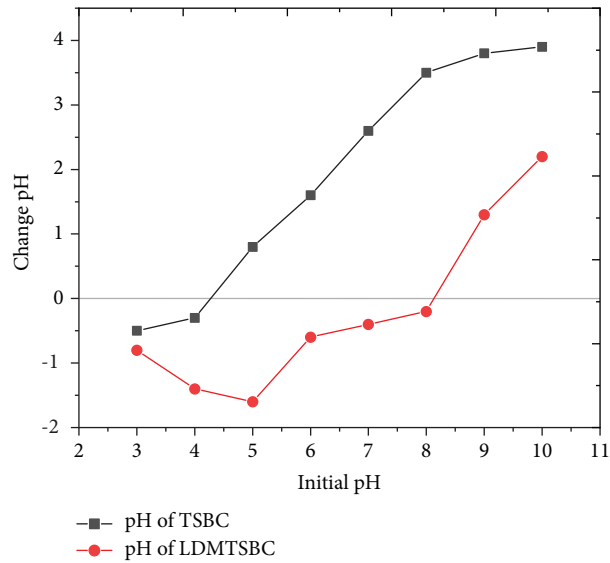
Figure 1: Point zero charge determination for TSBC and LDMTSB.
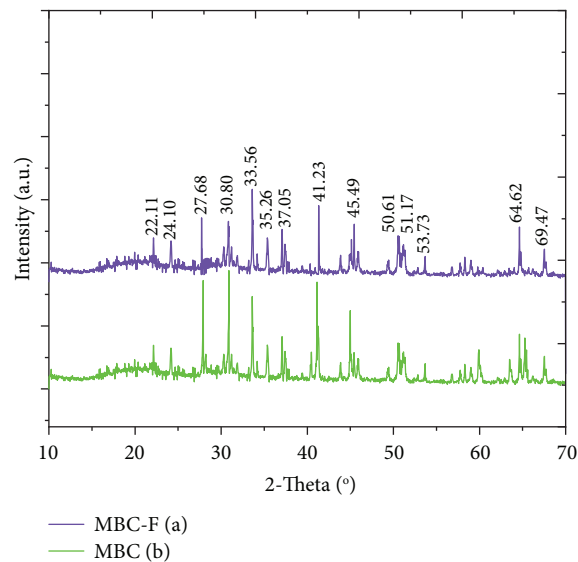
Figure 2: X-ray patterns for lanthanum doped magnetic BC before and after defluoridation.

curve, as shown in Figure 4 (a). According to Figure 4(b), after 273°C, the mass loss is stable due to nanocomposite properties as well as the presence of metals within modified biochar [40]. The reduction of magnetite, hematite, and iron carbide composites into lower oxide groups, as shown in the above chemical process, maybe a concern during decomposition at higher temperatures. The catalytic actions of iron species on the carbon surface are predicted to cause the magnetic composite to decompose rapidly at higher temperatures [41].

3.3.4. Analysis for TSBC and LDMTSB. The SEM pictures in Figures 5(a) and 5(b) clearly show the difference in biochar morphology before and after metal oxide nanoparticle modification. The heterogeneous layer with a high

micromere structure was shown by SEM morphology studies [42]. In contrast, the LDMTSB SEM picture in Figure 5(b) showed a rough and white surface. In addition, while comparing raw Teff straw biochar with lanthanum doped magnetic biochar, many tiny holes were discovered. The actions of metal oxide nanoparticles on the surface of biochar cause this morphological modification [43]. The development of pores on the LDMTSB adsorbent might explain the increase in surface area. Similar morphological structures have been reported in different previous researches [43, 44].

3.4. The Initial and Final Concentration of Fluoride Ion. According to Haji et al.[3], the fluoride ions content in the Rift Valley region was higher than the WHO drinking water
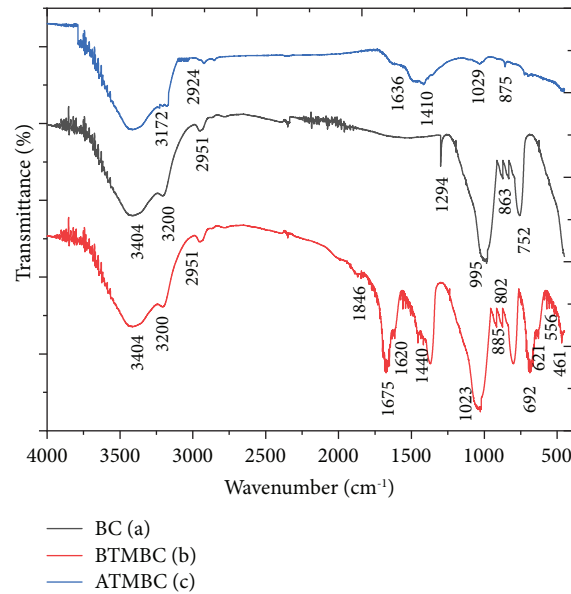
FIGURE 3: FTIR analysis for biochar, modified Teff straw biochar, and modified biochar treatment.
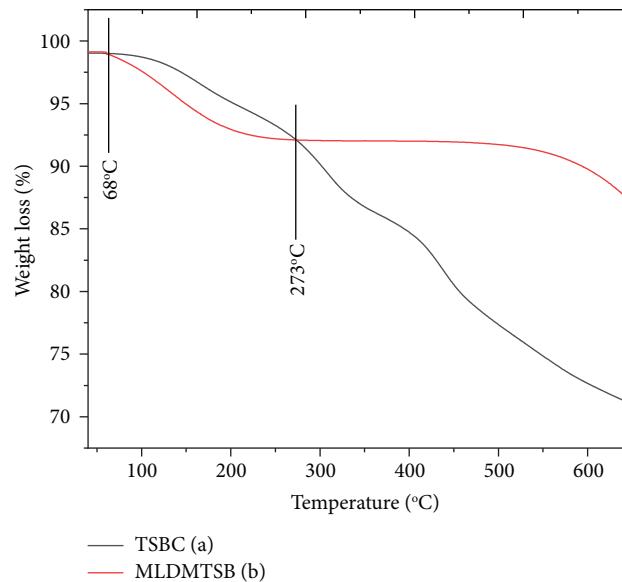
FIGURE 4: Thermogravimetric analysis of Teff straw biochar and lanthanum doped magnetic Teff straw biochar.

recommendation. As a result, treatment was required to lower the concentration of fluoride ions in groundwater and other sources of water with high fluoride content. The groundwater utilized in this study has a fluoride concentration of 56.2 mg/L and was sourced from the Rift Valley, especially Hawassa and Zeway city. The Rift Valley underground water has the following anions and cations, namely magnesium (Mg^{2+}), sodium (Na^+), potassium (K^+), calcium (Ca^{2+}), sulfate (SO_4^{2-}), bicarbonate (HCO_3^-), nitrates (NO_3^-) silica (SiO_2), chlorine (Cl^-), and fluoride (F^-) [3]. The blank solution was prepared from magnesium (Mg^{2+}), sodium (Na^+), potassium (K^+), calcium (Ca^{2+}), sulfate (SO_4^{2-}),

bicarbonate (HCO_3^-), nitrates (NO_3^-) silica (SiO_2), and chlorine (Cl^-) ions based on their concentration in groundwater. The stock fluoride concentration absorbance experiment was to create a standard curve. The absorbance of fluoride ions was measured using AAS. The concentration versus absorbance standard curve for fluoride ions was prepared, and this helps to determine the final concentration of fluoride ions after treatment. AAS was used to assess the absorbance capacity of the centrifuged solution. The standard curve was used to calculate the residual concentration of fluoride ions [45]. Equation (4) was used to compute the % elimination of fluoride ions.

(a)

(b)
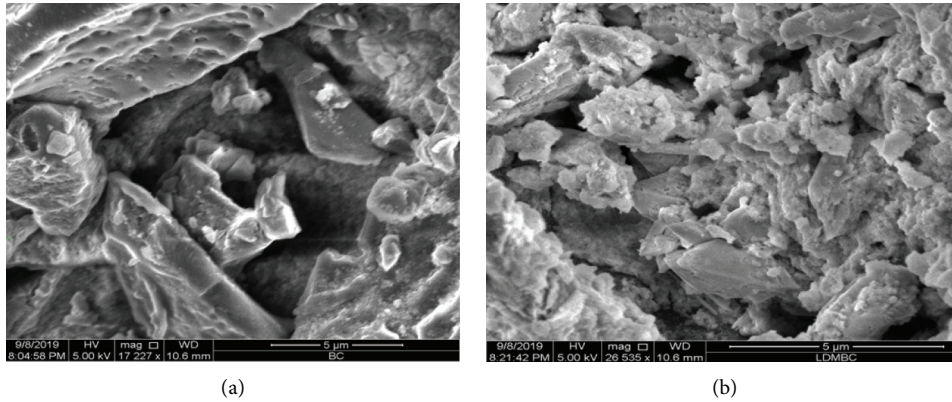
FIGURE 5: (a) SEM analysis of biochar and (b) lanthanum doped magnetic Teff straw biochar.

$$R\,(\%) = \frac{C_o - C_t}{C_o}, \tag{8}$$

where R (%) denotes the proportion of removal percent, the starting concentration of fluoride ions is denoted by C_o, while the concentration of methyl orange after adsorption is denoted by C_t.

3.5. Defluoridation Process and Response Surface Methodology Analysis.

The response surface approach for the central composite design matrix is given in Table 1. The number of variables is four, and the total number of experiments is thirty, according to equation (6). The factorial design, the axial run, and the central run are the three primary elements of this experiment. The factorial design is made up of 16 experiments represented by 2^4, the axial run is made up of 8 experiments represented by 2×4, and the center run is made up of 6 experiments. The four independent variables are Dosage LDMTSB (g/L), Contact Time (min.), Rotational Speed (rpm), and pH; they were investigated to calculate the defluoridation effectiveness based on the laboratory experiment presented in Table 1. The coded variables A, B, C, and D stood for LDMTSB dosage (g/L), Contact Time (min.), Rotational Speed (rpm), and pH, respectively.

The data in Table 4 were evaluated using analysis of variance (ANOVA) with a significance threshold of 5% (α-value = 5%). In addition, the F-value and p value for models are provided in Table 4. The p value aids in determining the significance and nonsignificant of each factor, as well as the interaction component, which was adequately represented [46]. Dosage LDMTSB (A), contact time (B), rotational speed (C), and pH (D) were all significantly affecting the adsorption efficiency; thus, p values were less than 0.0001. BC, CD, BD, A^2, C^2, B^2, and D^2 have a substantial influence on adsorption efficiency as well as other interaction effects such as AB, AD, and AC because it has a p value that is higher than the α-value. The Model F-value of 66.19 indicates that the model is statistically significant. The F-value having a magnitude of 0.01 percent has a probability of occurring due to noise. According to Mustefa Beyan et al. [47], the sum of squares and F-value provide information about whether factors have a substantial negative or positive

impact on the response. The sum of squares and F-value are presented in Table 4. Single variables of dose, contact time, rotating speed, and pH had sums of square values of 805.51, 184.37, 60.67, and 121.59, respectively. Dosage, contact duration, rotating speed, and pH, all had F-values of 363.80, 83.27, 27.40, and 54.92, respectively. The model's sum of squares and F-value were 2051.75 and 66.19, respectively. According to this data, the dose has a substantial impact on defluoridation capability, followed by dosage, contact time, pH, and rotating speed. Aside from that, this experiment's lack-of-fit model is 0.9565. This means that the error terms do not influence the adsorption efficiency. The p value was smaller than the level of significance (α -value). Thus, the models were approved [48].

Standard deviation, mean, CV (%), R^2, adjusted R^2, projected R^2, and adequacy precision were analyzed by ANOVA are shown in Table 5 to fit statistical data. 1.49, 85.59, 1.74, 0.9841, 0.9692, 0.9520, and 26.7531 were the values for standard deviation, mean, C.V. (%), R^2, adjusted R^2, projected R^2, and adequate precision, respectively. According to Abeto Amibo [46], the adjusted and predicted R^2 are in good agreement below a 20% variation. The adjusted square of R (R^2) value was 0.9692. This indicates that it is reasonably close to the predicted square of R (R^2) value of 0.9520. Hence, the difference is less than 0.2. The signal-to-noise ratio is measured by adequacy precision [49]. It is preferable to have a ratio of more than four. The ratio for this model was 26.753 showing that the signal is adequate. The design space may be navigated using this paradigm. The proposed model for this study was quadratic; the coefficient of variation (CV) and standard deviation (SD) values were low and acceptable, with good agreements [50, 51]. The R^2 is approaching one, and the experimental and predicted values are well aligned. The outcomes for this analysis were close to 1, indicating that the data fit well and were highly acceptable.

In Table 6, the coefficients for every single factor and interaction effects are shown. The coefficients for Dosage LDMTSB (A), contact time (B), rotational speed (C), and pH (D) were 5.79, 2.77, 1.59, and -2.25. From their values, dosage LDMTSB (A), contact time (B), and rotational speed (C) had a positive relation with adsorption efficiency, but pH had a negative relation with the adsorption of fluoride ions.

TABLE 4: Analysis of variance (ANOVA) results.

Source	Sum of square	Df	Mean square	F-value	p value	
Model	2051.75	14	146.55	66.19	<0.0001	Significant
A: dosage LDMTSB	805.51	1	805.51	363.80	<0.0001	
B: contact time	184.37	1	184.37	83.27	<0.0001	
C: rotational speed	60.67	1	60.67	27.40	0.0001	
D: pH	121.59	1	121.59	54.92	<0.0001	
AB	0.1640	1	0.1640	0.0741	0.7892	
AC	0.9801	1	0.9801	0.4427	0.5159	
AD	0.2970	1	0.2970	0.1342	0.7193	
BC	56.18	1	56.18	25.37	0.0001	
BD	9.67	1	9.67	4.37	0.0500	
CD	58.91	1	58.91	26.60	0.0001	
A^2	386.19	1	386.19	174.42	<0.0001	
B^2	271.91	1	271.91	122.81	<0.0001	
C^2	77.17	1	77.17	34.85	<0.0001	
D^2	296.85	1	296.85	134.07	<0.0001	
Residual	33.21	15	2.21			
Lack of fit	12.08	10	1.21	0.2857	0.9565	Not significant
Pure error	21.14	5	4.23			
Cor total	2084.96	29				

The adsorption efficiency rises proportionately when the three variables, namely, dose, LDMTSB, contact duration, and rotating speed, increase. The relationship is reversed for pH. As the weight of the dose increases, more pores or adsorption sites become available, resulting in a more efficient and effective adsorption process. It is very obvious that increasing LDMTSB dosage would stream more available active sites for fluoride ions [52]. The adsorption process increased proportionately as the contact time increased because the fluoride ions had enough time to attach to the functional groups contained within the adsorbents [50]. Because the spinning magnetic stirrer avoids the sedimentation of adsorbents during the adsorption process, the rotational speed increases during the adsorption process in tandem with time and dose. The attraction of intermolecular interactions between molecules is referred to as Van der Waals forces [53]. According to Beyan et al. [54], the pH increase, and the adsorption process decrease, the pH decrease, and the adsorption capacity increase due to Van der Waals force present due to hydrogen bonds when the pH is lower, and acidic medium. When all other factors are maintained constant, the coefficient estimate indicates the predicted change in response per unit change in factor value. In an orthogonal design, the intercept is the overall average response of all the runs [55]. The coefficients are changed depending on the factor settings around that average. When the factors are orthogonal, the VIFs are 1; when the factors are not orthogonal, the VIFs are larger than 1, indicating multicolinearity; the higher the VIF, the more severe the factor correlation. VIFs of fewer than ten are considered acceptable [56]. Table 6 shows that parameters such as LDMTSB dose (A), contact duration (B), rotating speed (C), and interaction effects like BC and CD all had a beneficial impact on defluoridation efficiency. Defluoridation efficiency was harmed by factors such as pH and interaction effects such as BD, D^2, C^2, B^2, and A^2. Based on Table 6, the model equation was developed to represent the defluoridation effectiveness by using coded variables in the following equation:

$$DF(\%) = 95.09 + 5.79A + 2.77B + 1.59C - 2.25D + 1.87Bc - 0.7775BD + 1.92CD - 3.75A^2 - 3.15B^2 - 1.68C^2 - 3.29D^2.$$

(9)

3.6. The Response's Actual vs. Predicted values. Figure 6 illustrates the actual and predicted values of defluoridation capacity, which were calculated by combining each independent variable. Figure 6 depicts the actual and predicted adsorption efficiency values. In this graph, the real and anticipated values are closely aligned, with an R^2 value of 0.9841. The difference between the real experimental values and the predicted fit value is represented by this R^2 value.

3.7. The 3D Diagram of Defluoridation Efficiency. A 3D representation of the adsorption of fluoride ions is shown in Figures 7(a) to 7(f). The adsorption results obtained in the 3D representation ranged from 69.75% to 97.95%. The maximum adsorption achieved was 97.95 percent in the 3D representation of Figures 7(a) to 7(f). The maximum yield was obtained at a dosage of 4 g, contact time of 60, a rotational speed of 600, and pH of 3. The difference

TABLE 5: Values for statistics of the fitting.

Values for statistics of fitting	
Std. dev.	1.49
Mean	85.59
CV %	1.74
R^2	0.9841
Adjusted R^2	0.9692
Predicted R^2	0.9520
Adeq precision	26.7531

TABLE 6: Coefficients of the coded variable.

Factor	Coefficient estimate	D1f	Standard error	95% CI low	95% CI high	VIF
Intercept	95.09	1	0.6075	93.79	96.38	
A-dosage LDMTSB	5.79	1	0.3037	5.15	6.44	1.0000
B-contact time	2.77	1	0.3037	2.12	3.42	1.0000
C-rotational speed	1.59	1	0.3037	0.9426	2.24	1.0000
D-pH	−2.25	1	0.3037	−2.90	−1.60	1.0000
AB	−0.1013	1	0.3720	−0.8941	0.6916	1.0000
AC	0.2475	1	0.3720	−0.5454	1.04	1.0000
AD	−0.1362	1	0.3720	−0.9291	0.6566	1.0000
BC	1.87	1	0.3720	1.08	2.67	1.0000
BD	−0.7775	1	0.3720	−1.57	0.0154	1.0000
CD	1.92	1	0.3720	1.13	2.71	1.0000
A^2	−3.75	1	0.2841	−4.36	−3.15	1.05
B^2	−3.15	1	0.2841	−3.75	−2.54	1.05
C^2	−1.68	1	0.2841	−2.28	−1.07	1.05
D^2	−3.29	1	0.2841	−3.90	−2.68	1.05
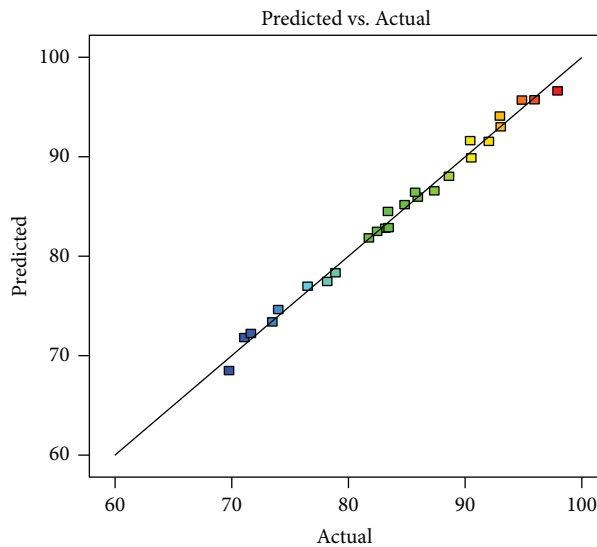
FIGURE 6: Actual versus predicted values for defluoridation efficiency.

between the shapes of the graph in Figures 7(a) and 7(f) was the changing and constant variables during the experiments.

3.8. Optimization of the Defluoridation Process. From Table 7, the optimized results for the defluoridation capacity of the adsorbent were analyzed. For optimization purposes, all independent variables were set in a range its importance was assigned by number 3, and the dependent variable was set at a maximum point that represented the importance of number 5 [46, 47]. The optimum results were 98.89%, and these results were obtained at a dosage of 3.97 g, contact time of 56.36 min, a rotational speed of 591.19 rpm, and pH of 3.968. To cross check these results, the experiment was done three times to testify the maximum adsorption of fluoride

(a)

(b)

(c)

(d)

(e)

(f)
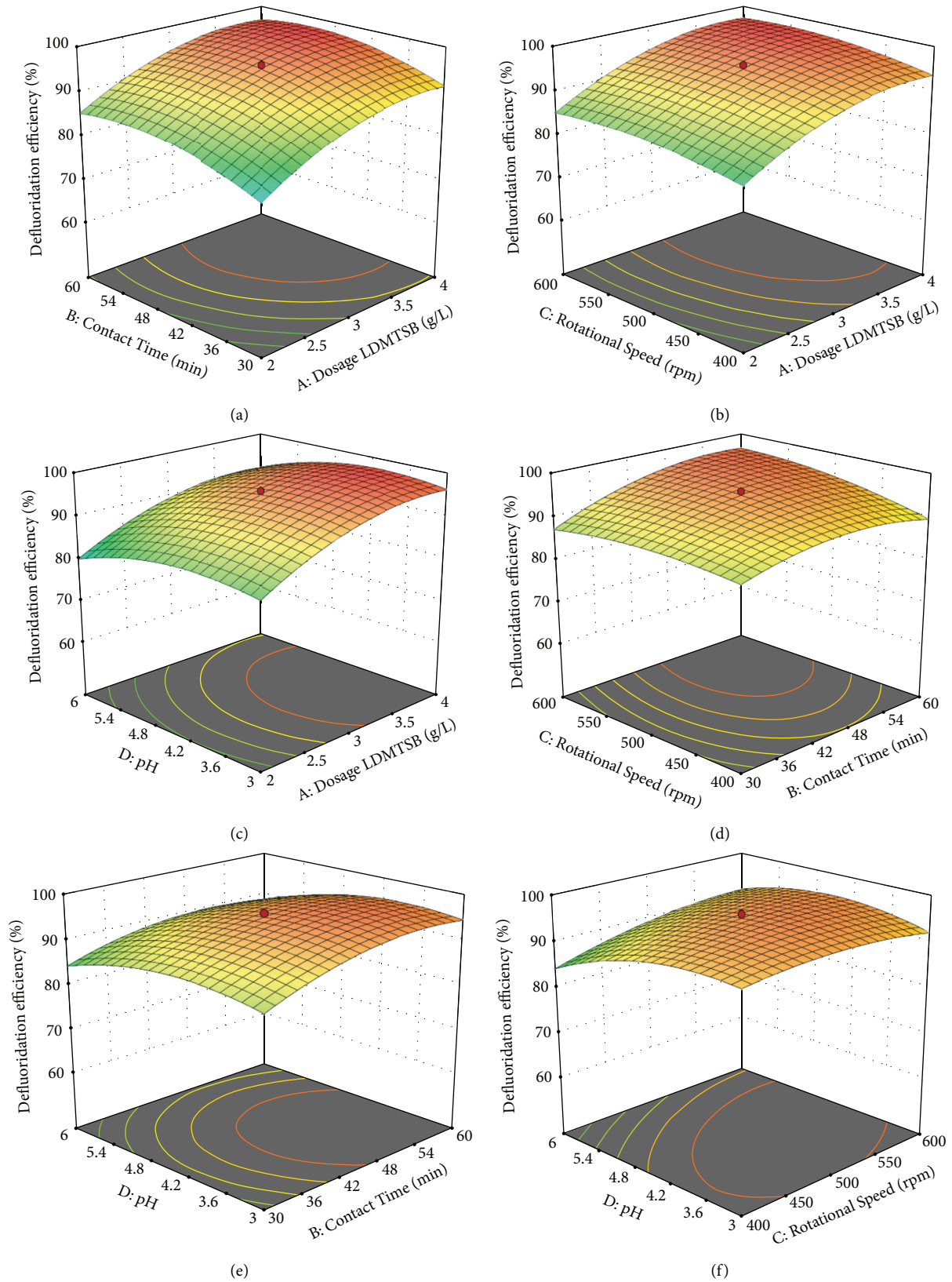
Figure 7: The 3D representation of defluoridation efficiency (%) by varying (a) contact time and dosage, (b) rpm and dosage, (c) pH and dosage, (d) rpm and time, (e) pH and contact time, (f) pH and rpm.

TABLE 7: Optimized results for the defluoridation process.

Name	Goal	Lower limit	Upper limit	Optimized results	Importance
A: dosage LDMTSB	is in range	2	4	3.567	3
B: contact time	is in range	30	60	56.36	3
C: rotational speed	is in range	400	600	591.19	3
D: pH	is in range	3	6	3.968	3
Defluoridation efficiency	Maximize	69.75	97.95	98.885	5
Desirability	Maximize	0	1	1	

ions from the solution. The experiments were conducted at a dosage of 3.97 g, contact time of 56.40 min, a rotational speed of 591.00 rpm, and pH of 3.97. In this case, the adsorption efficiency for fluoride ions was 98.85%. This result had almost the same results as the optimized results obtained from numerical optimization, but only the deviation was less than 0.04%. The desirability for this analysis was 1, and it is a good and highly acceptable model.

4. Conclusions

An efficient and novel LDMTSB adsorbent was synthesized and applied for the removal of fluoride ions in groundwater of Rift Valley located in Hawassa, Ethiopia. In this research, the following information was obtained, (I) Teff straw has 14.53% of fixed carbon, and this makes it an important candidate for biochar preparation. (II) At a dose: 3.57 g, adsorption time: 56.40 min, a rotating speed: 591.00 rpm, and a pH: 3.97, the optimal defluoridation (98.89%) was obtained, and its desirability was 1, (III) LDMTSB had hydroxyl, carbon-carbon double bond, and carbon-nitrogen triple bond, and these functional groups facilitate adsorption of fluoride ions, (IV) in comparison with TSBC and LDMTSB nanocomposite, the later exhibits great thermal stability at high temperatures and has a better ability for removing fluoride ions from water and (V) the surface areas of TSB and LDMTSB were 120.61 and 321.52 m^2/g, respectively.

Data Availability

The data used to support the findings of this study are included in the article.

Conflicts of Interest

The authors declare that they have no conflicts of interest.

References

[1] B. Toussaint, B. Raffael, A. Angers-Loustau et al., "Review of micro- and nanoplastic contamination in the food chain," *Food Additives & Contaminants: Part A*, vol. 36, no. 5, pp. 639–673, 2019.

[2] K. H. Vardhan, P. S. Kumar, and R. C. Panda, "A review on heavy metal pollution, toxicity and remedial measures: current trends and future perspectives," *Journal of Molecular Liquids*, vol. 290, Article ID 111197, 2019.

[3] M. Haji, D. Wang, L. Li, D. Qin, and Y. Guo, "Geochemical evolution of fluoride and implication for F– enrichment in groundwater: example from the bilate river basin of southern main Ethiopian rift," *Water*, vol. 10, no. 12, 2018.

[4] G. Singh, B. Kumari, G. Sinam, Kriti, N. Kumar, and S. Mallick, "Fluoride distribution and contamination in the water, soil and plants continuum and its remedial technologies, an Indian perspective- a review," *Environmental Pollution*, vol. 239, pp. 95–108, 2018.

[5] I. Mukherjee and U. K. Singh, "Groundwater fluoride contamination, probable release, and containment mechanisms: a review on Indian context," *Environmental Geochemistry and Health*, vol. 40, no. 6, pp. 2259–2301, 2018.

[6] A. Maleki and H. Jari, "Evaluation of drinking water quality and non-carcinogenic and carcinogenic risk assessment of heavy metals in rural areas of Kurdistan, Iran," *Environmental Technology & Innovation*, vol. 23, Article ID 101668, 2021.

[7] O. Akoto, J. A. Teku, and D. Gasinu, "Chemical characteristics and health hazards of heavy metals in shallow groundwater: case study Anloga community, Volta Region, Ghana," *Applied Water Science*, vol. 9, no. 2, p. 36, 2019.

[8] M. Vithanage and P. Bhattacharya, "Fluoride in the environment: sources, distribution and defluoridation," *Environmental Chemistry Letters*, vol. 13, no. 2, pp. 131–147, 2015.

[9] A. W. Wagutu, R. Machunda, and Y. A. C. Jande, "Crustacean derived calcium phosphate systems: application in defluoridation of drinking water in East African rift valley," *Journal of Hazardous Materials*, vol. 347, pp. 95–105, 2018.

[10] H. D. Beyene, N. G. Habtu, and A. Ayalew, "Removal of methylene blue dye from textile wastewater using activated carbon prepared from rice husk," *International Journal of Innovation Science and Research*, vol. 9, no. 2, pp. 317–325, 2014.

[11] M. H. Mahmoudian, M. Fazlzadeh, M. H. Niari, A. Azari, and E. C. Lima, "A novel silica supported chitosan/glutaraldehyde as an efficient sorbent in solid phase extraction coupling with HPLC for the determination of Penicillin G from water and wastewater samples," *Arabian Journal of Chemistry*, vol. 13, no. 9, pp. 7147–7159, 2020.

[12] Y. Rashtbari, S. Hazrati, A. Azari, S. Afshin, M. Fazlzadeh, and M. Vosoughi, "A novel, eco-friendly and green synthesis of PPAC-ZnO and PPAC-nZVI nanocomposite using pomegranate peel: cephalexin adsorption experiments, mechanisms, isotherms and kinetics," *Advanced Powder Technology*, vol. 31, no. 4, pp. 1612–1623, 2020.

[13] A. Azari, R. Nabizadeh, A. H. Mahvi, and S. Nasseri, "Integrated Fuzzy AHP-TOPSIS for selecting the best color removal process using carbon-based adsorbent materials: multi-criteria decision making vs. systematic review approaches and modeling of textile wastewater treatment in real conditions," *International Journal of Environmental Analytical Chemistry*, pp. 1–16, 2020.

[14] S. Bolognesi, G. Bernardi, A. Callegari, D. Dondi, and A. G. Capodaglio, "Biochar production from sewage sludge and microalgae mixtures: properties, sustainability and

possible role in circular economy," *Biomass Conversion and Biorefinery*, vol. 11, no. 2, pp. 289–299, 2021.

[15] T. F. Rittl, K. Butterbach-Bahl, C. M. Basile et al., "Greenhouse gas emissions from soil amended with agricultural residue biochars: effects of feedstock type, production temperature and soil moisture," *Biomass and Bioenergy*, vol. 117, pp. 1–9, 2018.

[16] M. Fazeli Sangani, S. Abrishamkesh, and G. Owens, "Physicochemical characteristics of biochars can be beneficially manipulated using post-pyrolyzed particle size modification," *Bioresource Technology*, vol. 306, Article ID 123157, 2020.

[17] K. A. Mottaleb and D. B. Rahut, "Household production and consumption patterns ofTeffin Ethiopia," *Agribusiness*, vol. 34, no. 3, pp. 668–684, 2018.

[18] A. B. Bageru and V. C. Srivastava, "Biosilica preparation from abundantly available African biomass teff (Eragrostis tef) straw ash by sol-gel method and its characterization," *Biomass Conversion and Biorefinery*, vol. 8, no. 4, pp. 971–978, 2018.

[19] D. Huang, Q. Zhang, C. Zhang et al., "Mn doped magnetic biochar as persulfate activator for the degradation of tetracycline," *Chemical Engineering Journal*, vol. 391, Article ID 123532, 2020.

[20] Y. Wu, D. Li, J. Lu et al., "LaMnO3-La2CuO4 two-phase synergistic system with broad active window in NOx efficient reduction," *Molecular Catalysis*, vol. 493, Article ID 111111, 2020.

[21] A. Azari, R. Nabizadeh, A. H. Mahvi, and S. Nasseri, "Magnetic multi-walled carbon nanotubes-loaded alginate for treatment of industrial dye manufacturing effluent: adsorption modelling and process optimisation by central composite face-central design," *International Journal of Environmental Analytical Chemistry*, pp. 1–21, 2021.

[22] A. Azari, M. Yeganeh, M. Gholami, and M. Salari, "The superior adsorption capacity of 2,4-Dinitrophenol under ultrasound-assisted magnetic adsorption system: modeling and process optimization by central composite design," *Journal of Hazardous Materials*, vol. 418, Article ID 126348, 2021.

[23] R. Deng, D. Huang, J. Wan et al., "Chloro-phosphate impregnated biochar prepared by co-precipitation for the lead, cadmium and copper synergic scavenging from aqueous solution," *Bioresource Technology*, vol. 293, Article ID 122102, 2019.

[24] S. H. Dhawane, S. Chowdhury, and G. Halder, "Lipase immobilised carbonaceous catalyst assisted enzymatic transesterification of Mesua ferrea oil," *Energy Conversion and Management*, vol. 184, pp. 671–680, 2019.

[25] C. Tongcumpou, P. Usapein, and N. Tuntiwiwattanapun, "Complete utilization of wet spent coffee grounds waste as a novel feedstock for antioxidant, biodiesel, and bio-char production," *Industrial Crops and Products*, vol. 138, Article ID 111484, 2019.

[26] J. J. Ojeda and M. Dittrich, "Fourier transform infrared spectroscopy for molecular analysis of microbial cells," *Microbial Systems Biology*, vol. 881, pp. 187–211, 2012.

[27] W. Yao, Y. Weng, and J. M. Catchmark, "Improved cellulose X-ray diffraction analysis using Fourier series modeling," *Cellulose*, vol. 27, no. 10, pp. 5563–5579, 2020.

[28] P. Karthikeyan, S. Vigneshwaran, and S. Meenakshi, "Removal of phosphate and nitrate ions from water by amine crosslinked magnetic banana bract activated carbon and its physicochemical performance," *Environmental Nanotechnology, Monitoring & Management*, vol. 13, Article ID 100294, 2020.

[29] M. Khraisheh, K. M. Zadeh, A. I. Alkhouzaam et al., "Characterization of polysulfone/diisopropylamine 1-alkyl-3-methylimidazolium ionic liquid membranes: high pressure gas separation applications," *Greenhouse Gases: Science and Technology*, vol. 10, no. 4, pp. 795–808, 2020.

[30] L. Kong, Y. Tian, Z. Pang et al., "Synchronous phosphate and fluoride removal from water by 3D rice-like lanthanum-doped La@MgAl nanocomposites," *Chemical Engineering Journal*, vol. 371, pp. 893–902, 2019.

[31] W. S. Saeed, A.-B. Al-Odayni, A. Ali Alghamdi, A. Abdulaziz Al-Owais, A. Semlali, and T. Aouak, "Miscibility of poly(-ethylene-co-vinylalcohol)/poly(δ-valerolactone) blend and tissue engineering scaffold fabrication using naphthalene as porogen," *Polymer-Plastics Technology and Materials*, vol. 58, no. 2, pp. 1–23, 2019.

[32] M. I. Ejimofor, I. G. Ezemagu, and M. C. Menkiti, "Physiochemical, Instrumental and thermal characterization of the post coagulation sludge from paint industrial wastewater treatment," *South African Journal of Chemical Engineering*, vol. 37, pp. 150–160, 2021.

[33] J. Liu, Q.-h. Zhang, F. Ma, S.-f. Zhang, Q. Zhou, and A.-m. Huang, "Three-step identification of infrared spectra of similar tree species to Pterocarpus santalinus covered with beeswax," *Journal of Molecular Structure*, vol. 1218, Article ID 128484, 2020.

[34] S. G. Prasad, A. De, and U. De, "Structural and optical investigations of radiation damage in transparent PET polymer films," *International Journal of Spectroscopy*, vol. 2011, Article ID 810936, 2011.

[35] S. Dawood, T. K. Sen, and C. Phan, "Synthesis and characterization of slow pyrolysis pine cone bio-char in the removal of organic and inorganic pollutants from aqueous solution by adsorption: kinetic, equilibrium, mechanism and thermodynamic," *Bioresource Technology*, vol. 246, pp. 76–81, 2017.

[36] S. J. Gerber and E. Erasmus, "Electronic effects of metal hexacyanoferrates: an XPS and FTIR study," *Materials Chemistry and Physics*, vol. 203, pp. 73–81, 2018.

[37] T. Chi, J. Zuo, and F. Liu, "Performance and mechanism for cadmium and lead adsorption from water and soil by corn straw biochar," *Frontiers of Environmental Science & Engineering*, vol. 11, no. 2, p. 15, 2017.

[38] H. Durak, S. Genel, and M. Tunç, "Pyrolysis of black cumin seed: significance of catalyst and temperature product yields and chromatographic characterization," *Journal of Liquid Chromatography & Related Technologies*, vol. 42, no. 11-12, pp. 331–350, 2019.

[39] Y. Li, C. Jia, X. Zhang et al., "Synthesis and performance of bio-based epoxy coated urea as controlled release fertilizer," *Progress in Organic Coatings*, vol. 119, pp. 50–56, 2018.

[40] M. T. H. Siddiqui, H. Ahmed Baloch, S. Nizamuddin et al., "Synthesis of novel magnetic carbon nanocomposite from waste biomass: a comparative study of industrially adoptable hydro/solvothermal co-precipitation route," *Journal of Environmental Chemical Engineering*, vol. 8, no. 2, Article ID 103519, 2020.

[41] M.-H. Li, K.-Y. A. Lin, M.-T. Yang, B. X. Thanh, and D. C. W. Tsang, "Prussian Blue Analogue-derived co/fe bimetallic nanoparticles immobilized on S/N-doped carbon sheet as a magnetic heterogeneous catalyst for activating peroxymonosulfate in water," *Chemosphere*, vol. 244, Article ID 125444, 2020.

[42] B. Armynah, D. Tahir, M. Tandilayuk, Z. Djafar, and W. H. Piarah, "Potentials of biochars derived from bamboo leaf biomass as energy sources: effect of

temperature and time of heating," *International Journal of Biomaterials*, vol. 2019, 9 pages, 2019.

[43] B. Janković, N. Manić, and V. Dodevski, "Pyrolysis kinetics of poplar fluff bio-char produced at high carbonization temperature: a mechanistic study and isothermal life-time prediction," *Fuel*, vol. 296, Article ID 120637, 2021.

[44] J. Zhou, F. Ma, and H. Guo, "Adsorption behavior of tetracycline from aqueous solution on ferroferric oxide nanoparticles assisted powdered activated carbon," *Chemical Engineering Journal*, vol. 384, Article ID 123290, 2020.

[45] C. A. Canciam and N. C. Pereira, "Assessment of the use of epicarp and mesocarp of green coconut for removal of fluoride ions in aqueous solution," *International Journal of Chemical Engineering*, vol. 2019, 8 pages, 2019.

[46] T. Abeto Amibo, "Modeling and pulping variables optimization OF ethanol-alkali pulping and delignification OF grevillea robusta IN Ethiopia BY response surface methodology," *European Journal of Materials Science and Engineering*, vol. 6, no. 1, pp. 34–51, 2021.

[47] S. Mustefa Beyan, S. Venkatesa Prabhu, T. K. Mumecha, and M. T. Gemeda, "Production of alkaline proteases using Aspergillus sp. isolated from injera: RSM-GA based process optimization and enzyme kinetics aspect," *Current Microbiology*, vol. 78, no. 5, pp. 1823–1834, 2021.

[48] T. A. Amibo and A. B. Bayu, "Calcium carbonate synthesis , optimization and characterization from egg," *International Journal of Modern Science and Technology*, vol. 5, 2020.

[49] T. K. Mumecha, B. Surafel Mustefa, S. Venkatesa Prabhu, and F. T. Zewde, "Alkaline protease production using eggshells and membrane-based substrates: process modeling, optimization, and evaluation of detergent potency," *Engineering and Applied Science Research*, vol. 48, no. 2, pp. 171–180, 2021.

[50] Y. Asrat, A. T. Adugna, M. Kamaraj, and S. M. Beyan, "Adsorption phenomenon of arundinaria alpina stem-based activated carbon for the removal of lead from aqueous solution," *Journal of Chemistry*, vol. 2021, pp. 1–9, Article ID 5554353, 2021.

[51] P. S. Venkatesa, G. Girma, A. K. Gizachew, M. Surafel, M. Beyan, and G. Ramesh, "Biosolubilization of Cr (VI) from tannery sludge: process modeling, optimization, rate kinetics and thermodynamics aspects," *International Journal of Recent Technology and Engineering*, vol. 8, no. 4, pp. 4808–4816, 2019.

[52] J. Wang, N. Chen, M. Li, and C. Feng, "Efficient removal of fluoride using polypyrrole-modified biochar derived from slow pyrolysis of pomelo peel: sorption capacity and mechanism," *Journal of Polymers and the Environment*, vol. 26, no. 4, pp. 1559–1572, 2018.

[53] W. Kidus Tekleab, S. M. Beyan, S. Balakrishnan, and H. Admassu, "Chicken feathers based Keratin extraction process data analysis using response surface-box-Behnken design method and characterization of keratin product," *Current Applied Science and Technology*, vol. 20, no. 2, pp. 163–177, 2020.

[54] S. M. Beyan, S. V. Prabhu, T. T. Sissay, and A. A. Getahun, "Sugarcane bagasse based activated carbon preparation and its adsorption efficacy on removal of BOD and COD from textile effluents: RSM based modeling, optimization and kinetic aspects," *Bioresource Technology Reports*, vol. 14, Article ID 100664, 2021.

[55] D. A. A. Abreham Bekele Bayu, "Conversion of degradable municipal solid waste into fuel briquette: case of Jimma city municipal solid waste," *Iranian Journal of Energy and Environment*, vol. 11, no. 2, 2020.

[56] K. Umanath, K. Palanikumar, V. Sankaradass, and K. Uma, "Optimization of wear properties on AA7075/Sic/Mos2 hybrid metal matrix composite by response surface methodology," *Materials Today: Proceedings*, vol. 46, pp. 4019–4024, 2021.

Research Article

Interface Bonding Properties between Nonwater Reaction Polyurethane Polymer Materials and Concrete

Xijun Zhang [ID],[1,2,3] **Chaojie Wang** [ID],[1,2,3] **Han Tian,**[4] **and Mingsheng Shi** [ID][1,2,3,5]

[1]*School of Water Conservancy Engineering, Zhengzhou University, Zhengzhou 450001, China*
[2]*National Local Joint Engineering Laboratory of Major Infrastructure Testing and Rehabilitation Technology, Zhengzhou 450001, China*
[3]*Collaborative Innovation Center of Water Conservancy and Transportation Infrastructure Safety, Henan, Zhengzhou 450001, China*
[4]*Guiyang Engineering Corporation Limited of Power China, Guizhou, Guiyang 550000, China*
[5]*Southern Institute of Infrastructure Testing and Rehabilitation Technology, Guangdong, Huizhou 516000, China*

Correspondence should be addressed to Chaojie Wang; wangyichaojie123@163.com

The concentric pushing method was used to study the bonding properties between polymer and concrete. This paper studied the influence of polymer density, environmental temperature, and moisture content of concrete between polymer and concrete on the bond strength. The results indicated that the bond failure of specimens occurred mainly when the polymer was pushed out. Furthermore, increasing the polymer density increases the bond strength at the polymer-concrete interface but decreases as the moisture content of the concrete increases. The environmental temperature affects the curing time, and the bond strength increases with increasing temperature. Under the same condition, the bond strength was influenced by the roughness of the interface. This study provides references for the construction design and enhances polymer materials and matrix application for repairing cracks in concrete dams.

1. Introduction

Hydraulic structures are prone to cracks and concentrated leak channels during construction or operation. Many dam damage cases are caused by crack penetration. When repairing cracks in concrete dams, surface sealing, insertion, and grouting methods are generally used [1]. The grouting method is the best method to solve such problems. The grout used can be divided into cement grouting and chemical grouting [2–4]. The cement grouting method relies on the pumping pressure of the grouting equipment to fill the crack and act as the plugging slurry. However, the cement material has a long setting time, which is unsuitable for emergency or engineering rescue. After solidification, the cement slurry converts to a brittle material, resulting in repeated cracking [5–7]. The chemical grouting method relies on the pressure of the equipment to pump the slurry to the cracks and fill the

cracks through expansion force [8]. Epoxy resin and polyurethane are generally used in polymer chemical grouting materials [9, 10]. Epoxy resin materials are similar to cement materials. After hardening, they are brittle and cannot withstand secondary cracking [11, 12]. In contrast, the elasticity of the polyurethane slurry in a specific density range is superior to the elasticity of the dam body and has a good sealing effect [13].

With the increasing number of large dams and reservoirs, the commonly used methods of emptying reservoirs are too expensive for deep diseases. Underwater repair is a more feasible method. However, the underwater environment requires a higher standard for repairing materials. Cracks in the dam body in a deep water environment can be repaired using submersibles. This means that the performance of repairing materials faces the adverse conditions of low temperature and wet interface [14–16]. Many

researchers have conducted several studies on this topic [17, 18]. Li et al. developed a polyurethane elastic sealing material and studied its characteristics such as water resistance, chemical resistance, and freeze-thaw resistance. The results showed that the material had high tensile bond strength (over 0.55 MPa) after a long-term water immersion test and a high elastic recovery rate [11, 19]. Sun et al. developed underwater crack grouting materials and used simulation models to conduct detailed experiments on their technology. As a result, they suggested a set of underwater crack repair alternatives and techniques [20]. Zou et al. studied the effects of various ambient temperatures, moisture content, and mixing time on the bonding properties of polyurethane sealing materials. The results showed that the bonding performance increases with extended mixing time. Ambient temperature and moisture content are negatively related to bond strength [21]. The interaction between the polymer and civil engineering structures dramatically influences the mechanical properties of the structure. The strength of the polymer-structure interface is one of the most important parameters in engineering design. However, the most common bond strength testing methods for cement concrete materials are the pull-out and push-in methods [22–24]. Two-component nonaqueous reactive polyurethane materials are widely used for dam antiseepage repair due to their excellent properties [25], but their bonding with concrete has not been thoroughly studied [26]. The functional performance of a two-component polyurethane material after caulking depends on the interfacial moisture content, ambient temperature, and polymer density. In this paper, the bonding performance of two-component polyurethane material and concrete was studied by moisture content, the ambient temperature of the interface, and polymer density. It is crucial to improve the underwater construction technology of polyurethane grouting materials [27, 28].

2. Experiment

2.1. Materials and Model Design.

The polymer was a two-component polymer that reacted and foamed. Component A consisted of isocyanates and polyisocyanates, and component B consisted of polyols and additives. Materials A and B were mixed and injected into steel models by a grouting gun. For polymer materials with densities of 0.1, 0.12, 0.2, 0.29, 0.4, 0.6, 0.8, 0.83, and 1.2 g/cm^3, the polymer density was controlled by mass. The C60 concrete was used in the test. The test pieces of this experiment were based on a standard permeability test piece (upper bottom, 185 mm, lower bottom, 175 mm, and height, 150 mm) [29]. The center was preset with a hollow cylinder with a diameter of 90 mm filled with polymer (as shown in Figure 1(a)).

The polymer generates high temperatures and large expansion forces during the reaction [30]. Therefore, the specimens were placed in a special steel cylinder, and the top and bottom were connected using a flange plate and fixed with bolts. As shown in Figure 1(b), the position of the grouting hole was located at the center of the flange, and the venting hole was located at a short distance from the side of the grouting hole.

2.2. Specimen.

In this test, 120 specimens were created to examine the bond strength between the polymer and concrete, mainly considering three parameters: concrete interface temperature, moisture content, and polymer density (as shown in Table 1). Hollow cylindrical specimens were used for the test. As shown in Figure 2, the concrete adopted a standard impermeability test model (upper, 185 mm, lower, 175 mm, and height, 150 mm). First, the center was cut, and a PVC pipe with a diameter of 90 mm was inserted to reserve a hole for the polymer. The prepared concrete was then poured and removed from the mold, and, 28 days after standard curing, the specimens were soaked in groups. The time control was divided into 0 h, 3 h, 10 h, and 24 h. The soaked specimens were wrapped in plastic wrap and placed in a constant temperature test room (0°C–15°C) for 24 h. After applying butter, they were placed in a steel cylinder. They were then covered with upper and lower flanges, bolts were tightened, and the grouting density was changed by controlling the grouting mass. As a result, the polymer expanded rapidly within the model, discharging air through the overflow hole. After grouting for 1 hour, all samples were unmolded and placed in the laboratory until testing.

After prolonged immersion, cracks in the concrete may be fully saturated. In this experiment, specimens were made using C60 grade high-strength concrete. The moisture content was measured as shown in Figure 3. From the figure, it can be seen that the moisture content of the specimens increased sharply in the early stage after soaking in water, but the growth rate was slow after 24 h. Therefore, the moisture content corresponding to the immersion time of 24 hours can be regarded as the saturated moisture content (about 2.66%).

2.3. Experiment Method.

Due to the short hole in the center of specimens, it was difficult to anchor the low-density specimens. The main test was the bonding properties of the interface between polyurethane polymer and concrete. Therefore, the concentric pull-out test was not adopted, and the bond strength was determined by the concentric pushing test shown in Figure 4 [31]. The specimens were placed on a test bench with a special steel ring substrate. The top of the pusher was made of an 85 mm diameter disc, the center of which was aligned with the sample. The universal testing machine was equipped with a strain acquisition system that collected continuous displacement. The maximum load of the universal test machine was 100 kN, the load speed was 0.1 kN/s, and changes in load and displacement could be recorded automatically. Before official loading, we considered a preload of 1 kN [32]. Loading was stopped when the following happened: (1) the central hole of the concrete specimen was destroyed; (2) the polyurethane polymer core was cracked and damaged; and (3) the polyurethane polymer core did not slip along the concrete interface. Since the maximum load P was measured using a load cell with an accuracy of 0.01 kN, the average bond stress T can be taken as into account $T = P/A$. The average bond strengths of the three groups of parallel specimens were taken as measurement values for those experimental specimens.

FIGURE 1: (a) Test piece schematic. (b) Steel cylinder.

TABLE 1: The parameters related to specimens.

Number	Density $\rho/(g/cm^3)$	Soaking time (h)	Temperature (˚C)	Average moisture content (%)
1–3	0.6	0	0	—
4–6	0.6	0	5	—
7–9	0.6	0	10	—
10–12	0.6	0	15	—
13–15	0.6	3	0	0.98
16–18	0.6	3	5	0.98
19–21	0.6	3	10	1.01
22–24	0.6	3	15	1.02
25–27	0.6	10	0	0.83
. . .	. . .	. . .	. . .	. . .
37–39	0.6	24	0	1.3
40–42	0.6	24	5	1.22
43–45	0.6	24	10	1.03
46–48	0.6	24	15	0.76
49–51	0.12	24	5	1.12
52–54	0.29	24	5	1.57
55–57	0.6	24	5	1.22
58–60	0.83	24	5	1.5
61–63	0.1	0	0	—
64–66	0.2	0	0	—
67–69	0.4	0	0	—
70–72	0.8	0	0	—
73–75	1.2	0	0	—
76–78	1.2	0	5	—
79–81	1.2	0	10	—
82–84	1.2	0	15	—
85–87	0.1	0	25	—
88–90	0.2	0	25	—
91–93	0.4	0	25	—
94–96	0.6	0	25	—
97–99	0.8	0	25	—
100–102	1.2	0	25	—
. . .	. . .	. . .	. . .	. . .
112–114	1.2	24	0	1.92
115–117	1.2	24	5	2.18
118–120	1.2	24	15	2.42

To ensure the accuracy of the experiments, each test piece in the table consists of three samples.

The specimens were classified into three groups to examine the effects of polymer density, prewetting of the concrete surface before grouting, and temperature after grouting on bond behavior. The impact of interfacial moisture on bond strength under dry and saturated conditions was evaluated in the first group. The temperature was 10˚C, and the polymer density was 0.6 g/cm³. In the second group, specimens with temperatures of 0˚C, 5˚C, 10˚C, and 15˚C were tested to examine the effects of temperature. In the third group, samples with various polymer
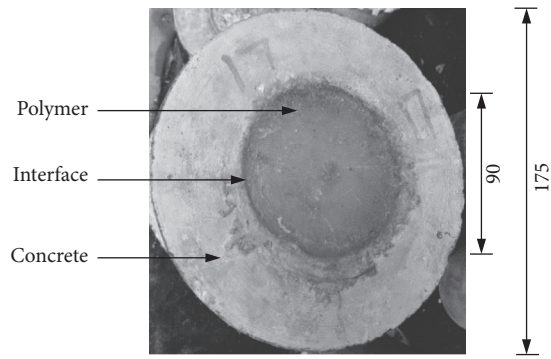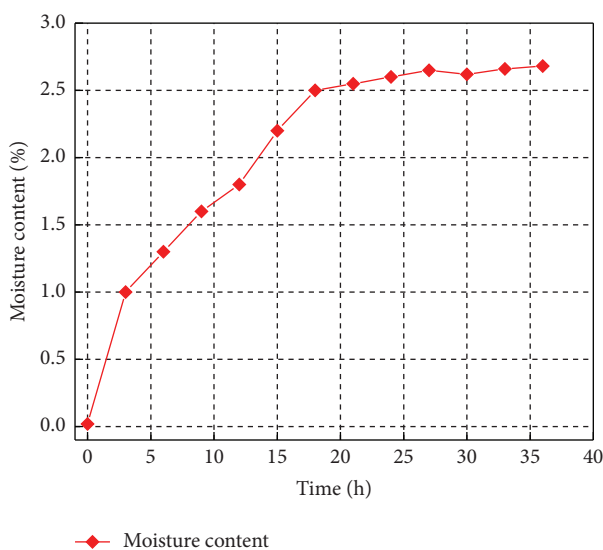
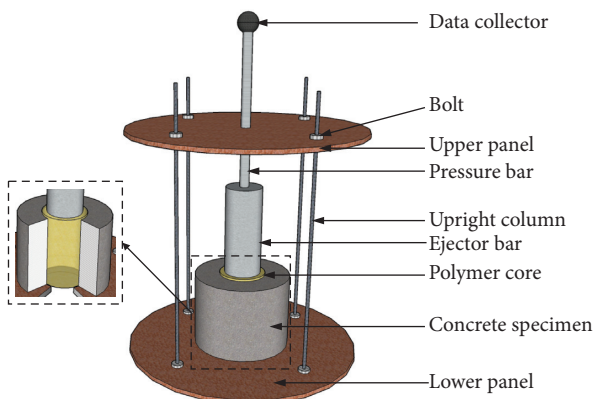FIGURE 2: Details of bonding specimens (mm).

FIGURE 3: Moisture growth curve.

FIGURE 4: Experimental device.

densities of 0.1, 0.12, 0.2, 0.29, 0.4, 0.6, 0.8, 0.83, and 1.2 g/cm^3 were prepared to evaluate the effects of polymer densities.

3. Results and Discussion

Most of the 120 specimens in this test experienced slip damage at the polymer-concrete interface (as shown in Figure 5(a)). In addition, when a part of the annular concrete of the specimen was pushed out, it was partially damaged (as shown in Figure 5(b)). Some high-density specimens are damaged by the hardened surface of polyurethane, but this damage did not penetrate the polymer, and the polymer core was intact. It was found that the interface of the polymer was worn, and the uneven part of the surface was polished. The inner interface of the concrete was also worn, the concrete at the inner interface of the individual specimens was sheared, and the concrete skin was stuck off.

3.1. Average Compression. As shown in Figure 6, the compression value at the time of failure of the polymer bond in the center of specimens was recorded to determine the relationship between the compression value and the density. The results show that the greater the push-out forces for low-density specimens, the greater the compression deformation. The reason is that when the polymer density is low, many bubbles exist in the polymer, the compactness is low, and the compression deformation is large. The deformation of low-density specimens is greatly affected by the push-out force. The push-out force is proportional to the compression value for high-density specimens (1.2 g/cm^3). As a result, the slope of the density-compression curve is less than the slope of low-density specimens. In high-density polymers, the microscopic morphology can be interpreted as the formation of isolated high-density bubbles within the polymer. By decreasing the size of the bubbles, the wall thickness of the bubbles increases. In addition, the delicate and uniform cell structure enhances the resistance of the material to deformation (as shown in Figure 7(b)).

3.2. Polymer-Concrete Bond-Slip Characteristics. As shown in Figure 8, the slip of the load end and that of the free end are basically the same, but the free end displacement is slightly delayed. The free end load-displacement curve intersects the coordinate axis. This indicates that the load end slightly slips in the early stages of loading, and no failure is transmitted from the bond interface to the free end. Thus, there is no slip on the free end, and external loads are resisted mainly by chemical cementation at this stage. According to bond-slip characteristics, the entire development can be simply divided into three stages.
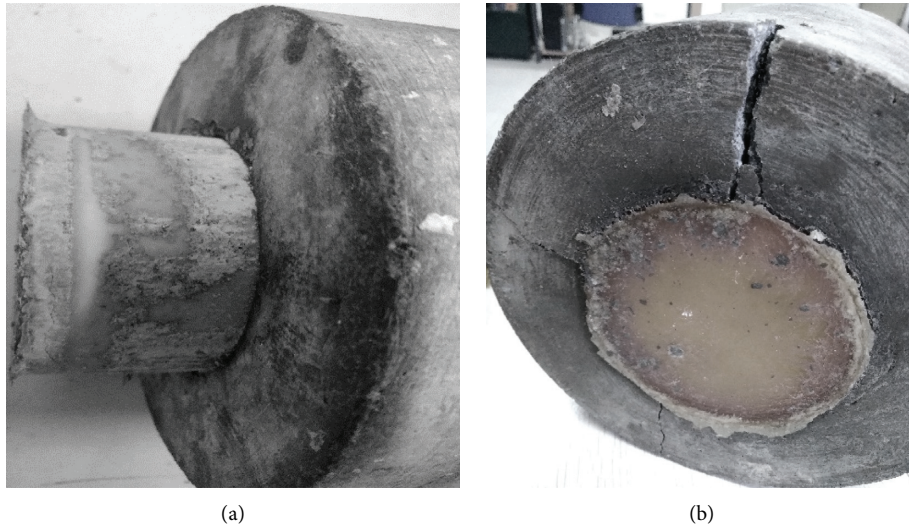
(a) (b)

FIGURE 5: (a) A typical form of destruction. (b) Concrete fragmentation.
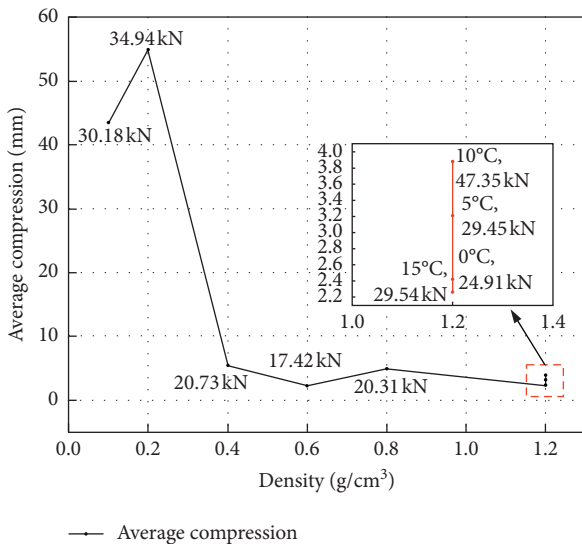

FIGURE 6: Relationship between density and average compression.

3.2.1. Linear Slip Stage (OA). In the OA stage, the load-displacement curve is approximately linear. The thrust is mainly resisted by friction and mechanical bite force at this stage, and the chemical bonding force no longer works. As a result, the displacement increases faster, and the displacement of the free end is slightly smaller than that of the load end.

3.2.2. Ejection Stage. As the load continues to increase, the concrete on the bonding interface is worn out, the amount of slip is further accelerated, the load-displacement curve tends to be flat, and the load eventually reaches its peak.

3.2.3. Thrust Decay Stage. As the amount of slip increases, the concrete surface that comes into contact with the polymer wears severely, reducing the friction and mechanical bite force and the corresponding thrust.

3.3. Bond Strength. This test uses the bond strength between polymer and concrete under normal temperature (25°C) and dry conditions as a reference. Table 2 shows the trend of bond strength as a function of density.

3.3.1. Effect of Moisture Content. Cracks at certain engineering sites in dams are often moist because the water level constantly changes on rainy days and under the influence of open sluice gates [20]. Polyurethane materials are sensitive to the moisture level at the repair interface, which in turn affects the bond strength between the polyurethane polymer and the concrete on either side of the crack [33]. Specimens in Table 3 have the same density ($0.6 \, g/cm^3$) and interface temperature (0°C). Four different wetting conditions were set, and soaking time was used as a screening condition for moisture levels. Using the moisture content as a quantitative index, the bond strength was measured as follows. It can be seen that the bond strength decreases with the increase of moisture levels (water content) under the same temperature condition, because the water reacted with isocyanate to form carbon dioxide to reduce the adhesion if the isocyanate in the two-component polyurethane material was less than 2% in the aqueous state. The reason may be that when the amount of isocyanate is small, the foam curing is not complete, and the structure of the cross-linking network is partly defective. At a temperature of 0°C and a polymer density of $0.6 \, g/cm^3$, the bond strength of the specimens at the soaking times of 3 h and 24 h decreased by 75.2% and 84.3%, respectively. Therefore, it is highly required to reduce the interfacial moisture between concrete and polymers in engineering applications. For example, a superplasticizer can be added to concrete to prevent a significant decrease in bond strength due to moisture [34].

3.3.2. Effect of Temperature. Figure 9 shows that, under the same conditions, the higher the temperature within a certain temperature range, the higher the bond strength. However,
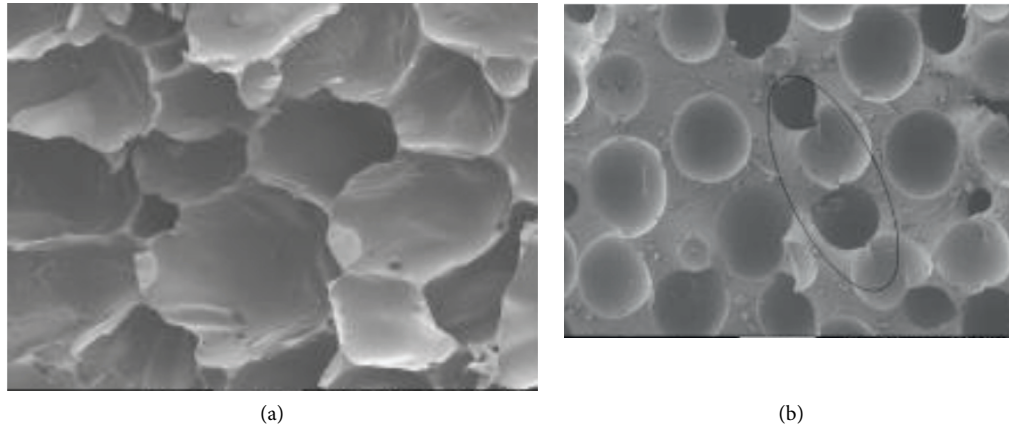
(a)   (b)

FIGURE 7: SEM images of the polymer at densities of (a) $0.15\,\text{g/cm}^3$ and (b) $0.57\,\text{g/cm}^3$.
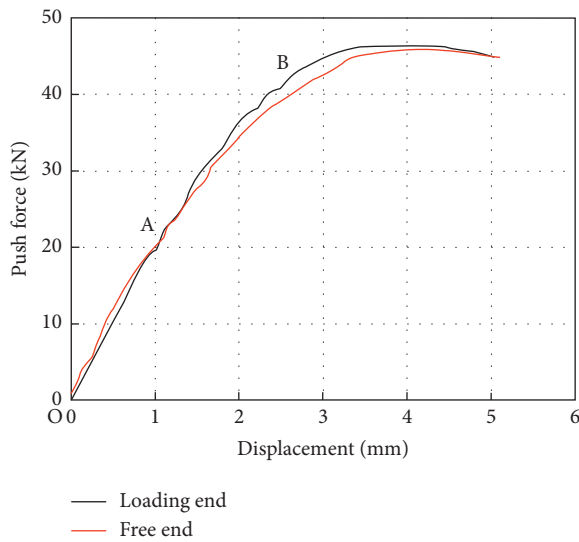

FIGURE 8: Bond-slip curves of the loading end and the free end.

TABLE 2: Relationship between bond strength and density.

Density $\rho/(\text{g/cm}^3)$	0.1	0.2	0.4	0.6	0.8	1.2
Bond strength (MPa)	0.31	0.53	0.6	1.12	1.55	1.98

under saturation conditions, the bond strength is reduced accordingly (as shown in Table 4). As can be seen from Table 5, the bond strength, corresponding to the temperature drop, decreased by 43.8%–57.1% in the dry state. The lower the temperature, the more significant the decrease. In addition, as the temperature drops, the bond strength decreases from 65.2% to 83%. This is because the higher the temperature of the specimen, the slower the temperature loss of the polymer during the reaction and the lower the temperature shrinkage stress. On the other hand, at the concrete interface, the higher the temperature of the specimens, the denser the compaction. Therefore, differences between the reaction temperature of the low temperature specimens and the material in the reaction process are large,

and temperature shrinkage stress is generated. After the reaction, the extrusion and cementation forces are offset by the temperature shrinkage stress, the concrete is disengaged from the concrete, and the bond force is reduced.

3.4. Effect of Polymer Density. To produce polymer water stop plugging, the effect of density on bond strength at low temperatures and under fully saturated interfacial conditions needs to be further investigated [35]. The interface temperature of the specimens is 5°C, and it is fully saturated (24 h). The effect of polymer density on bond strength can be analyzed and compared to dry conditions. Figure 10 shows the relationship between bond strength and polymer density. Based on the linear fitting results, the bond strength between the polymer and the concrete interface is positively correlated with the polymer. The higher the density of the polymer, the higher the bond strength between the polymer and the concrete interface.

The absolute difference in the bond strength between the saturated and dry specimens between $0.1\,\text{g/cm}^3$ and $0.4\,\text{g/cm}^3$ is not significant, with a mean reduction of about 3.8%. However, the absolute difference in density between $0.4\,\text{g/cm}^3$ and $1.5\,\text{g/cm}^3$ is 1.0 and it is significantly larger for $1.2\,\text{g/cm}^3$. The reduction rate is large, ranging from 67.2% to 72.7%. The difference between dense specimens ($1.2\,\text{g/cm}^3$) is much more remarkable. The bond strength between fully saturated low-density specimens and high-density specimens is relatively concentrated, indicating that an increase in polymer density in the water has a limited effect on the growth of bond strength. There are two reasons for this phenomenon. As shown in Figure 7, when the polymer density is relatively low (Figure 7(a)), there are many bubble cells in the polymer, the radius of the bubbles becomes large, and the bubbles are squeezed together. On the other hand, the polymer is combined with the concrete through the thin walls of the bubble chamber, reducing the bond strength. The higher the polymer density (Figure 7(b)), the smaller the radius of the bubble and the thicker the walls. This increases the distance between the bubble chamber and the concrete. Therefore, at the polymer-concrete interface, the thick walls of the bubbles cells bond with the concrete, increasing the

TABLE 3: Relationship between moisture content and bond strength.

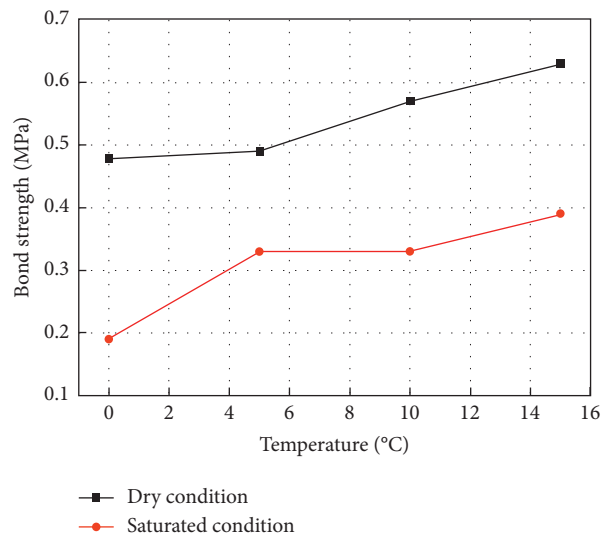| Number	Temperature (°C)	Moisture content (%)	Ave. moisture content (%)	Soaking time (h)	Bond strength (MPa)	Ave. bond strength (MPa)
	0	0	0	0	0.42	0.48
1–3		0			0.56	
		0			0.46	
	0	0.8	0.98	3	0.37	0.3
		1.03			0.44	
13–15		1.11			0.09	
	0	0.95	0.83	10	0.29	0.71
		0.47			0.64	
25–27		1.08			1.12	
	0	0.93	1.3	24	0.25	0.19
37–39		1.19			0.2	
		1.79			0.11	

FIGURE 9: Relationship between temperature and bond strength.

TABLE 4: Saturation conditions.

Number	Density ρ/(g/cm^3)	Soaking time (h)	Temperature (°C)	Ave. moisture content (%)	Bond strength (MPa)	Reduction rate (%)
37–39	0.6	24	0	1.3	0.19	83.0
40–42	0.6	24	5	1.22	0.33	70.5
43–45	0.6	24	10	1.03	0.33	70.5
46–48	0.6	24	15	0.76	0.39	65.2

TABLE 5: Dry condition.

Number	Density ρ/(g/cm^3)	Soaking time (h)	Temperature (°C)	Ave. moisture content (%)	Bond strength (MPa)	Reduction rate (%)
1–3	0.6	0	0	—	0.48	57.1
4–6	0.6	0	5	—	0.49	56.3
7–9	0.6	0	10	—	0.57	49.1
10–12	0.6	0	15	—	0.63	43.8

bond strength. In addition, the expansion force of the polymer increases with density. As a result, the intercalation and cementation of the polymer at the interface become stronger, resulting in higher bond strength [28]. The higher the density of the polymer, the higher the bond strength at the interface in a certain range. This means that the contact

Equation	$y = a + b*x$
Intercept	0.07229 ± 0.02907
Slope	0.7916 ± 0.04559
Pearson's r	0.97602
R-square (COD)	0.95261

▼ Experimental data (saturated condition)
— Linear fitting (saturated condition)

(a)

Equation	$y = a + b*x$
Intercept	0.121 ± 0.03656
Slope	1.67993 ± 0.05736
Pearson's r	0.99137
R-square (COD)	0.98282

● Experimental data (dry condition)
— Linear fitting (dry condition)

(b)

$y = 1.67x + 0.12$
$R^2 = 0.98$

$y = 0.79x + 0.07$
$R^2 = 0.95$

▼ Experimental data (saturated condition)
● Experimental data (dry condition)
— Linear fitting (saturated condition)
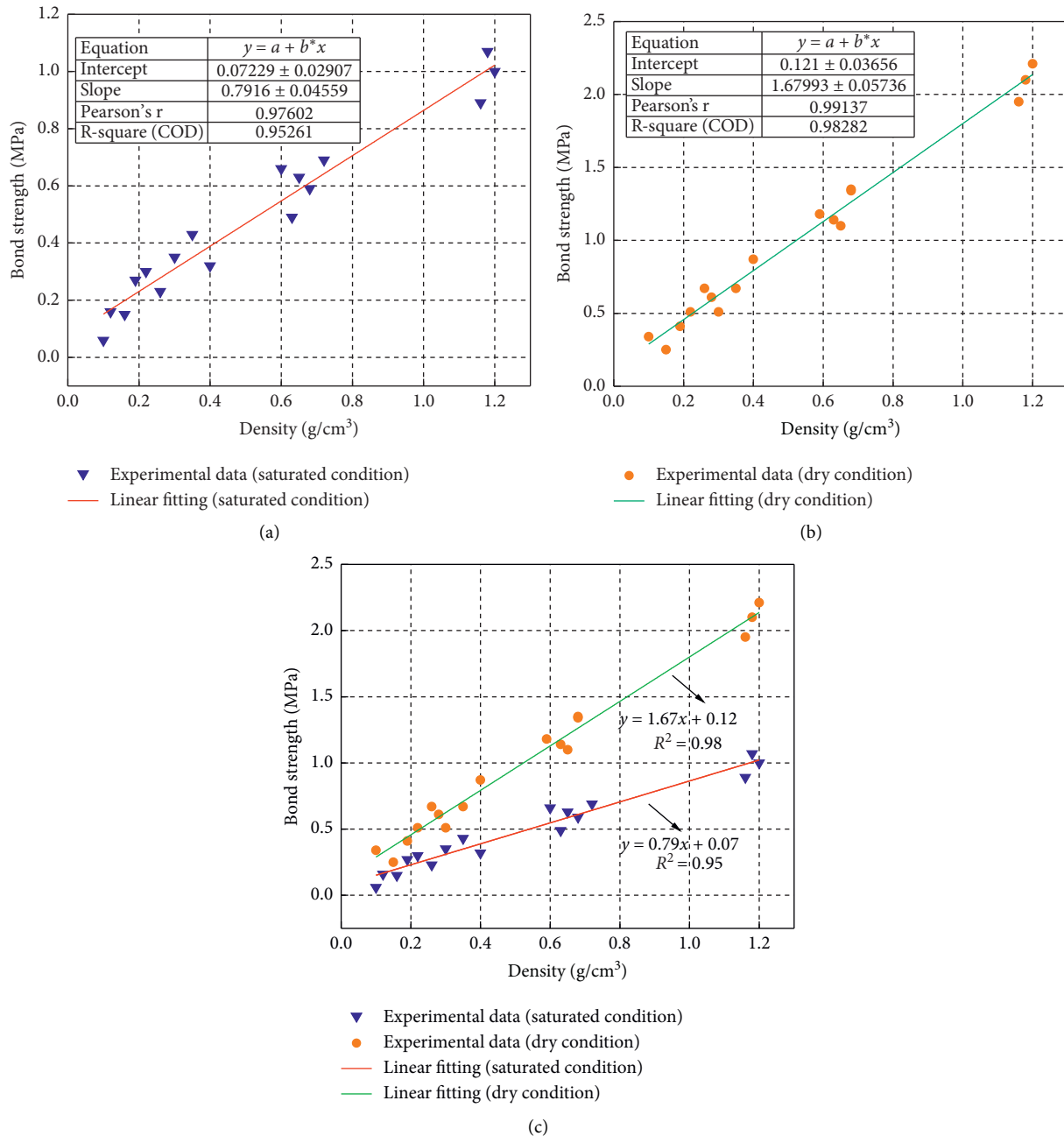— Linear fitting (dry condition)

(c)

FIGURE 10: Relationship between polymer density and bond strength.

surface can withstand higher shear forces and pressures. However, the increase in polymer density has a limited effect on the growth of bond strength at the saturated interface. During the reaction, many bubbles are generated on the surface of the concrete, and the bond strength is significantly reduced due to intrusion. If the specimen polymer density exceeds a specific range, most of it will damage the concrete [36].

4. Conclusion

Through a concentric pushing test system for 120 adhesive specimens, the effects of temperature, density, and interfacial moisture on the bonding properties between polymers and concrete under special construction conditions were studied. From the results obtained, the following conclusions can be drawn:

(1) When fully saturated, increasing the polymer density has little effect on bond strength. In contrast, increased polymer density has a significant effect on bond strength under dry conditions.

(2) Interfacial moisture content is a significant factor affecting the bonding properties between the polymer and concrete. At the same interfacial temperature, the higher the interfacial moisture content, the

lower the bond strength between the polymer and concrete. When the interface is completely saturated, the interfacial bond strength follows this rule, but the overall bond strength is lower than that of a dry interface. For dam concrete structures, reducing interfacial water content and increasing the mass of the polymer are effective methods to improve the bonding force between the polymer and concrete.

(3) The bond strength between the polymer interface and the concrete interface is much less than the shear resistance of the polymer itself. As a result, most of the polymer cores are intact and are mainly damaged by ejecting, with less damage to the inner surface of the concrete.

Data Availability

The data used to support the findings of this study are available from the corresponding author upon request.

Conflicts of Interest

The authors declare that they have no conflicts of interest.

Authors' Contributions

Mingsheng Shi conceptualized the study. Han Tian performed data curation. Xijun Zhang performed formal analysis. Mingsheng Shi was responsible for funding acquisition. Xijun Zhang developed the methodology. Xijun Zhang wrote the original draft. Chaojie Wang reviewed and edited the article.

Acknowledgments

References

[1] J. Conceio, F. Rui, M. Azenha, and M. Miranda, "A new method based on equivalent surfaces for simulation of the post-cooling in concrete arch dams during construction," *Engineering Structures*, vol. 209, Article ID 109976, 2020.

[2] C. J. Billington, "The underwater repair of concrete offshore structures," *Protein and Peptide Letters*, vol. 5, pp. 459–468, 1979.

[3] S. Kazemian and B. K. Bujang, "Assessment and comparison of grouting and injection methods in geotechnical engineering," *European Journal of Scientific Research*, vol. 52, pp. 243–247, 2009.

[4] B. Czupryński, J. Liszkowska, and J. Paciorek-Sadowska, "Modification of the rigid polyurethane-polyisocyanurate foams," *Journal of Chemistry*, vol. 2014, Article ID 130823, 12 pages, 2014.

[5] P. Hong pu, S. U. Yi-sheng, X. Guo-hong, C. Zong-ping, and N. I. Huan-cheng, "Study of bond force on polyurethane foam materal and fly ash concrete," *Journal of Guangxi University*, vol. 34, pp. 9–12, 2009.

[6] L. Hou-Tang, *Preparation and Application of the New Polyurethane Adhensives*, China Adhesives, Shanghai, China, 2005.

[7] Y. Wang and C. Zeng, "Shear behavior of wheat-concrete interface during monotonic and cyclic loading," *Complexity*, vol. 2019, Article ID 6792650, 15 pages, 2019.

[8] X. Yang, K. Zheng, L. Xu, and N. Liu, "Properties and applications of a new chemical grouting material," *Advances in Civil Engineering*, vol. 2020, Article ID 7191354, 10 pages, 2020.

[9] C. Yang-jie, X.-f. Zhang, X.-l. Lu, Q. Lu, and J. Lin-qi, Study on toughness modification of epoxy resin by polyurethane for crack repair in concrete," *Journal of Highway and Transportation Research and Development*, vol. 36, pp. 24–30, 2019.

[10] M. A. Safan, Z. A. Etman, and A. Konswa, "Evaluation of polyurethane resin injection for concrete leak repair," *Case Studies in Construction Materials*, vol. 11, Article ID e00307, 2019.

[11] J. W. Li and B. Z. Y. Qu, "Crack resistance test and application research of high toughness epoxy protective coatings under low temperature," *Water Power*, vol. 40, pp. 90–92, 2014.

[12] Y. Shen, Y. Wang, Y. Yang, Q. Sun, T. Luo, and H. Zhang, "Influence of surface roughness and hydrophilicity on bonding strength of concrete-rock interface," *Construction and Building Materials*, vol. 213, pp. 156–166, 2019.

[13] A. Naudts, "Irreversible changes in the grouting industry caused by polyurethane grouting: an overview of 30 Years of polyurethane grouting," in *Proceedings of the 3nd International Specialty Conference on Grouting and Ground Treatment*, pp. 1266–1280, New Orleans, LA, USA, February 2003.

[14] G. Lazzara, Y. Lvov, G. Cavallaro, R. Fakhrullin, and S. Konnova, "Composite films of natural clay nanotubes with cellulose and chitosan," *Green Materials*, vol. 2, no. 42, pp. 32–42, 2014.

[15] L. Xiaofang, *Development of High-Efficiency Chemical Grouting Material for Dam*, Hu Nan University, Changsha, China, 2001.

[16] C. Hai, T. Liu, and S. Xia, "Processing and analysis of chemical grouting for crack of concrete dam," *Water Power*, vol. 5, 2010.

[17] C. A. Apostolopoulos, K. F. Koulouris, and A. C. Apostolopoulos, "Correlation of surface cracks of concrete due to corrosion and bond strength (between steel bar and concrete)," *Advances in Civil Engineering*, vol. 2019, Article ID 3438743, 12 pages, 2019.

[18] I. Ghaaowd, J. S. McCartney, S. S. Thielmann, M. J. Sanders, and P. J. Fox, "Shearing behavior of tire-derived aggregate with large particle size. I: internal and concrete interface direct shear," *Journal of Geotechnical and Geoenvironmental Engineering*, vol. 143, no. 10, Article ID 04017078, 2017.

[19] L. I. Jing-wei, H. Ju-tao, and H. Ben-zheng, "Study on elastic polyurethane sealing material," *Water Resourcs and Hydropower Engineering*, vol. 11, 2005.

[20] Z. Sun and Y. Lu, "Underwater crack repairing technology for concrete dam," *Water Power*, vol. 11, pp. 65–67, 2002.

[21] Z. Jun, *The Test and Research of the Polyurethane Sealing Material Bonding Performance in Channel Expansion Joint under the Special Construction Environment*, Xinjiang Agricultural University, Ürümqi, China, 2016.

[22] Z. Fang, H.-q. Zhang, K.-y. Zhang, S.-h. He, and B. Tu, "Experimental research on bond performance of bond face between high-performance grouting materials and rock

anchor," *Journal of the China Railway Society*, vol. 36, pp. 104–110, 2014.

[23] L. Eduarda and B. Lourenço Paulo, "Bond strength characterization of commercially available grouts for masonry," *Construction and Building Materials*, vol. 144, pp. 317–326, 2017.

[24] W. Luo, Y.-y. Xiao, H. E. Donger, and Z. Zhang, "Experimental study on interfacial tensile bonding performance of pre-heated CFRP-concrete under fast load," *Engineering Mechanics*, vol. 35, pp. 307–312, 2018.

[25] C. Yuan, W. Chen, T. M. Pham et al., "Effect of aggregate size on the dynamic interfacial bond behaviour between basalt fiber reinforced polymer sheets and concrete," *Construction and Building Materials*, vol. 227, Article ID 116584, 2019.

[26] Z. Zhenyu, W. Shanyong, and J. Feng, "Frictional behaviour of the interface between concrete and rubber: laboratory shear test and its elastoplastic model," *Engineering Fracture Mechanics*, vol. 197, pp. 192–205, 2018.

[27] L. Heng, F. Wang, and M. Shi, "Experimental and numerical simulation on bond behavior between polymer anchorage body and soil," *Journal of Hydraulic Engineering*, vol. 49, pp. 749–756, 2018.

[28] H. Liu, M. Shi, and F. Wang, "Experimental research on the bond strength between polyurethane polymer and steel bars," *Chinese Journal of Underground Space and Engineering*, vol. 12, pp. 1119–1225, 2016.

[29] Standard for test method of mechanical properties of ordinary concrete, *Standard for Test Method of Mechanical Properties of Ordinary Concrete*, China Planing Press, Beijing, China, 2002.

[30] S. Mingsheng, *Research on Polymer Grouting Material Properties and Directional Fracturing Grouting Mechanism for Dykes and Dams*, Dalian University of Technology, Dalian, China, 2011.

[31] S. Mingsheng, F. Wang, and J. Luo, "Compressive strength of polymer grouting material at different temperatures," *Journal of Wuhan University of Technology: Materials Science English Edition*, vol. 25, pp. 962–965, 2010.

[32] M. Wang Fu, M. S. Shi, H. J. Li, and Y. H. Zhong, "Experimental study on the anti-permeability properties of polymer grouting materials," *Advanced Materials Research*, vol. 284, pp. 284–286, 2011.

[33] G. Pompe, M. Brauer, J. Schweikle, B. Nagel Hupfer, and D. Lehmann, "Influence of the temperature profile in the interface on the bond strength of polyamide–polyurethane two-component tensile bars," *Journal of Applied Polymer Science*, vol. 100, pp. 4297–4305, 2010.

[34] R. S. Ghosh and V. M. Malhotra, "Use of superplasticizers as water reducers," *Cement, Concrete and Aggregates*, vol. 1, pp. 56–63, 1979.

[35] H. Fang, Z. Su, X. Li, F. Wang, and Y. Fu, "Interfacial bond performance between self-expansion polymer and concrete," *Construction and Building Materials*, vol. 270, Article ID 121459, 2020.

[36] R. Haddad and M. Haddad, "Predicting fiber-reinforced polymer-concrete bond strength using artificial neural networks: a comparative analysis study," *Structural Concrete*, vol. 22, no. 1, pp. 38–49, 2020.

Research Article

Investigation of Dynamic, Mechanical, and Thermal Properties of *Calotropis procera* Particle-Reinforced PLA Biocomposites

K. Yoganandam,[1] Vigneshwaran Shanmugam,[2] A. Vasudevan,[2] D. Vinodh,[2]
N. Nagaprasad,[3] Balasubramaniam Stalin ⃝,[4] Alagar Karthick ⃝,[5]
Chandrabhanu Malla ⃝,[6] and Murugesan Bharani ⃝[7]

[1]*Department of Mechanical Engineering, ARM College of Engineering and Technology, Kancheepuram-603209, Tamil Nadu, India*
[2]*Department of Mechanical Engineering, Saveetha School of Engineering, Saveetha Institute of Medical AndTechnical Sciences, Chennai 602, Tamilnadu, India*
[3]*Department of Mechanical Engineering, ULTRA College of Engineering and Technology, Madurai-635107, Tamil Nadu, India*
[4]*Department of Mechanical Engineering, Anna University, Regional Campus Madurai, Madurai-, 501, Tamilnadu, India*
[5]*Department of Electrical and Electronics Engineering, KPR Institute of Engineering and Technology, Arasur, Coimbatore-641407, Tamilnadu, India*
[6]*Department of Mechanical Engineering, Radhakrishna Institute of Technology and Engineering, Bhubaneswar-752057, Odisha, India*
[7]*School of Textile Leather and Fashion Technology Kombolcha 208, Kombolcha Institute of Technology, Wollo University, Dessie, Ethiopia*

Correspondence should be addressed to Murugesan Bharani; bharani.murugesan@kiot.edu.et

The thermal behavior of the biodegradable *Calotropis procera* (CP) particle-reinforced polylactic acid (PLA) biocomposites was investigated. The injection molding process was used to make the composites, and the CP particle weight percentage was varied during the process (0%, 5%, 10%, 15%, and 20%). The melt flow index, heat deflection temperature, Vicat softening point, and the thermal properties of the composites were determined using dynamic mechanical testing. The results were analyzed and compared to the thermal properties of the neat PLA. The results revealed the increase in thermal stability of the PLA due to the addition of CP particles. The CP particles aided in the restriction of polymer mobility, which elevated the glass transition temperature of the composite. Incorporating CP particles in the PLA can increase the PLA/CP composite utilization in heat dissipation applications.

1. Introduction

Ecofriendly natural-based composites are the spotlight in today's sustainable world. Global efforts are initiated to avoid the usage of fossil-based polymers and composites, which can endanger the environment. The global waste of polymeric materials has caused severe environmental issues which have severely impacted the global environment [1]. Natural-based reinforcement and bio-based polymer matrix are revealed as sustainable solutions for developing high-strength bio-based polymer composites, replacing traditional polymers and their composites [2, 3]. For example, the use of natural fiber in polymer matrices has increased the biodegradability of the polymers and made them more sustainable without reducing their strength [4]. The natural fibers derived from polysaccharides (cellulose and hemicellulose) can be used as fiber and filler. The research mentioned in this paper outlines the development of natural filler-based biocomposites. *Calotropis procera* (CP) is a shrub whose stem can be used to extract natural cellulosic

fibers. These fibers have cellulose material which possesses desirable elongation and strength characteristics. Compared to cotton and jute fibers, the CP variants have elevated weight per square centimeter and enhanced tensile and abrasive capacities [5]. The CP is a commonly grown plant in India and can be used as a low-cost source of cellulose fibers to supplement the existing fibers. In the current study, the CP fiber was converted into particles and used to develop composites.

Plastics cannot be substituted easily by other materials due to their unique properties, such as good mechanical performance, low density, transparency, low cost, heat sealability, chemical resistance, and barrier capability [6, 7]. Researchers are striving hard to develop an environment-friendly material to replace plastic. Polylactic acid (PLA) is one of the most productive and promising environment-friendly polymers due to its appealing mechanical properties, renewability, biodegradability, and low cost [8]. Although the PLA has many advantages, its brittle nature, impact strength, and thermal properties are not conducive for its usage in several industrial applications [9]. The inclusion of filler material to the PLA polymeric material improves its thermal and mechanical properties, facilitating its usage in various applications [10, 11]. Bio-fillers have invoked the researcher's interest due to their low cost and environmental-friendly nature. It facilitates the easy manufacturing of polymer composites, making them suitable for automotive, structural, and other applications [12, 13]. Several studies have found that the addition of bio-fillers to polymer composites was found to augment thermal stability. For instance, PLA-based biocomposites developed using rice husk, wheat husk, and wood fiber exhibited thermal properties. The composites prepared using rice husk revealed a least thermal conductivity of 0.08 W/m.K [14]. In another study, Chun et al. reported that the addition of coconut shell particles to the PLA elevated the glass transition temperature of the composite, thereby increasing its thermal stability [15].

The dynamic mechanical analysis (DMA) is used to determine the storage modulus, loss modulus, Tan δ, and the glass transition temperature of natural fiber-reinforced polymer composites as a function of temperature [16]. By determining these parameters under dynamic loading conditions concerning temperature, the viscoelastic nature of the fabricated composites can be derived [17]. The DMA details the transition zone of composites, where the polymer molecule movement is initiated [18–21]. The melt flow index (MFI) affects the mixing efficiency of the filler and plastic materials. Plastics with higher MFI were found to improve flow and distribution [22]. The MFI determines the average molecular weight and reverses the melt viscosity. Hence, the elevation of MFI is proportional to its melt flow. The MFI is desirable for predicting and regulating the composite fabrication process [23]. The Vicat softening temperature parameter is essential when the fabricated composite finds utility in potential applications like construction industries. The Vicat softening temperature will establish the material's ability to withstand penetration under increased temperatures [24]. The Vicat softening point (VSP) is a measurement

that is used to compare the heat softening properties of the composite materials [25]. The systematic literature survey revealed various investigations initiated by researchers for identifying a suitable biodegradable polymeric composite for various applications. In this study, the *Calotropis procera* fiber-reinforced polylactic acid composite was fabricated using the injection molding technique and investigated for analyzing its thermal performance. The dynamic mechanical analysis, melt flow index, Vicat softening point, and the heat deflection temperature were determined using suitable procedures to determine the thermal performance of the fabricated natural fiber-filled PLA composites.

2. Materials and Methods

2.1. Materials. The PLA used in the present investigation was purchased from Nature-Tech India Pvt. Ltd, Chennai, India, having a specific gravity of 1.24, the relative viscosity of 3.3, glass transition temperature in the range of 55–60°C, and an MFI of 14 g/10 min (210C, 2.16 kg). The CP particles were prepared manually from the CP fibers extracted from the twig of a two-to-three-year-old CP plant. Initially, the CP fibers were manually extracted from the twig of the CP plant (Figure 1(a)) with the help of the retting process. The extracted fibers were cleaned in water to remove contaminants and unnecessary impurities. The fibers were then sun-dried for 4 hours before being oven-dried for 24 hours at 60°C to ensure an absence of moisture in the fiber. The well-dried fibers were cut to 0.3–0.5 mm length and placed in the desiccator. The cut-fibers were converted into particles using the ball milling process, which was done for 8 hours at 800 rpm with a ball ratio of 10 : 1. The powdered particles were collected and kept in an oven which was maintained at 60°C for 24 hours and used for composite fabrication. Figure 1 shows the CP plant, pellets, and the composite samples used in the DMA test.

2.2. Fabrication of Composites. The biocomposite fabrication was done in two steps. In the first step, the preparation of PLA/CP pellets (Figures 1(b) and 1(c)) was done with the help of a twin-screw extruder. The second step involved developing biocomposite samples (Figure 1(d)) as per ASTM Standards (plates) using the injection molding process. The PLA/CP pellets were developed using the twin-screw extruder (Coperion-ZSK26), operated at a screw rpm of 100. The extrusion temperature was maintained in a range between 160 and 180°C. The temperatures above the mentioned range were found to degrade the CP particles. The extruded blend was then pelletized. The PLA/CP pellets were then oven-dried at 60°C to avoid moisture content. Using the injection molding machine (JSW-J75E), the composites specimens were fabricated at 7 bar back pressure, 60 mm/sec screw speed, 175°C temperature, and 30°C molding temperature.

2.3. Dynamic Mechanical Analysis. The three-point flexural method of DMA testing was done to measure the composites' storage modulus and loss modulus. A DMS 6100
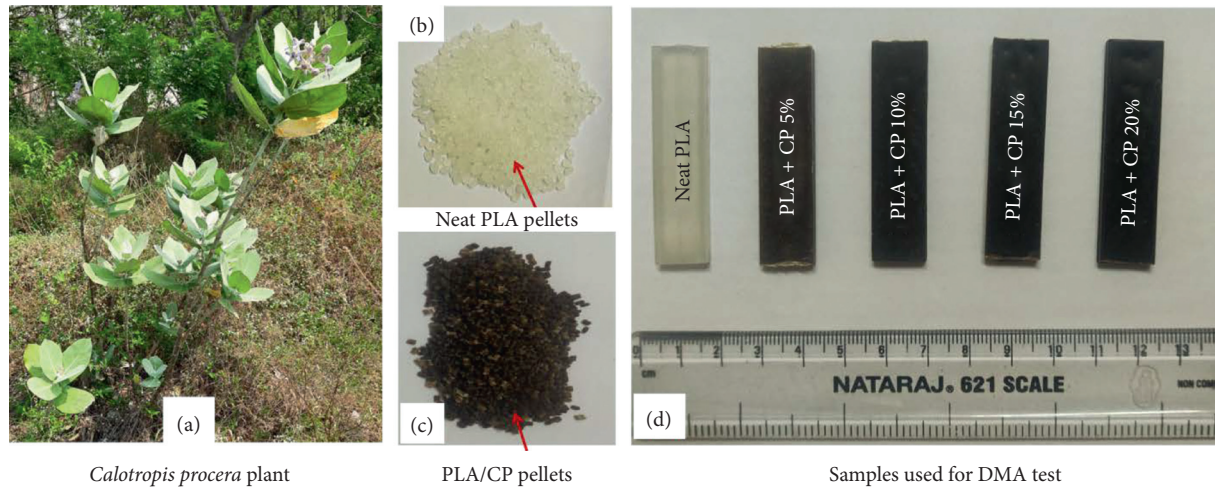
Figure 1: (a) *Calotropis procera* plant. (b) Neat PLA pellets. (c) PLA/CP pellets. (d) Samples used for DMA test.

instrument (SII Nano Technology, Japan) was used for conducting the dynamic mechanical test. The neat PLA and PLA/CP composite specimens (size-$52 \times 13 \times 3$ mm) were subjected to a temperature range between 30°C and 130°C and a frequency of 20 Hz. During the experiments, the samples were heated at a rate of 3°C/min.

2.4. Melt Flow Index.

The MFI of the PLA/CP composites was measured using the Ametek Davenport MFI 10 equipment at a temperature of 210°C and a load of 2.16 kg following the ASTM D1238-04 protocol.

2.5. Heat Deflection Temperature.

The heat deflection temperature (HDT) was measured in a three-point bending manner using the Presto HDT/VSP Tester (model: HDT/VSP-500) following ASTM D648. A specimen having the dimensions of 125 mm $\times 12.5$ mm $\times 3$ mm was used. The HDT was obtained for each sample at a deflection of 0.25 mm and a heating rate of 2°C/minute under a load of 0.5 MPa.

2.6. Vicat Softening Point.

The Vicat softening point test for the fabricated CP-filled PLA composites was done following the ASTM D1525-17*e*1 standard. The specimens with dimensions of $10 \times 10 \times 3$ mm were used for testing. The specimen was placed in the testing apparatus (Presto HDT/VSP Tester: HDT/VSP-500) with the penetrating needle at approximately 1 mm from the surface's edge. After this, the specimen was immersed in an oil bath heated to 230°C, followed by applying a force of 10 N. The bath temperature was gradually increased by 50°C every hour until the needle penetrated 1 mm.

3. Results and Discussion

3.1. DMA Results.

The results of the DMA test are revealed in Figure 2. The effect of the CP particle reinforcement on the storage modulus of PLA composites is depicted in Figure 2(a). Three distinct regions, namely, the glassy,

transition, and rubbery regions, were identified from the storage modulus curve at temperatures ranging from 30 to 125 C. The glassy region occurred between ca.30 and 60°C, the transition temperature occurred between ca.60 and 75°C, and the rubbery region occurred between ca.75 and 125°C. The storage modulus of the PLA/CP composites was found to increase after ca.85°C, except for the neat PLA, which was due to the cold crystallization of the PLA/CP composites. In general, cold crystallization occurs when the polymer chain gains sufficient mobility to arrange itself into an ordered structure (i.e., crystalline structure) due to chain folding. The storage modulus of composites and neat PLA decreased between 60 and 75°C. In general, the transition temperature for PLA is 60°C. The drop in storage modulus after the glassy region was caused by a change in the material's elastic behavior to viscoelastic behavior, visible in the transition region. Compared to neat PLA, the storage modulus of the PLA composites increased in both the glassy and rubbery regions. The 20 wt.% CP-added composite had the highest storage modulus, followed by the 15 wt.%, 10 wt.%, and 5 wt.% CP-added composites. At 5°C, the storage modulus of the 20 wt.% CP composites were 35% higher than the neat PLA. This was due to an increase in the composite stiffness in all three regions, which was a function of the reinforced CP particles. The increased stiffness of the composites resulted from the better compatibility of the CP particles with the matrix, which can be understood from Figure 3.

Figure 2(b) depicts the loss modulus of the PLA/CP composites with varying wt.% of CP particles. In general, the loss modulus increased until it attained the glass transition temperature, followed by a precipitous fall. The CP/PLA composites followed a similar pattern. The sudden drop in the loss modulus after the glass transition temperature was due to increased polymer mobility, which increased the viscosity of the composite. For the composite with 20 wt.% CP, the loss modulus increased steadily until the peak value (66°C), followed by a sharp decrease up to 82°C. A small peak at 90°C was observed, which was due to cold crystallization. In both the glassy and transition regions, the magnitude of the loss modulus was more significant for the composites
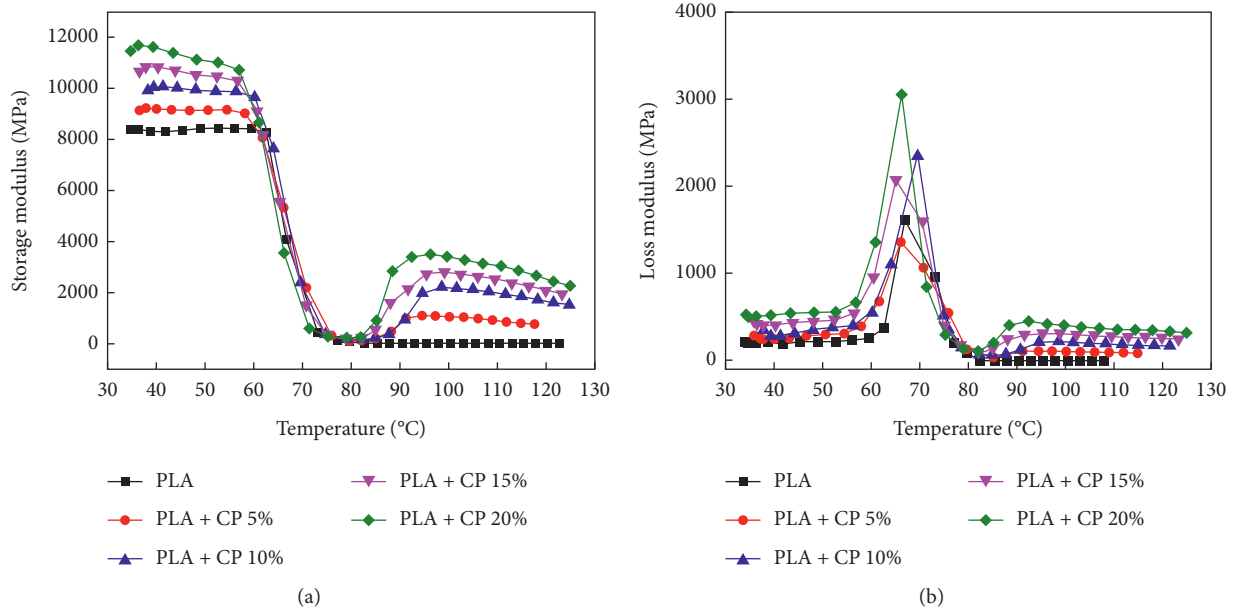
(a)

(b)

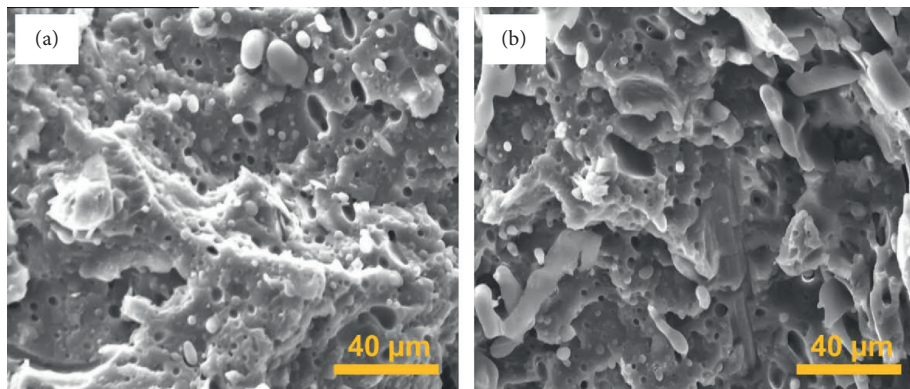Figure 2: Storage modulus and loss modulus of PLA/CP.

Figure 3: SEM image showing interaction of CP with PLA: (a) 15% CP composite and (b) 20% CP composite.

than the neat PLA. The peaks of the composites were found to be broad with distinct amplitude and temperature positions, owing to the development of complex relaxation behavior as a result of the polymeric matrix's restricted chain mobility. The displacement of the peak of the composite was observed at lower temperatures compared to neat PLA, owing to the increased flexibility of the composites that resulted from the addition of CP particles.

Generally, the glass transition temperature can be determined from the loss modulus concerning temperature. However, the loss modulus was more sensitive to the molecular movements under the same deformation amplitude in this case. The glass transition temperature of the PLA/CP composites was higher than that of the neat PLA due to the restriction in polymer chain mobility caused by the addition of the CP particles.

3.2. Melt Flow Index of CP/PLA Composites. Figure 4 reveals the melt flow test results of the PLA/CP composites. The

melt flow index of the neat PLA was 13 g/10 min. The melt flow of the PLA was reduced after the addition of the CP particles in a usual manner. The reinforcement of 5 wt.% and 10 wt.% CP particle reinforcement revealed lower MFI when compared to the neat PLA. However, the composites, reinforced with 15 wt.% and 20 wt.% CP particles, possessed higher MFI than the neat PLA and the other two PLA/CP composites. The lower MFI value at 5 wt.% and 10 wt.% particle content was due to the strong interaction of the PLA and CP particles, which restricted the movement of the polymer chains, resulting in a reduction in the flowability of the PLA/CP composite.

The addition of CP particles increased the viscosity of the molten PLA while decreasing its elasticity. However, this mechanism depended on the particle loading content of the PLA composite with 20 wt.% CP having the highest MFI, which was three times higher than the neat PLA. The PLA composite with 5 wt.% had the lowest MFI. The MFI of the 20 wt.% CP composite increased by 332% when compared to the 5 wt.% CP-added composite. This increase was
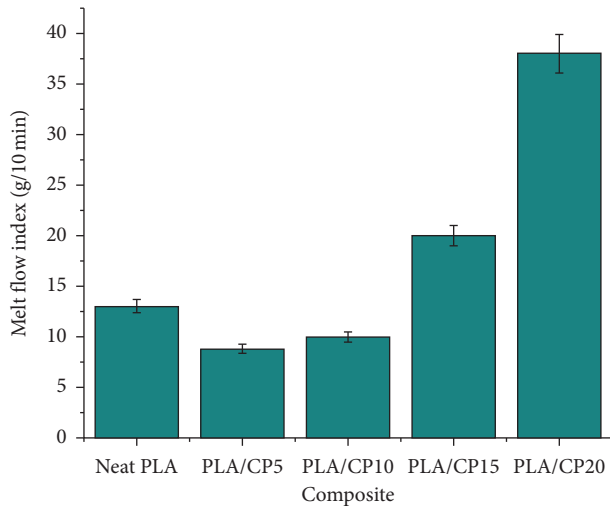
FIGURE 4: Melt flow index of PLA/CP.

FIGURE 5: Heat deflection temperature of PLA/CP.

FIGURE 6: Vicat softening point of PLA/CP.

primarily attributed to increased particle-to-particle inter- action in the composites after the 15% and 20% CP particles, respectively. At high testing temperatures, the bioparticles lose their stability and interaction as thermal degradation begins, resulting in a weak polymer-polymer link that allows the polymer to move freely. This reduces the polymer's viscosity, which increases the MFI.

3.3. Heat Deflection Temperature of CP/PLA Composites. The heat deflection temperature of the CP/PLA composites is shown in Figure 5. After incorporating the CP filler material into the PLA, the heat deflection temperature gradually increased. The addition of CP filler material to the PLA matrix resulted in a 4% to 20% increase in heat de- flection temperature. The heat deflection temperature gradually increased from 50°C to 58°C as the filler particle content increases from 5 wt.% to 20 wt.%. Maximum en- hancement was noted for the composite with 20 wt.% CP, 20% higher than the neat PLA. A minimal enhancement (4%) was noted for the composite with 5 wt.% CP added. Furthermore, lower polymer content at a higher CP content increased the polymer-to-particle interaction rather than the polymer-to-polymer interaction. The increased particle- polymer interaction probably accounted for the improved HDT at 20% CP composites.

3.4. Vicat Softening Point of CP/PLA Composites. The VSP of the CP/PLA composites is depicted in Figure 6. The VSP of the neat PLA was around 55°C. When the filler was added to the composites ranging from 5% to 20%, the VSP of the composites increased from 57°C to 64°C. This demonstrated the effectiveness of the CP filler particles in PLA composites against the VSP. The needle penetrated to a depth of 1 mm inside the neat PLA at a lower temperature (55°C) than the PLC/CP composites. This was because the addition of CP to the PLA increased its rigidity, which increased the hardness of the composites.
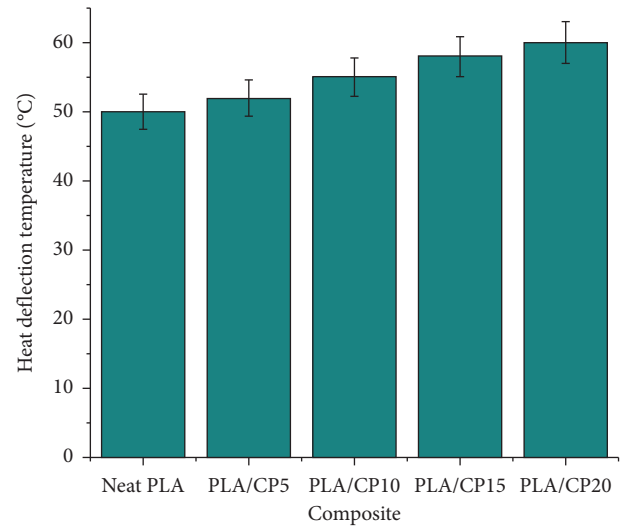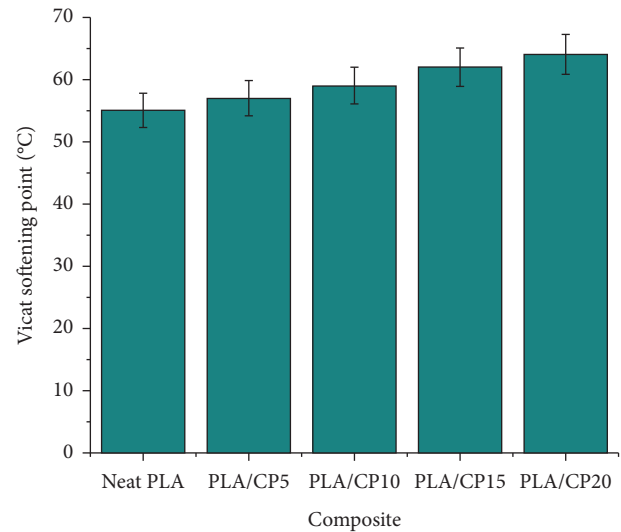
Furthermore, increasing the temperature was not suf- ficient to break the bonding between the PLA and CP particles because of the increased stiffness of the composites. The increased stiffness was also the reason for the com- posite's increased VSP. The composite's storage modulus results can explain the increased stiffness.

4. Conclusion

The PLA-based biocomposites reinforced with natural filler CP were successfully manufactured using the injection molding process. The thermal properties of the composites were studied, including the dynamic mechanical analysis, heat deflection temperature, melt flow index, and the Vicat softening point. The addition of CP particles to PLA in- creased the thermal stability of the composites. The 20 wt.% CP-added composite possessed the highest storage modulus, followed by the 15 wt.%, 10 wt.%, and 5 wt.% CP-added

composites. The glass transition temperature of the PLA/CP composites was higher than the neat PLA due to the restriction in the polymer chain mobility caused by the addition of the CP particles. The reinforcement of 5 wt.% and 10 wt.% CP particle reinforcement had lower MFI when compared to the neat PLA. However, the composites with 15 wt.% and 20 wt.% CP-added composites had higher MFI than the neat PLA and the other two PLA/CP composites. The heat deflection temperature of the 20 wt.% CP composites were 20% higher when compared to neat PLA. The maximum VSP for the 20 wt.% CP composites were 64°C, which was 16% higher than the neat PLA. The increased thermal stability was due to restriction in polymer chain movement due to the addition of CP particles. The findings resultant of our investigation can be used to induce enhanced thermal resistance in the PLA-based biocomposites.

Data Availability

The data used to support the findings of this study are included in the article.

Conflicts of Interest

The authors declare that there are no conflicts of interest regarding the publication of this article.

References

[1] S. Thakur, J. Chaudhary, B. Sharma et al., "Sustainability of bioplastics: opportunities and challenges," *Current Opinion in Green and Sustainable Chemistry*, vol. 13, pp. 68–75, 2018.

[2] V. Arumugaprabu, R. Johnson, and S. Vigneshwaran, "Mechanical performance of nanocomposites and biomass-based composite materials and its applications: an overview," in *Handbook of Nanomaterials and Nanocomposites for Energy and Environmental Applications*Springer International Publishing, Geneva, Switzerland, 2020.

[3] S. Vigneshwaran, R. Sundarakannan, K. M. John et al., "Recent advancement in the natural fiber polymer composites: a comprehensive review," *Journal of Cleaner Production*, vol. 277, Article ID 124109, 2020.

[4] T. Gurunathan, S. Mohanty, and S. K. Nayak, "A review of the recent developments in biocomposites based on natural fibres and their application perspectives," *Composites Part A: Applied Science and Manufacturing*, vol. 77, pp. 1–25, 2015.

[5] M. J. Raghu and G. Govardhan, "Development of Calotropis procera-glass fibers reinforced epoxy hybrid composites: dynamic mechanical properties," *Journal of Natural Fibers*, pp. 1–8, 2020.

[6] P. A. Fowler, J. M. Hughes, and R. M. Elias, "Biocomposites: technology, environmental credentials, and market forces," *Journal of the Science of Food and Agriculture*, vol. 86, no. 12, pp. 1781–1789, 2006.

[7] M. P. Ho, H. Wang, J. H. Lee et al., "Critical factors on manufacturing processes of natural fibre composites," *Composites Part B: Engineering*, vol. 43, pp. 3549–3562, 2012.

[8] F. M. Lamberti, A. Luis, R. Ramírez, and J. Wood, "Recycling of bioplastics: routes and benefits," *Journal of Polymers and the Environment*, vol. 28, no. 10, pp. 2551–2571, 2020.

[9] J.-M. Raquez, Y. Habibi, M. Murariu, and P. Dubois, "Polylactide (PLA)-based nanocomposites," *Progress in Polymer Science*, vol. 38, no. 10-11, pp. 1504–1542, 2013.

[10] X. Zhao, X. Wang, Z. Wu, and Z. Zhu, "Fatigue behavior and failure mechanism of basalt FRP composites under long-term cyclic loads," *International Journal of Fatigue*, vol. 88, pp. 58–67, 2016.

[11] E. Fortunati, F. Luzi, W. Yang et al., "Bio-based nanocomposites in food packaging," *Nanomaterials for Food Packaging: Materials, Processing Technologies, and Safety Issues*, pp. 71–110, 2018.

[12] A. M. Nafchi, M. Moradpour, M. Saeidi, and A. K. Alias, "Thermoplastic starches: properties, challenges, and prospects," *Starch–Stärke*, vol. 65, no. 1-2, pp. 61–72, 2013.

[13] J. K. Pandey, S. H. Ahn, S. L. Caroline, A. K. Mohanty, and M. Misra, "Recent advances in the application of natural fiber based composites," *Macromolecular Materials and Engineering*, vol. 295, no. 11, pp. 975–989, 2010.

[14] R. Muthuraj, C. Lacoste, P. Lacroix, and A. Bergeret, "Sustainable thermal insulation biocomposites from rice husk, wheat husk, wood fibers and textile waste fibers: elaboration and performances evaluation," *Industrial Crops and Products*, vol. 135, pp. 238–245, 2019.

[15] K. S. Chun, S. Husseinsyah, and H. Osman, "Mechanical and thermal properties of coconut shell powder filled polylactic acid biocomposites: effects of the filler content and silane coupling agent," *Journal of Polymer Research*, vol. 19, no. 5, pp. 1–8, 2012.

[16] A. Etaati, S. Pather, Z. Fang, and H. Wang, "The study of fibre/matrix bond strength in short hemp polypropylene composites from dynamic mechanical analysis," *Composites Part B: Engineering*, vol. 62, pp. 19–28, 2014.

[17] B. Sethuraman, S. P. Subramani, S. K. Palaniappan, B. Mylsamy, and K. Aruchamy, "Experimental investigation on dynamic mechanical and thermal characteristics of Coccinia Indica fiber reinforced polyester composites," *Journal of Engineered Fibers and Fabrics*, vol. 15, 2020.

[18] A. Manral and P. K. Bajpai, "Static and dynamic mechanical analysis of geometrically different kenaf/PLA green composite laminates," *Polymer Composites*, vol. 41, no. 2, pp. 691–706, 2020.

[19] K. A. Ali, V. Mohanavel, M. Ravichandran, S. A. Vendan, T. Sathish, and A. Karthick, "Microstructure and mechanical properties of friction stir welded SiC/TiB$_2$ reinforced aluminum hybrid composites," *Siliconindia*, pp. 1–11, 2021.

[20] V. Kavimani, B. Stalin, P. M. Gopal, M. Ravichandran, A. Karthick, and M. Bharani, "Application of r-GO-MMT hybrid nanofillers for improving strength and flame retardancy of epoxy/glass fibre composites," *Advances in Polymer Technology*, vol. 2021, Article ID 6627743, 9 pages, 2021.

[21] S. D. Kumar, M. Ravichandran, A. Jeevika, B. Stalin, C. Kailasanathan, and A. Karthick, "Effect of ZrB2 on microstructural, mechanical and corrosion behaviour of aluminium (AA7178) alloy matrix composite prepared by the stir casting route," *Ceramics International*, vol. 47, no. 9, pp. 12951–12962, 2021.

[22] M. Hamed Shojaie, A. H. Hemmasi, M. Talaeipour, and E. Ghasemi, "Effect of gamma-ray and melt flow index of polypropylene on the properties of the lignocellulosic composite," *Radi-ation Physics and Chemistry*, vol. 177, Article ID 109126, 2020.

[23] M. T. Sarabi, A. H. Behravesh, P. Shahi, and Y. Daryabari, "Effect of polymeric matrix melt flow index in reprocessing

extruded wood-plastic composites," *Journal of Thermoplastic Composite Materials*, vol. 27, pp. 881–894, 2014.

[24] Y. Tao, J. Ren, S. Li, H. Yuan, and Y. Li, "Effect of fiber surface-treatments on the properties of poly(lactic acid)/ramie composites," *Composites Part A: Applied Science and Manufacturing*, vol. 41, no. 4, pp. 499–505, 2010.

[25] G. Ali, "The physical and mechanical properties of polymer composites filled with Fe-powder," *Journal of Applied Polymer Science*, vol. 99, no. 5, pp. 2438–2442, 2006.